TYPE IA SUPERNOVAE IN THE ULTRAVIOLET, OPTICAL, AND NEAR-INFRARED

A Dissertation

by

MICHAEL THOMAS SMITKA

Submitted to the Office of Graduate and Professional Studies of
Texas A&M University
in partial fulfillment of the requirements for the degree of

DOCTOR OF PHILOSOPHY

Chair of Committee,	Nicholas B. Suntzeff
Committee Members,	Darren DePoy
	Mark Lemmon
	Lifan Wang
Head of Department,	Peter McIntyre

August 2016

Major Subject: Physics

ABSTRACT

We present an ultraviolet (UV) spectroscopic atlas containing 91 spectra of 22 unique Type Ia supernovae (SNe Ia). The spectra were observed using the Ultraviolet/Optical Telescope (UVOT) onboard the *Swift* space telescope. We present a new technique of decontaminating UVOT grism spectra, which we apply to 40 of the spectra in our sample. We present the first UV spectroscopic series of a peculiar 1999aa-like SN Ia, iPTF14bdn, and compare to normal SNe in our sample. We find this SN to be very blue at early times due to a bright feature between $2800 - 3200$Å. We attribute this to a lower UV opacity caused by higher temperatures above the SN photosphere, likely due to a greater quantity of ^{56}Ni in this region. We also identify the spectroscopic feature differences between $2700 - 3300$Å responsible for the near-UV (NUV) photometric diversity. Comparison of these features to model data suggest that NUV-bluer SNe result from lower metal abundances in the outer ejecta layers.

We combine our UV spectral atlas with UV, optical and NIR photometry, and spectra to generate a UV-O-IR spectral series atlas for 8 SNe Ia near peak brightness. The UV-O-IR SEDs represent time evolution within -10 to $+30$ days of peak brightness, decline rates between $0.9 < \Delta m_{15}(B) < 1.8$, and UV subclassification (when known). Using these data, we calculate integrated bolometric luminosities and synthesized ^{56}Ni masses. We demonstrate that our UV-O-IR SEDs provide an improved method of calculating K-corrections for B-band optical photometry, and present an analysis of SNe Ia UV K-corrections. We present a method of calculating bolometric corrections which take the SNe decline rates into account for SNe near peak brightness.

ACKNOWLEDGEMENTS

Thanks, Nick.

Thanks, Peter.

Thanks, Kevin.

Thanks, Karen.

Thanks, Andrew.

Thanks, Mom and Dad.

Congratulations, Brett, Jimmy, Ryan, Steven, and Ting.

The authors acknowledge the Texas A&M University Brazos HPC cluster that contributed to the research reported here. Brazos Computational Resource, Academy for Advanced Telecommunications and Learning Technologies, Texas A&M University (brazos.tamu.edu).

NOMENCLATURE

CSP	Carnegie Supernova Project
mag	Apparent Magnitude
Mag	Absolute Magnitude
SED	Spectral Energy Distribution
SN	Supernova
SN Ia	Type Ia Supernova
SNe Ia	Type Ia Supernovae (plural)
UVOT	Ultraviolet/Optical Telescope
z	Redshift

TABLE OF CONTENTS

Page

LIST OF FIGURES

FIGURE Page

LIST OF TABLES

TABLE Page

1. INTRODUCTION

Supernovae (SNe) are among the most energetic astrophysical phenomena, produce much of the heavy atomic nuclei in the universe, and are standardizable astrophysical candles. Thus, they are useful as tools for investigating fundamental physics, the atomic evolution of the universe, and making distance measurements with the goal of measuring the expansion history of the universe. The empirical relationship in which luminosities of Type Ia supernovae (SNe Ia) are proportional to broadband filter lightcurve width makes them ideal targets for calculating cosmological distances at redshifts $z \leq 1.5$ (Pskovskii, 1977, 1984; Phillips, 1993; Perlmutter et al., 1997; Burns et al., 2014). This characteristic has been utilized in projects measuring the value of the Hubble constant H_o (Hamuy et al., 1996; Suntzeff et al., 1999; Freedman et al., 2001; Riess et al., 2016), and projects leading to the discovery of the accelerating expansion of the universe attributed to dark energy (Riess et al., 1998; Perlmutter et al., 1999). The physical origin of this characteristic behavior is believed to be the product of variable amounts of ^{56}Ni synthesis in the thermonuclear explosions of white dwarf progenitor stars. This produces an observable spectrum of SNe behaviors in which SNe with less ^{56}Ni synthesis produce intrinsically dimmer peak luminosities and display more rapidly evolving lightcurves than their more ^{56}Ni rich counterparts.

In the two decades since the first major steps into SNe Ia science were taken, many additional photometric studies have been completed. The Union compilation (Kowalski et al., 2008), Constitution compilation (Hicken et al., 2009), Union2 compilation (Amanullah et al., 2010), and its followup Union2.1 compilation (Suzuki et al., 2012) provide a photometric compilation of the collective 833 SNe. They provide analyses

of the systematic differences between 19 data sets, and suggest agreement with a flat ΛCDM cosmological model. Amanullah et al. (2010) cites the three major sources of systematic errors in the measurement of w: 1) zero-points of the photometric systems, 2) the colors of the standard star Vega used in the definition of photometric systems, and 3) the intrinsic color variations of SNe Ia.

In addition to photometric studies, spectrophotometric studies have revolutionized the field in the last two decades. For example, numerous subclasses of SNe are now known to exist with characteristics spanning faint, fast-declining lightcurves to overluminous, slowly-declining lightcurves relative to normal SNe Ia (Jeffery et al., 1992; Phillips et al., 1992; Filippenko et al., 1992a,b; Li et al., 2003; Branch et al., 2004; Jha et al., 2006a). These data have served as a benchmark in the formation of a picture of the physical systems that constitute the breadth of SNe Ia: progenitor system compositions, thermonuclear explosion mechanisms, atmospheric ionic compositions and velocities, and circumstellar environments. The goal of this spectroscopic research is twofold: to understand the physical systems of SNe Ia in their own right, and to exploit this knowledge in order to improve the utility of SNe Ia as cosmological probes.

1.1 Upcoming SNe Ia Studies

In the coming decades, large photometric surveys are expected to raise the number of SNe Ia with high quality photometry by orders of magnitude. For example, the Large Synoptic Survey Telescope (LSST) collaboration is expected to obtain ground-based optical photometry of $100,000$ SNe Ia out to $z < 1.2$ (LSST Science Collaboration et al., 2009), while the Dark Energy Survey (DES) expects to observe 3000 in the redshift range $0.05 < z < 1.2$ (Bernstein et al., 2012). The enormity of the future sample size promises a realm in which systematic errors of the observations

are the dominant sources of errors in measurements of cosmological parameters.

1.2 Nearby SNe Ia

Very distant SNe Ia are useful as cosmological probes because their recession velocities due to the expansion of the universe are much greater than their peculiar motions. This quality is advantageous for cosmological studies which focus on measuring the expansion, but disadvantageous because the extreme distance makes the events extremely faint and prevents detailed analyses. The opposite is true for nearby SNe Ia ($z < 0.015$), whose peculiar motions are not dwarfed by expansion velocities, and are bright enough to afford detailed (spectroscopic) analyses. Understanding the characteristics of nearby SNe so that this knowledge can be applied to more distant SNe Ia is one of the main goals of this work.

1.2.1 SNe Rest-frame UV

For a normal SN Ia, the majority of the emitted flux is observable in the rest-frame optical, as shown in black in the top panel of Figure 1.1. This is ideal because this portion of the SED is easily observed by ground-based observatories for all but the highest redshift events. For this reason, the vast majority of nearby SNe Ia observations to date have focused on the rest-frame optical regime.

Rest-frame UV light from SNe Ia is more difficult to observe due to the large opacity of the earth's atmosphere in the UV. As a result, ground-based observations are not possible and space-based observations must be utilized to gather useful data at wavelengths shorter than ~ 3300Å. For this reason, UV observations have been much more limited in number than optical observations (see Section 1 of Brown et al. (2014a) for a synopsis of UV SNe photometric observations). Even rarer are UV spectroscopic observations, of which ~ 100 are available (Jeffery et al., 1992; Kirshner et al., 1993; Foley et al., 2008; Bufano et al., 2009; Foley et al., 2012a; Foley

& Kirshner, 2013; Foley et al., 2014; Mazzali et al., 2014).

The UV is an excellent place to observe the primary components of SNe Ia atmospheres. Lines of Fe group ions, the primary nucleosynthesis products of SNe Ia, dominate the UV spectra. UV light also provides the best method of probing and constraining the effects of temperatures and densities within expanding SNe Ia atmospheres, and determining whether UV flux results from escaping photospheric photons or reverse fluorescence in the outermost ejecta layers (Höflich et al., 1998; Mazzali, 2000; Lentz et al., 2001; Sasdelli et al., 2014; Walker et al., 2012; Mazzali et al., 2014). Models suggest that interaction with a non-degenerate companion star should be detectable in the UV at very early times, and thus the UV provides a window into investigating single or double-degenerate progenitor systems (Kasen, 2010; Brown et al., 2012a; Cao et al., 2015). Recently, the subclassification of normal SNe Ia as 'near-UV red' (NUV-red) and 'near-UV blue' (NUV-blue) has reduced the NUV color scatter to a level comparable to the optical, and thus opens the possibility of using the NUV for cosmological investigations (Milne et al., 2013). Also, rest-frame NUV colors suggest that the fraction of NUV-red to NUV-blue SNe Ia evolves with redshift, such that nearby NUV-red are favored 2:1 whereas NUV-blue SNe represent a higher fraction at high-redshift. This observation suggests a monotonic evolution of SNe Ia progenitors and atmospheric characteristics with time (Milne et al., 2015).

One of the goals of this work is to increase the existing sample of rest-frame UV spectrophotometric measurements. We achieve this by reducing, presenting, and analyzing the *Swift* UVOT archive of nearby ($z < 0.02$) SNe Ia observations, which is currently mostly unpublished. We present a new method of decontaminating *Swift* UVOT grism spectra that enabled us to obtain uncontaminated, flux calibrated spectra of 40 of the 91 UVOT spectra we present. Details of the processing of *Swift* UVOT data are presented in Section 2. The compiled UV spectroscopic atlas

and an analysis of the peculiar SN Ia iPTF14bdn is presented in Section 3. In Section 4 we combine the UV data with optical and near-infrared observations, perform an analysis of the UV-O-IR properties and investigate the spectroscopic properties of NUV-red and NUV-blue SNe.

1.3 SN K-corrections

The expansion of the universe has the effect of increasing the wavelength of light as it passes through space-time, known as cosmological redshift. When comparing photometry of nearby (low-redshift) objects to their distant (high-redshift) conterparts, the process of K-correcting is utilized to account for this effect. Thus, calculating K-corrections enables the comparison of photometry sampling roughly equivalent portions of target spectral energy distributions (SEDs). The necessity for this calculation was first noted by Hubble & Humason (1931) following the discovery of the expanding universe, and the subject has since been revisited several times (Humason et al., 1956; Sandage, 1956; Oke & Sandage, 1968; Hogg et al., 2002; Nugent et al., 2002; Hsiao et al., 2007).

With increasing redshift, the rest-frame UV shifts further and further into the ground-based optical. Figure 1.1 demonstrates this effect for SNe Ia at redshifts of $z = 0\,, 0.5\,, 1$ and shows the portions of the SED which are sampled by various photometric filters. It is obvious that for high-z SNe Ia, the rest-frame UV is readily observable by ground-based observatories. In order for meaningful comparisons to be made between low-z and high-z photometry, one must calculate K-corrections to account for the differences in the photometric filter shapes and the regions of the SED which are being measured. One of the goals of this work is to demonstrate UV K-correction calculations using our SED sample. We anticipate that this analysis will be beneficial to the next generation of large surveys, which will measure rest-frame

UV photometry for thousands of SNe Ia.

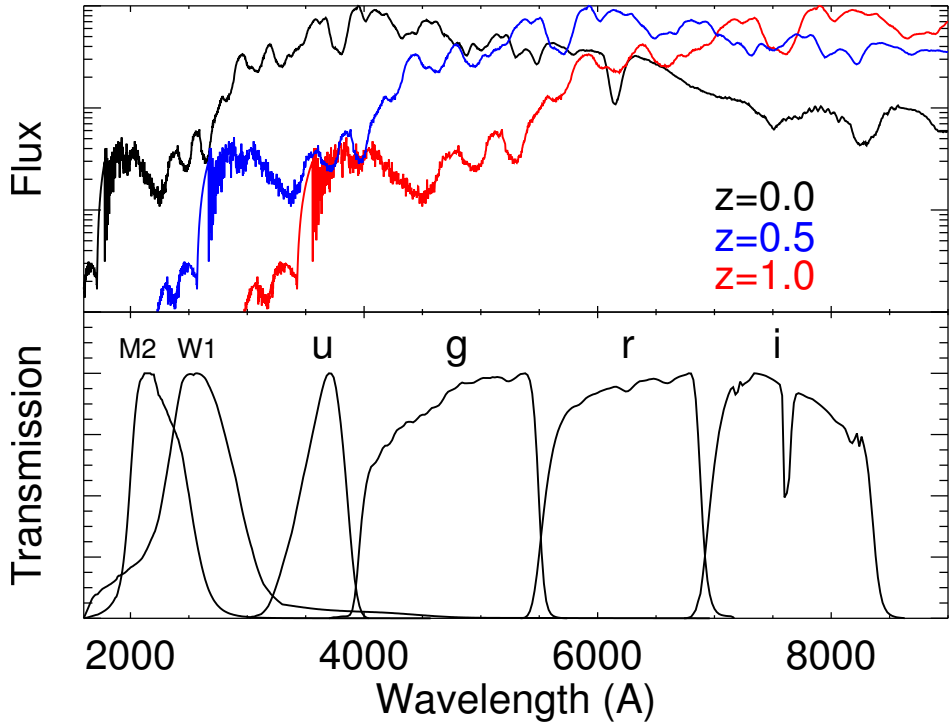

Figure 1.1: Redshift and K-corrections example.

Top: A normal SN Ia spectrum at maximum llight is shown at three redshifts. *Bottom:* normalized *Swift* UVOT and ugri photometric filter transmission functions are shown. The region of a SN SED sampled by each photometric filter is dependent upon the redshift of the SN. Comparisons of SNe photometry from different redshifts are accomplished using the process of K-correcting.

Cross-filter K-corrections have the mathematical form:

$$K_{xy}(z) \;=\; +2.5\,log(1+z) \;-\; 2.5\,log\frac{\int \lambda S_x(\lambda) Z(\lambda) d\lambda}{\int \lambda S_y(\lambda) Z(\lambda) d\lambda} + 2.5\,log\frac{\int \lambda F(\lambda) S_x(\lambda) d\lambda}{\int \lambda F(\lambda/(1+z)) S_y(\lambda) d\lambda} \tag{1.1}$$

where $F(\lambda)$ is the SN SED, $S_x(\lambda)$ and $S_y(\lambda)$ are the effective transmission functions of the x and y bandpasses, $Z(\lambda)$ is an ideal local stellar SED for which all magnitudes are equal to zero, and z is the target object redshift (Kim et al., 1996). The K-correction is applied to the photometry of the x bandpass to convert it to the the y bandpass system as,

$$m_y \;=\; m_x \;+ K_{xy}. \tag{1.2}$$

Inspection of Equation 1.1 makes it immediately clear that a K-correction requires knowledge of the photometric filter bandpasses and the SN SED. It is uncommon that one possesses simultaneous knowledge of an individual SN's photometry and spectrophotometry to calculate an exact K-correction, particularly at high redshifts. So, template SEDs are typically employed in these calculations (Nugent et al., 2002; Hsiao et al., 2007). Supernovae SEDs vary as functions of time and lightcurve stretch. So, an ideal set of template SEDs will cover a wide range of wavelengths and phases for SNe of multiple decline rates. One of the goals of this work is to provide the first set of template SEDs which span the ultraviolet, optical, and near-infrared for normal SNe Ia with decline rates $0.9 > \Delta m_{15}(B) > 1.6$. Our analysis compares the K-corrections calculated using our UV-O-IR SEDs to those calculated using existing templates in the UV and optical spectral ranges.

2. DATA*

The data used in this analysis primarily comes from two sources: 1) the Carnegie Supernova Project (CSP) (Hamuy et al., 2006), and 2) the *Swift* Ultraviolet/Optical Telescope (Gehrels et al., 2004; Roming et al., 2005). Optical and near-infrared data was measured by the CSP, while ultraviolet data was measured using the *Swift* UVOT.

2.1 Carnegie Supernova Project

The CSP I had the goals of providing a large sample of SNe 1) photometric series in a uniform and well-characterized photometric system spanning the wavelengths of ground-based ultraviolet to K-band near-infrared for low-z ($0 < z < 0.07$), and high-z samples ($0.1 < z < 0.7$), and 2) spectroscopic series in the ground-based optical regime for the low-z sample of SNe. The CSP II is an ongoing effort to obtain optical and NIR observations of $100-150$ SNe Ia at redshifts $0.03 < z < 0.08$. Observations of NIR lightcurves and spectra are the main priorities of the CSP II data collection effort. All published CSP data presented herein were obtained from the data products repository of the CSP I at http://csp.obs.carnegiescience.edu/data. Unpublished data were obtained through personal communication with Carlos Contreras and Nidia Morrell.

2.1.1 CSP Photometric System

The CSP photometric system utilizes the filters *uBgVriYJHK*. The photometric system for all filters was first characterized at the time of the first photometric data

*Section 2.2.2.1 is reprinted with permission from "Decontaminating Swift UVOT Grism Observations of Transient Sources," by Smitka et al. (2016). *Publications of the Astronomical Society of the Pacific*, 128, 034501, Copyright 2016 by The Astronomical Society of the Pacific.

release of 35 SNe Ia by Contreras et al. (2010). At the time of the second photometric data release of 50 SNe Ia, the photometric zero-points of the *uBgVri* filters were refined by Stritzinger et al. (2011) using updated response functions which were measured for the telescope-filter-CCD system (Rheault et al., 2010, 2014). Similary, the *YJH* zero-points have been updated and are available on the CSP website.

The CSP defines the zero-points using synthetic photometry, which is the process of convolving the telescope-filter-CCD response functions with a spectrum to simulate photometric observations. Mathematically a synthetic magnitude takes the form,

$$m_{syn} = -2.5\, Log[\, \int_0^\infty S_X(\lambda) F_o(\lambda) \frac{\lambda}{hc} d\lambda\,] + ZP_X, \tag{2.1}$$

where wavelength has units Å, S_X is the photon transmission function of filter X, F_o is the SED of a fiducial source with units erg s^{-1} cm^{-2} Å^{-1}, and ZP$_X$ is a zero-point calculated using the relation,

$$ZP_X = m_o - m_{syn}, \tag{2.2}$$

where m_o is the observed magnitude of this source through the filter X. Addition of the zero-piont term places the synthetic photometry on a standardized photometric system (Strömgren, 1937; Arp, 1961; Bessell, 1990; Straizys, 1996; Schmidt et al., 1998).

In order to fully utilize the CSP photometric data while retaining the precision of the photometric system, we were required to encode a synthetic photometry system that behaves very similarly to the published photometric system. The *synth.pro* software routine achieved this and was confirmed to perform accurate calculations by recreating the zero-point calculations outlined in the photometric system documentation Contreras et al. (2010); Stritzinger et al. (2011). The normalized filter

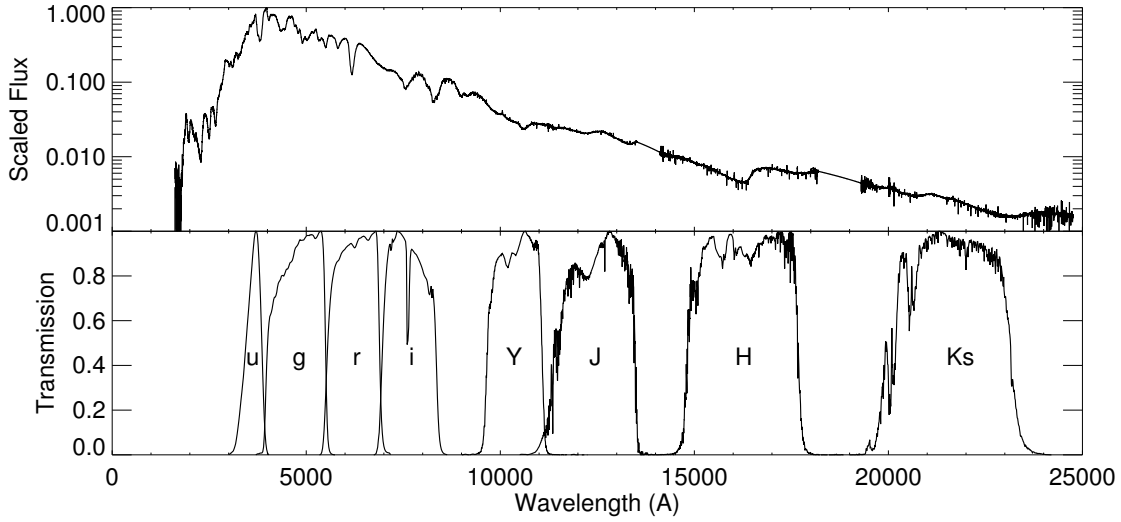

Figure 2.1: Normalized CSP photometric filters.
A SNe Ia SED is shown to demonstrate the SED regions to which each filter is sensitive. The B and V filters are not shown here to avoid overlap.

response functions are shown in Figure 2.1 to exemplify the regions of a SNe Ia SED to which each filter is sensitive.

2.1.1.1 BV Photometry

The it B and V systems of the CSP are defined on the Vega system and the most recent CSP system calibration is defined by Stritzinger et al. (2011). This calibration utilizes the Vega magnitudes in the standard system $B_{std} = 0.03$ and $V_{std} = 0.03$ (Fukugita et al., 1996) transformed onto the Swope telescope natural system: $B_{nat} = 0.03$ and $V_{nat} = 0.009$ (Contreras et al., 2010; Stritzinger et al., 2011). All CSP photometry is published in the Swope natural system. Using the Vega SED (version 5) of Bohlin & Gilliland (2004b) from CALSPEC and the filter response functions, we calculated zeropoints shown in Table 2.1. Agreement within 0.001 mags of the published values is demonstrated.

Table 2.1: CSP photometric system zeropoints.
A comparision of published CSP photometric zero-points with those calculated using our *synth.pro* software. These calculations were performed as confirmation the accuracy of our replication of the published systems.

System	Filter	Published Zero-point	Our Zero-point	Source
CSP	u	13.044	13.048	Stritzinger et al. (2011)
CSP	B	14.344	14.344	Stritzinger et al. (2011)
CSP	g	15.135	13.139	Stritzinger et al. (2011)
CSP	V	14.450	14.451	Stritzinger et al. (2011)
CSP	r	14.915	14.914	Stritzinger et al. (2011)
CSP	i	14.781	14.783	Stritzinger et al. (2011)
CSP	Y	12.687	12.687	Contreras et al. (2010)
CSP	J	12.853	12.853	Contreras et al. (2010)
CSP	H	12.555	12.555	Contreras et al. (2010)
CSP	K	11.967	11.968	Contreras et al. (2010)

2.1.1.2 ugri Photometry

The *ugri* systems of the CSP are defined on the SDSS standard calibrator $BD+17°4708$ system. The most recent CSP system calibration is defined by Stritzinger et al. (2011). This calibration utilizes the $BD+17°4708$ magnitudes of Smith et al. (2002). Using the $BD+17°4708$ SED of Bohlin & Gilliland (2004a) and the filter response functions we calculated zeropoints shown in Table 2.1. Agreement within 0.004 mags of the published values is demonstrated.

2.1.1.3 YJHK Photometry

The *YJHK* systems of the CSP are defined on the Vega system and the most recent CSP system calibration is defined by Contreras et al. (2010). This calibration utilizes the Vega magnitudes of Cohen et al. (1999) for *JHK* and that of Hamuy et al. (2006) for *Y*. Using the Vega SED (version 5) of Bohlin & Gilliland (2004b) and the filter response functions we calculated zeropoints shown in Table 2.1. Agreement within 0.001 mags of the published values is demonstrated.

2.1.2 CSP Spectroscopy

The main source of optical spectra used herein are derived from the CSP data products repository. To date, the CSP has released 832 individual spectra of 93 SNe Ia at $z < 0.1$ (Folatelli et al., 2013). These spectra span epochs of -12 to $+150$ days relative to B-band maximum brightness with typical wavelength coverage of $3500 - 9500$ Å. This wavelength coverage ensures that the majority of the total UV-O-IR energy output of low-z SNe Ia is encompassed within these spectra. All of the SNe Ia observed spectroscopically were also observed photometrically. The spectra were published without being flux calibrated onto an absolute system; we place the spectra onto the CSP system using color-matching which utilizes the photometric colors, our synthetic photometry routine, filter transmission functions, and the photometric zeropoints (Section 4.3). A complete listing of the SNe with published spectra is found in Table 1 of Folatelli et al. (2013). Telluric features were removed using observations of standards each night. Additional details of the spectroscopic observation facilities and reduction methods are presented in Hamuy et al. (2006) and Folatelli et al. (2013) and will not be discussed further here.

2.2 *Swift* UVOT

The UVOT is a $30\,cm$ telescope and instrument onboard the *Swift* space telescope possessing both photometric and grism spectroscopic observing modes. It is sensitive to wavelengths $1600 - 6500\,$Å. *Swift* UVOT and the Hubble Space Telescope are currently the only observatories with the capacity to observe the space ultraviolet, and data gathered are accordingly valuable. The analysis presented herein incorporates data from both the photometric and spectroscopic modes.

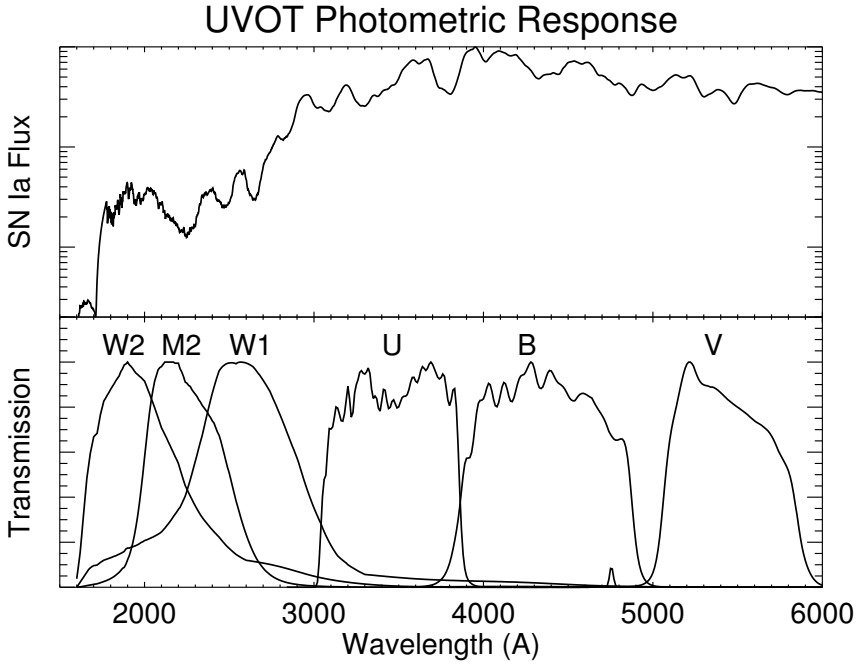

Figure 2.2: Normalized *Swift* UVOT photometric filters.
A SNe Ia SED is shown to demonstrate the SED regions to which each filter is sensitive.

2.2.1 UVOT Photometry

In photometric mode, UVOT has six filters available: *UVW2, UVM2, UVW1*, U_{sw}, B_{sw}, V_{sw}. The normalized filter response functions are shown in Figure 2.2 to exemplify the regions of a SNe Ia SED to which each filter is sensitive. Details of the processing of UVOT SNe photometry and a photometric archive reduced using the standard methods are described in detail in Brown et al. (2014a). All UVOT photometry used herein was drawn from this archive by means of the website, http://people.physics.tamu.edu/pbrown/SwiftSN/swift_sn.html.

As was the case with the CSP photometry, we ensured that our UVOT synthetic photometry system was in agreement with the most recent published calibrations. We

obtained the most recent UVOT filter response functions from the NASA HEASARC archive (Poole et al., 2008; Breeveld et al., 2011).

2.2.1.1 UVOT UVB Photometry

The calibration of the UVOT $U_{sw}V_{sw}B_{sw}$ photometry is detailed by Poole et al. (2008). The calibration is defined using different sets of standard stars for each filter using the standards of Landolt (1992); Colina & Bohlin (1994) and white dwarves of the HST MAST archive. The sets of stars used in each filter's calibration is presented in Table 2 of Poole et al. (2008), which contains an overview of the zero-point calibration procedure as well. The zero-pointing procedure consists of calculating the zero-points of roughly 10 stars in each filter and averaging the results to determine the final zero-point values.

We obtained the SEDs of these stars and recreated the calibration procedure using our synth.pro software. A complication arose during this phase due to the fact that spectra of the photometric standards of Landolt (1992) are not available. To remedy this problem, Poole et al. (2008) used spectral representations of the Landolt (1992) photometric standards taken from the spectral type classification catalog spectra of Pickles (1998). The exact spectral templates used by Poole et al. (2008) are not documented, so in our calibration procedure for each Landolt (1992) standard star we adopted the Pickles (1998) SED with the most similar synthetic $(B-V)$ and $(U-B)$ colors of the same spectroscopic class.

Upon comparing our calculated zero-point values with those of Poole et al. (2008) we found agreement within 0.01 mags. This confirmed that our software was working properly in both the CSP and UVOT systems. Because of the ambiguity associated with the process of assigning SEDs to the Landolt (1992) photometric standards, we decided to adopt the published zero-point values in our software implementation.

Table 2.2: *Swift* UVOT photometric zeropoints.
UV synthetic magnitudes of Vega calculated using our *synth.pro* software. These values have had the indicated zero-points applied.

System	Filter	Synthetic Magnitude	Zeropoint	Zeropoint Source
UVOT	U_{sw}	-0.003	18.34	Poole et al. (2008)
UVOT	B_{sw}	-0.006	19.11	Poole et al. (2008)
UVOT	V_{sw}	0.001	17.89	Poole et al. (2008)
UVOT	*UVW2*	-0.003	17.38	Breeveld et al. (2011)
UVOT	*UVM2*	0.000	16.85	Breeveld et al. (2011)
UVOT	*UVW1*	-0.002	17.44	Breeveld et al. (2011)

This was decided to avoid any systematic bias in the zero-point values ($\sim$ 0.005 mag), which may have arisen due to differences in SED selection. As a check of the accuracy of this assumption we performed synthetic photometry of the Vega SED and applied the published zero-point values. Our calculated Vega magnitudes (accurate within 0.006 mags), and the published zero-point values are presented in Table 2.2.

2.2.1.2 UVOT UVW2, UVM2, UVW1 Photometry

The original *UVW2, UVM2, and UVW1* filter response functions presented by Poole et al. (2008) were based on observations of three white dwarf standard stars observed early in the *Swift* mission. This functions were later updated by Breeveld et al. (2011) to include additional white dwarf observations as well as standard stars with a wider range of colors (12 standard stars in total). This recalibration also included a redetermination of the photometric zero-points. The recalibration process used by Breeveld et al. (2011) utilized a SED of Vega and a correction factor to account for the photon counting nature of the UVOT detector, which was not available to us. For this reason, we were unable to recreate the calibration for these filters. Because of the confirmed success of our software in the other photometric regimes, we thought it was prudent to simply adopt the published zero-point values. As a

check of the accuracy of this assumption, we performed synthetic photometry of the Vega SED and applied the published zero-point values. In Table 2.2 we demonstrate that our calculated Vega magnitudes are witihin 0.003 mags of defined zero value.

2.2.2 UVOT Spectroscopy

The UVOT instrument has two slitless spectroscopic grisms: the UV and V-grisms. The UV-grism is designed for observing within the wavelength range $1700 - 5000$ Å and the V-grism $2850 - 6600$ Å (Kuin et al., 2015). In practice, the UV-grism is heavily favored because it is sensitive to a larger range of wavelengths not accessible to ground-based observatories. The UV-grism has an average resolution of $3\ \mathring{A}\ pix^{-1}$. *Swift's* fast targeting and flexible scheduling are inherent to its primary mission as a gamma-ray burst observatory, and give the UVOT instrument the ability to target objects with just a few hours notice. These qualities make an UVOT instrument ideal for studying the early evolution of transient objects in the UV, which are otherwise difficult or impossible to observe.

The Hubble Space Telescope (HST) is the only other existing obseravtory capable of measuring UV spectra. Compared to *Swift* UVOT, HST Space Telescope Imaging Spectrograph (STIS) spectra of SNe benefit from: a larger telescope aperture, a slit for reducing contamination from the SN host galaxy and nearby field objects, a factor of ~ 2 times better resolution in the UV, an absolute flux calibration of 5% (10% for UVOT), and a sensitivity lower limit of 1200Å (1700Å for UVOT) (Bostroem & Proffitt, 2011; Kuin et al., 2015). For these reasons, HST spectra are more desirable than UVOT spectra. However, HST has the disadvantages of schedule oversubscription and slower response time (~ 1 week between observation request and acquisition). For these reasons, HST spectra are more difficult to obtain, fewer in number, and biased against the pre-maximum light epochs when SNe Ia UV light

comprises a greater proportion of the total flux and the features are evolving the fastest.

Both grisms have the ability to observe in either nominal or clocked mode. Clocking is an observing mode in which the filter wheel containing the grisms is positioned to partially obscure the light path such that the diffracted spectrum of interest falls upon a region of the detector that is not exposed to the target field. Using this procedure $\sim \frac{2}{3}$ of a typical spectrum's wavelength range falls upon the obscured portion of the detector while the remaining $\sim \frac{1}{3}$ falls upon a portion of detector exposed to the target field. For the UV-grism the region of the spectrum which falls on this sky-illuminated region is the shortest wavelength region ($1700 - 3000\,\text{Å}$.) Clocked mode is most often used because it prevents projecting the redder portion of the diffracted spectrum of interest on top of nearby contaminant sources, and it provides a lower background and thus smaller coincidence loss correction (Kuin et al., 2015).

Since shortly after its launch in 2004, *Swift* UVOT has been observing supernovae photometry and spectra. To date ~ 30 SNe Ia and ~ 20 core collapse SNe have been targeted for grism observations. Despite the large number of targets, the number of published UVOT spectra of SNe remains quite small (Bufano et al., 2009; Foley et al., 2012a; Bayless et al., 2013; Brown et al., 2014c, 2015a; Margutti et al., 2014). This is partly due to the fact that roughly half of the SNe Ia grism observations contain contamination which cannot be removed using the normal image processing methods, and thus render the final spectral features and flux calibrations suspect or useless. Because SNe Ia are transient objects, the contaminated data cannot be re-observed and are thus lost if the contaminating background sources cannot be removed. Because of the high value of space-based UV spectral observations and our desire to incorporate the UVOT spectra into our study of UV-O-IR SNe, we opted to develop a method of removing as much of the contamination as possible. To do

this and make more of the sample of grism observations of SNe available for analysis we have developed an empirical decontamination technique for *Swift* UVOT grism images. The process is akin to image subtraction for direct images and thus requires that any sources of contamination remain unchanged between data and template image acquisitions.

2.2.2.1 The UVOT Grism Decontamination Process

The process of decontaminating the UVOT grism spectra consists of four main steps: 1) template observation, 2) template registration, 3) flux scaling, and 4) spectral extraction. This process is described in explicit detail in Smitka et al. (2016).

- *Template observation:* our empirical decontamination technique requires that UVOT observe template images which reproduce the original data observations as closely as possible. A template image is a grism image observed after the target flux has sufficiently faded.

- *Template registration:* this process is necessary because the pointing differences between exposures can vary by up to one arcminute ($\sim$ 100 pixels). As a result, this process must be carried out individually for each exposure (UVOT observations typically consist of multiple 'snapshots' which are coadded in processing). A simple translation of the template detector image is all that is necessary. Translations are typically 100 pixels or fewer in each dimension when the templates are observed as outlined in Smitka et al. (2016). Translations greater than this amount should be avoided due to the spatially varying sensitivity of the detector. The flux calibration of Kuin et al. (2015) accounts for the overall spatial variation of the detector, but not for the difference in sensitivity resulting from the data and template images being slightly offset.

For clocked UV-grism template images with an offset of 100 pixels or fewer we estimate that the uncertainty in measured flux introduced by the registration process is 3% or less.

- *Flux scaling:* the registered template image must be flux scaled to account for differences in the integration times of the data images and the template image. The purpose of this step is to scale the flux on the template image such that sources of constant brightness have equivalent counts in both data image and the scaled template image. This step can be avoided if the integration time of both the data and template images are identical. A simple multiplicative scaling of the counts on the registered template detector image is all that is required. The scaling factor is calculated as the ratio of the exposure times of the template and data images.

  In some cases an additional small flux scaling factor is necessary to account for the $\sim 1\%$ per year sensitivity loss of the UVOT detector (Breeveld et al., 2011). This is typically required in cases where a sufficiently long span of time elapses between the data and template observations that the UVOT sensitivity changed significantly. In these cases, the correction accounts for a slight faintness of the template image relative to the data image. In practice, this effect can be corrected 1) theoretically by assuming a value for sensitivity loss as a function of time and multiplying the template image by the factor and length of time elapsed between observations, or 2) empirically by measuring fluxes of constant brightness sources in both images, calculating a flux ratio of the two and multiplying this factor into the template image.

- *Extraction:* The UVOTPY software (Kuin et al., 2015) for extracting, flux calibrating and wavelength calibrating UVOT grim spectra includes an option

to supply an external background image, yet does so in a way that accurately calculates coincidence loss for the UVOT detector. The change from the typical extraction process lies in how the measurement of the background is performed. In a typical UVOTPY extraction the background flux imposed on the target spectrum is not directly measured, but is estimated from the flux contained in channels lying parallel to the dispersion direction directly above and below the channel containing the target spectrum. The background flux along the dispersion direction is then calculated from the sigma clipped mean to remove bright sources lying within the channels. Next, the smoothed flux within these channels and the coincidence loss is calculated using the flux within the extraction channel plus the background estimate. The corrected background is then subtracted from the total flux to obtain the coincidence loss corrected target flux. When the empirical decontamination technique is used, the contaminant flux for each pixel is measured directly from the corresponding sky location on the registered and scaled template image. The coincidence loss is then calculated using the total flux from the extraction channel on the data image and for the background measurement from the extraction channel on the template image. The flux errors are based on the total flux in the target spectrum and that from the template image. The primary benefit of this process is that it decouples the flux of the target object from any underlying sources within the extraction channel while properly correcting for the effect of coincidence loss on the detector due to both target and contaminant photons.

The extraction process described above is necessary due to the photon counting nature of the UVOT detector and the non-linear nature of the coincidence loss correction. The UVOT detector does not directly measure incident photons,

but rather incident photons interact with a photocathode which produces a cascade of photons that is recorded as a splash on the detector. A centroiding process of the splash then calculates the spatial location of the incident photon. Coincidence loss occurs for bright sources as a result of the UVOT detector's finite frame time while recording these splashes. When multiple photons are incident upon the photocathode during an individual readout frame the multiple splashes can be recorded as a single splash if the incident spatial locations are near each other. When this occurs, photons remain uncounted and bright fluxes are innacurately measured. If a correction is not applied, the corresponding flux measurement will underestimate the true flux of the source. The coincidence loss correction for all UVOT grism spectra is performed by the UVOTPY extraction software and is documented in detail in Kuin et al. (2015).

2.2.2.2 Verification of the UVOT Decontamination Process

Supernova 2011fe data affords us the opportunity to demonstrate the accuracy of the flux recovery from the SN using our empirical decontamination technique. Due to its location in the nearby galaxy M101, SN 2011fe was a very bright SNe Ia. For this reason it was heavily monitored by several observatories, including both the *Hubble Space Telescope* (*HST*) Space Telescope Imaging Spectrograph (STIS) (Mazzali et al., 2014) and *Swift* UVOT (Brown et al., 2012b). The UV slit spectra of SN 2011fe obtained using STIS are superior to those of UVOT because *HST* has a much larger aperture, the high spatial resolution and narrow slit produce spectra free of contamination and have an absolute flux calibration accurate to 5% (Bostroem & Proffitt, 2011) and can thus be used as benchmarks for comparison.

The UVOT spectra of SN 2011fe exhibit more contamination than any other SN

observed with UVOT. As a result of the proximity of the host galaxy, the location of the SN within the galaxy, and *Swift*'s roll angle availability, the grism images exhibit both types of contamination described above. In all observations, the first order spectra are projected on top of resolved zeroth order and dispersed galaxy features and the background measurement channels near the diffracted spectra contain both diffracted and zeroth order light from clumpy sources (Figure 2.3.) Using normal UVOTPY extraction procedures the SN and host galaxy fluxes cannot be decoupled and all SN spectral information blueward of 2500 Å is contaminated. In this region one does not know a priori which extracted spectral features are from the SN and which are from the galaxy. However, SN 2011fe template images contain only the underlying galactic flux and the STIS spectra contain only the SN flux, so in this case we can test the ability of our empirical decontamination technique to decouple the SN and host galaxy fluxes while assessing the accuracy of the recovered SN flux.

We carried out our empirical decontamination technique using the clocked UVOT UV-grism data of SN 2011fe observed on 2011 September 10 (obsid: 00032094004) and the template we observed as a *Swift* target of opportunity two years after the initial observations on 2013 September 11 (obsid: 00032094018). For the template images the pointing of the spacecraft was recreated to within 30 arcsec in both RA and dec and within 4.5 arcmin in roll angle. At the time of the original observation the SN was at a phase of 0.11 days past B-band maximum light. We chose this epoch for analysis because simultaneous STIS spectra exist and provide us with a benchmark for comparison. Figure 2.4 shows that we were able to decouple the SN from the contaminant fluxes and demonstrate agreement between the calibrated UVOT and STIS SN fluxes as blueward as 2000 Å. After subtraction of the host galaxy flux, there is little flux remaining from the supernova shortward of 2500 Å. In the absence of HST/STIS or subtracted UVOT spectra, the strong features in the

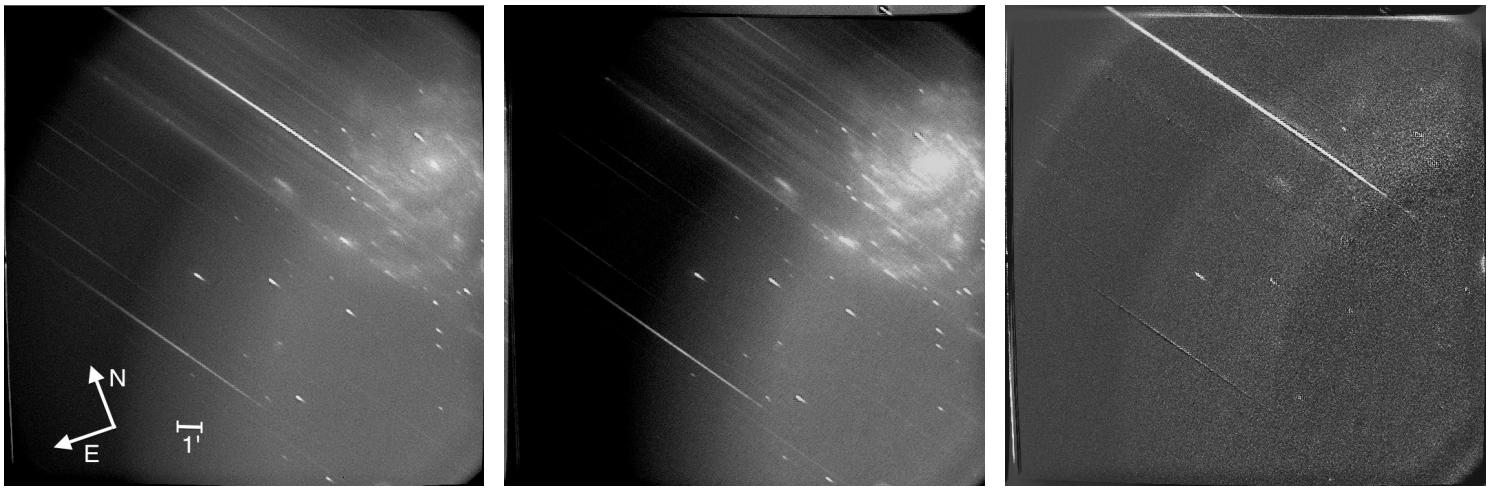

Figure 2.3: Emperical decontamination concept.
Swift UVOT U-grism images. *Left:* A data image of SN 2011fe. The zeroth order image of SN 2011fe lies just outside of the frame to the right, the first order diffracted spectrum is the brightest feature and appears partially overlaid on the host galaxy M101. Wavelength of the diffracted spectrum increases from bottom right to upper left. *Center:* A registered and flux-scaled template image for SN 2011fe. This image was taken two years after the SN data images. *Right:* The residual of subtracting the registered and flux-scaled template image from the SN data image. The SN light is decoupled from the galaxy light.

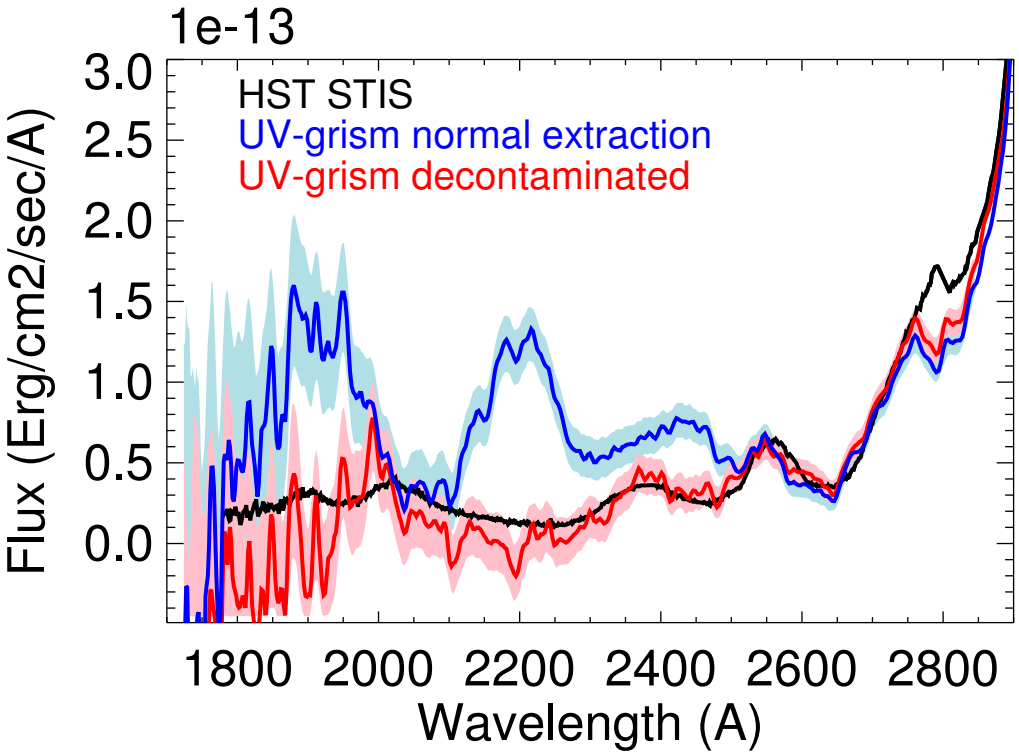

Figure 2.4: Emperical decontamination flux calibration.
Swift UVOT U-grism spectra of SN 2011fe extracted using the normal UVOTPY method and our empirical decontamination technique are compared to *HST* STIS spectra. The UVOT and STIS spectra were gathered just hours apart while the SN was very near maximum brightness. The contamination to the UV portion of the UVOT spectrum (blue) is removed and the agreement with the STIS spectrum is improved (red). The noise at the shortest wavelengths is due to a combination of low photon rates and decreased detector sensitivity.

unsubtracted spectra could have been misinterpreted as coming from the SN and therefore resulted in unnecessary (and incorrect) theoretical interpretations.

2.2.2.3 Treatment of Errors

The UVOT is a photon counting instrument, where each imaging observation is made up of a finite number of frames. This means that the errors follow a Poison distribution as long as the number of counts per pixel in an observation is much

smaller than the number of frames. In cases where this is not so, the errors need to be computed according to the formalism presented in Kuin & Rosen (2008).

The treatment of errors is implemented within the UVOTPY software. Since the observed spectrum is determined by subtracting a background, the total error in the observed spectrum is the root mean square sum of the errors in background and spectrum. The same procedure is employed for both the default background produced in UVOTPY (described in Kuin et al. (2015)) and for the background supplied from matching a late-time observation of the field in its place.

In the case of spectral extraction, UVOTPY resamples the spectrum while rotating the image for extractions (see Kuin et al. (2015)). As a result, a correlation is introduced between the errors in neighboring spectral bins. Tests show that assuming three bins are correlated will bring the values of the χ-squared test to the expected values (Kuin et al., 2009).

The empirical decontamination technique works similarly as when using the normal UVOTPY method in which the background is estimated by sigma clipping and smoothing the original image. For the following discussion we will assume that the changes in the field are only due to the fading away of the transient object spectrum. The normal UVOTPY background, being an extrapolation from nearby regions, is almost certainly less accurate because the transient spectrum may lie in pixels also containing light from weak sources. This includes either zeroth or first order light, which cannot be removed (see the spectra of SN 2010ev and SN 2012cg in the Appendix for examples.) Also, the opposite may be true where the spectrum lies over a slightly less crowded part of the background (see the spectra of SN 2005df in the Appendix for an example.) The estimation of the normal UVOTPY background also becomes less accurate when the source is near a number of strong first order spectra. These are all systematic errors above the Poisson errors mentioned already.

The method of this paper does not suffer from these kinds of systematic errors. The gain is mainly obtained where the spectrum is up to 10 sigma above the background noise, but also in removing weak underlying zeroth and first order contaminations. The contaminating source count rate raises the count rates in the supplied background and the errors are correctly treated for the higher contribution from the contaminating source. Surprisingly, in the UVOTPY spectral extraction the same contaminating source count rate will be added to the source spectrum and add to the random error there (as well as being an unidentified systematic error), so the difference in the size of the random error between the two methods is small. However, the difference and advantage lies in removing the systematic errors by using the empirical decontamination technique.

Coincidence loss, has a spatial component that affects the spectral profile when very large. The reason lies in the photon splash centroiding which is based on three physical detector pixels - equal to 24 (sub)pixels (Roming et al., 2005) - and the coincidence loss affects the centroiding. As a result, for very bright sources, a zeroth order field star near the target spectrum will have a large error or become unrecoverable (see the discussion of SN 2012dn in the Appendix for an example.) When extremely strong contamination is present both the normal UVOTPY extraction and the empirical decontamination technique cannot recover the affected portions of the spectrum. In the UVOT grism calibration documentation, Kuin et al. (2015) determined that the coincidence loss correction is found as a best fit to a set of calibration observations. For large count rates, where the total count rate in the spectrum needs to be regarded, the error increases. A limiting count rate equivalent to 0.97 counts per bin per frame was selected as an upper limit as above that rate the error in the coincidence loss correction became much larger than 20%. For a more detailed description of the coincidence loss correction the reader is referred to Kuin et al.

(2015), section 7.

2.2.2.4 TRUVOT Software

We have designed the TRUVOT software pipeline to perform our empirical decontamination technique. The pipeline consists of IDL and UVOTPY Python routines. This software and a working example of the SN 2011fe empirical decontamination extraction of Section 2.2.2.2 is available at http://github.com/mikesmitka/truvot. The software is also available in the UVOTPY distribution.

2.3 Near-Infrared SEDs

The sample of NIR SEDs of SNe Ia available in the literature is sparse. The CSP II observed a large sample of time-series, NIR SEDs, but these were not available for use at the time this work was undertaken. For this reason, the majority of NIR SEDs that we adopt for our bolometric SED and lightcurve analysis are the SNe Ia time-evolution templates of Hsiao et al. (2007). Additionally, spectroscopic observations from the NASA Infrared Telescope Facility of SNe 2005am, 2008hv, and 2008ec were employed as well (Howie Marion, private communication).

3. THE UV SPECTRAL ATLAS*

Using the standard UVOT spectral extraction method of Kuin et al. (2015) and our decontamination method described in Section 2, we have processed the full sample of SNe Ia observed by the UVOT grisms to date: 91 spectra of 21 SNe. Details of the individual spectra and the extraction processes used in each case are presented in the Appendices. Appendix A contains spectra extracted using our decontamination procedure, while Appendix B contains spectra using the normal UVOTPY extraction procedure. Table 3.1 presents the optical decline rates, optical classifications, and UV subclassifications for all of the SNe in our sample.

As stated in Section 2.2.2, some UVOT spectra of SNe Ia have been previously published. These spectra are included in our spectral atlas for two reasons. First, the UVOTPY software (Kuin et al., 2015) is designed solely for the purpose of performing robust and standardized extractions and calibrations (wavelength and flux) of UVOT grism spectral data. Due to the large time commitment required to author software of this nature, the full data reduction pipeline has only become available in the last few years. This means that the previously published spectra have been published using differing extraction methods, and thus may have systematic differences in their wavelength and flux calibrations, (see Bufano et al. (2009); Foley et al. (2012a) for more details about SNe 2005am and 2009ig). By extracting these data using the most up-to-date methods and software, we are ensuring a standardized data set in compliance with our best understanding of the UVOT instrument. Second, the UVOT grism decontamination process (Section 2.2.2.1) provides flux calibrated

*Section 3.1 is reprinted with permission from "The 1999aa-like Type Ia Supernova iPTF14bdn in the Ultraviolet and Optical," by Smitka et al. (2015). *The Astrophysical Journal*, 813, 30, Copyright 2015 by The American Astronomical Society.

Table 3.1: UV spectral atlas SNe Ia details.

SN	$\Delta m_{15}(B)$	$\Delta m_{15}(B)$ Source	Optical Class	Optical Class Source	UV Subclass [‡]
2005am	1.514(076)	Folatelli et al. (2013)	Normal	Folatelli et al. (2013)	...
2005cf	1.11(10)	Milne et al. (2010)	Normal	Milne et al. (2010)	NUV-red
2005df	1.2(1)	Milne et al. (2010)	Normal	Milne et al. (2010)	NUV-red
2005ke	1.762(048)	Folatelli et al. (2013)	1991bg-like	Folatelli et al. (2013)	...
2006ej	1.297(055)	Folatelli et al. (2013)	Normal	Folatelli et al. (2013)	MUV-blue
2007sr	0.919(039)	Folatelli et al. (2013)	Normal	Folatelli et al. (2013)	NUV-red
2008Q	1.40(05)	Brown et al. (2010)	Normal	Milne et al. (2013)	NUV-blue
2009an	1.20(05)	Milne et al. (2013)	Normal	Milne et al. (2013)	NUV-red
2009dc	0.72(03)	Silverman et al. (2011)	Super-Ch	Silverman et al. (2011)	NUV-blue
2009ig	0.89(05)	Foley et al. (2012a)	Normal	Foley et al. (2012a)	Irregular
2009Y	0.883(057)	Folatelli et al. (2013)	Normal	Folatelli et al. (2013)	...
2010ev	1.12(02)	Gutiérrez et al. (2016)	Normal	Gutiérrez et al. (2016)	...
2011ao	1.03(05)	This publication*	Normal	Sahu & Arora (2011)	...
2011by	1.14(05)	Milne et al. (2013)	Normal	Milne et al. (2013)	NUV-blue
2011fe	1.21(03)	Munari et al. (2013)	Normal	Munari et al. (2013)	NUV-blue
2011iv	1.69(05)	Foley et al. (2012b)	Normal	Foley et al. (2012b)	...
2012cg	1.039(010)	Munari et al. (2013)	1999aa-like [††]	Silverman et al. (2012b)	...
2012dn	1.08(03)	Brown et al. (2014c)	Super-Ch	Brown et al. (2014c)	...
2012fr	0.85(05)	Zhang et al. (2014)	Normal[†]	Childress et al. (2013)	...
2012ht	1.39(05)	Yamanaka et al. (2014)	2004eo-like	Yamanaka et al. (2014)	...
2013aa	0.97(06)	This publication*	...	...	...
iPTF14bdn	0.84(05)	Smitka et al. (2015)	1999aa-like	Smitka et al. (2015)	...
2014J	1.14(10)	Brown et al. (2015b)	Normal	Ashall et al. (2014)	...

* Lightcurve fits were performed using SNooPy on UVOT U, B, V photometry.
† Zhang et al. (2014) classify 2012fr as 1991T-like.
†† The large $\Delta m_{15}(B)$ of SN 2012cg is not typical of the 1999aa-like classification.
‡ Classified by Milne et al. (2013).

spectra free of UV contamination. By decontaminating the spectra of some previously published SNe and re-publishing the data, we allow for more definitive analyses to be performed.

Table 3.1 shows that our UV spectral atlas contains SNe of a multitude of optical and UV photometric classifications. Detailed analyses of these data has the potential to quantify the UV spectral differences present among the classes and to reveal details of the underlying physical systems. Some analyses of these data are already complete. Brown et al. (2014b) compared spectra of the highly extincted SN 2014J to SNe 2011fe and 2012fr and concluded that the attenuated UV and optical light from SN 2014J was consistent with an extinction law with $R_V = 1.4$ resulting from interaction with interstellar dust. Also, the work of Brown et al. (2014c) found overluminous UV absolute magnitudes for three Super-Chandresekhar SNe Ia candidates. In this analysis, the spectra of 2009dc and 2012dn hint that this behavior may be due to strong features near 2600Å resulting from higher temperatures and lower opacity in the SN ejecta. This interpretation was favored over the alternative possibility in which the UV excess results from hot, smooth blackbody emission due to shock interaction with a companion star.

In this dissertation, we perform two additional analyses utilizing data from our UV spectral atlas. First, we compare the UV evolution of the peculiar iPTF14bdn to that of normal SNe. Second, we compare the UV features of SNe photometrically classified as NUV-red and NUV-blue.

3.1 The Peculiar SN Ia iPTF14bdn

While the rest-frame ultraviolet regime doesn't presently appear to provide useful standard candles due to greater scatter in UV absolute magnitudes and colors (Jha et al., 2006b; Brown et al., 2010), it has provided new insights into normal SNe

Ia physics, practical means of subclassifying normal SNe Ia and better methods of identifying peculiar SNe Ia than are apparent in the optical. The finding of Milne et al. (2013, 2015) that optically normal SNe can be subclassified into near-UV red and near-UV blue categories exemplifies color differences among SNe which only become apparent when looking in the UV and provides a possible means of utilizing the rest-frame UV as a cosmological probe. Additionally, Brown et al. (2014c) and Brown (2014) have shown that with decreasing wavelength into the UV, the deviant behavior of some peculiar SNe Ia towards brighter absolute magnitudes and bluer colors increases. Explanations for this UV excess cite evidence of an interaction of the SN ejecta with a companion star and the possibility of masses in excess of the Chandrasekhar limit (Howell et al., 2006; Brown et al., 2014c). In the case of so called 'super-Chandrasekhar SNe,' the overluminous behavior is sometimes only detected in the UV absolute magnitudes and not the optical, thus stressing the importance of understanding the rest-frame UV for peculiar SNe Ia. As large ground-based surveys like DES and LSST detect SNe Ia at higher and higher redshifts knowledge of the rest-frame UV will be crucial in interpreting their observations.

Peculiar SNe Ia are classified by how their light curve shapes, luminosities, and spectral features differ from normal SNe Ia. The peculiar 1991T-like SN subclassification is defined in the optical by overluminous, slowly declining light curves, weak or no Ca II and Si II absorption at epochs earlier than $\sim +1$ week, and strong Fe III absorption (Filippenko et al., 1992a; Phillips et al., 1992). The peculiar 1999aa-like SNe classification is similar to 1991T-like with the subtle differences of having weak signatures of Ca II H & K and Si II absorption prior to maximum light (Garavini et al., 2004). From optical observations, possible explanations of the peculiar behavior of both classes include abnormal surface abundances, progenitor deflagration or delayed detonation, and higher than normal photospheric temperatures (Phillips

et al., 1992; Garavini et al., 2004; Sasdelli et al., 2014). Few UV observations exist for these SNe. Jeffery et al. (1992) presented three near-maximum *IUE* spectra of 1991T and found a suitable model where the outer envelope is dominated with newly synthesized Ni and Co. *Swift* UV photometry as early as -7 days of two 1991T-like SNe has shown brighter than normal UV absolute magnitudes, roughly normal color evolution in the NUV and hints of bluer than normal colors in the mid-UV (Brown et al., 2014c).

We present UV and optical photometry and spectral series of iPTF14bdn, a high-luminosity 1999aa-like SN Ia, observed using the Ultraviolet/Optical Telescope (UVOT) (Roming et al., 2005) onboard the *Swift* spacecraft (Gehrels et al., 2004) and the Lijiang 2.4 meter telescope. The UV data comprise the first published UV photometric and spectral series of a 1999aa-like SN Ia. In Section 3.1.1 we present the UV and optical photometry and spectroscopy of iPTF14bdn. We present light curves, UV colors, compare the UV spectra to those of normal SNe Ia and to the bluest rest-frame spectral observations of 1991T-like SNe and present SYNAPPS ion analysis of the spectra. We discuss the origins of the early-time UV flux and the *I*-band secondary maximum.

3.1.1 Observations of iPTF14bdn

iPTF14bdn (Cao et al., 2014) was discovered in UGC 8503 ($z = 0.01558$) (Adelman-McCarthy et al., 2007) on 2014 May 27.40 by the intermediate Palomar Transient Factory (Law et al., 2009) at a phase of 18 days prior to *B*-band maximum light and identified as a 1991T-like or 1999aa-like SN Ia by a weak Si II 6155 Å feature. No comment was made on the presence of a Ca II H & K feature to distinguish between classification as 1991T-like or 1999aa-like in the discovery announcement. No sign of strong extinction was reported in the discovery spectrum nor observed later by us.

Table 3.2: Photometry of iPTF14bdn.
The full version of this table is available in Smitka et al. (2015).

Filter	MJD	Mag	Mag err
UVW2	56806.51	18.96	0.19
UVW2	56808.62	19.08	0.20
UVW2	56812.45	18.19	0.13
UVW2	56813.51	18.11	0.12
UVW2	56815.02	17.88	0.11
UVW2	56816.61	18.03	0.12
UVW2	56816.69	17.82	0.11
UVW2	56817.26	17.99	0.15
UVW2	56819.49	17.88	0.14
UVW2	56820.55	17.78	0.11

Schlafly & Finkbeiner (2011) cite a Galactic extinction of $A_{V\,Landolt} = 0.032$ mag in the direction of UGC8503.

3.1.1.1 Swift Ultraviolet Observations

We began a *Swift* UVOT photometric monitoring program on 2014 May 27 and determined that the target had become bright enough for spectroscopic observations to begin on 2014 June 05. We obtained UVOT photometry in the six photometric bandpasses from phases −18 days through +45 days relative to B-band maximum light and was analyzed using the reduction method of the *Swift* Optical/Ultraviolet Supernova Archive (SOUSA) (Brown et al., 2014a). We removed host galaxy light from the photometry in all six bandpasses using template images obtained one year after the initial observations. The reduced photometry is presented in Table 3.2.

Six epochs of spectra were observed between phases −9 through +18 days using both the UV and V grisms operating in clocked mode. The UVOT spectra snapshots were extracted, wavelength calibrated and flux calibrated using UVOTPY (Kuin, 2014; Kuin et al., 2015) and were then coadded for each epoch using variance

Table 3.3: Spectroscopy of iPTF14bdn.

Date (2014)	MJD +56000	SN Phase (days)	Integration Time (sec)	Telescope	Instrument
May 30	807.7	-14.8	1800	LiJiang 2.4m	LJT+YFOSC
Jun 01	809.6	-12.9	2100	LiJiang 2.4m	LJT+YFOSC
Jun 03	811.7	-10.8	1800	LiJiang 2.4m	LJT+YFOSC
Jun 05	813.5	-9.0	6497	*Swift*	UVOT V grism
Jun 08	816.6	-5.9	7270	*Swift*	UVOT UV grism
Jun 09	817.6	-4.9	1800	LiJiang 2.4m	LJT+YFOSC
Jun 11	819.5	-3.0	4590	*Swift*	UVOT UV grism
Jun 19	827.6	5.0	9140	*Swift*	UVOT UV grism
Jun 23	831.2	8.7	8617	*Swift*	UVOT UV grism
Jun 24	832.6	10.1	2100	LiJiang 2.4m	LJT+YFOSC
Jun 27	835.3	12.8	7840	*Swift*	UVOT V grism
Jul 02	840.3	17.8	5660	*Swift*	UVOT UV grism
Jul 05	843.6	21.0	2100	LiJiang 2.4m	LJT+YFOSC
Jul 24	862.6	40.0	2100	LiJiang 2.4m	LJT+YFOSC

weighting. Our extraction process for the UV grism images utilized galaxy template images observed on 2015 May 19 and June 4 to remove light from the host galaxy and other contaminant sources near the SN (Section 2.2.2.1) (Smitka et al., 2016). This resulted in the removal of a feature near 2500 Å in the -6 and -3 day spectra which we attribute to a faint zero order diffraction source in the grism images. Details of the spectroscopic observations are presented in Table 3.3. [2]

3.1.1.2 Optical Observations

We observed optical photometry and spectrophotometry with the Lijiang 2.4m telescope and the Yunnan Faint Object Spectrograph and Camera (YFOSC) (Wang et al., 2008). Photometric observations were made in the *UBVRI* bandpasses between the dates of 2014 May 29 and 2014 July 24. We performed background subtraction of the host galaxy light for all filters using template observations gathered on 2015 March 17. To estimate the residual brightness of iPTF14bdn in the template images we used the *UBVRI* photometry of SN 1991T (Lira et al., 1998), which extends $\sim$

[2]The *Swift* UVOT photometric transmission functions, grism profiles, and their associated calibration products are available at http://heasarc.gsfc.nasa.gov/docs/heasarc/caldb/data/swift/uvota/index.html

400 days past maximum in all bands. By assuming that iPTF14bdn behaved similarly to SN 1991T in all bands, we found that we should expect the B band to contain the brightest residual source in which the SN is ~ 22 mag (~ 0.001 of the maximum-light flux). The lack of extinction is suggestive that the SN exploded in a low-dust environment and that we should not expect light echoes to be present in the template images. Following template subtraction, we made photometric measurements using aperture photometry. Spectroscopic observations were made on the dates shown in Table 3.3 spanning phases of -15 through $+40$ days relative to B-band maximum light.

Additional photometric measurements in the *UBVRI* bandpasses were made using the 80 cm Tsinghua-NAOC (National Astronomical Observatories of China) Telescope (TNT) between the dates of 2014 June 18 and 2014 June 28. These data were reduced and processed using the same methods as the YFOSC data.

3.1.2 Light Curves

Light curves of iPTF14bdn are displayed in Figure 3.1. Visual inspection of the light curves shows very slow declining behavior and an I-band secondary peak about $+22$ days after B-band maximum. To calculate light curve parameters for the UVOT photometry, we used a version of the SNooPy light curve fitting algorithm (Burns et al., 2011) that had been modified by Chris Burns to accept the UVOT photometric bandpasses and calculate S-corrections (Suntzeff, 2000) onto the Carnegie Supernova Project photometric system for the u, B and V bandpasses (Hamuy et al., 2006; Contreras et al., 2010; Stritzinger et al., 2011). Using this we calculate B-band maximum light to occur at $MJD = 56822.5 \pm 0.3$ and $\Delta m_{15}(B) = 0.84 \pm 0.05$ mag. This slow declining behavior is characteristic of the 1991T-like and 1999aa-like classes of objects and does not provide adequate information for distinguishing between these

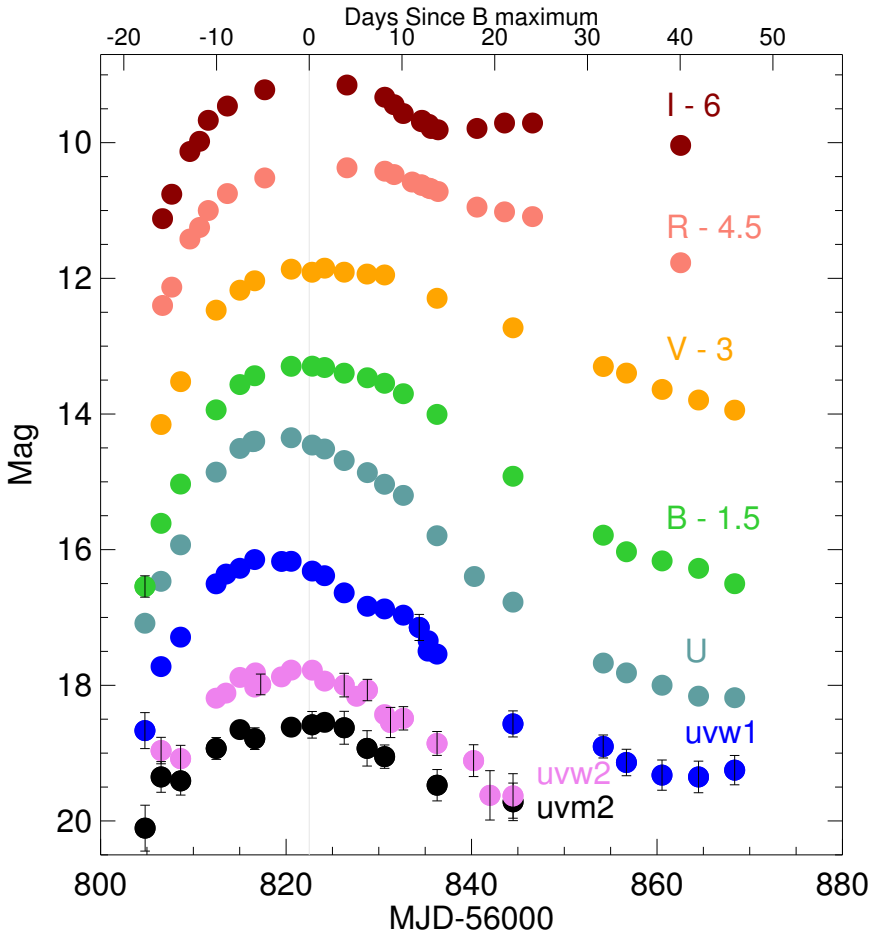

Figure 3.1: Lightcurves of iPTF14bdn.
Data shown here for the *UBV* filters are those of UVOT. Error bars are shown only for data points with photometric errors greater than 0.15 mag. The light grey vertical line marks B-band maximum. Host galaxy light has been removed from all photometry.

Table 3.4: Light curve parameters of iPTF14bdn.

Filter	Peak MJD	Peak Mag	Δm_{15} (mag)
UVM2	56819.6 ± 0.6	18.63 ± 0.04	0.59 ± 0.21
UVW2	56819.3 ± 0.3	17.84 ± 0.03	0.83 ± 0.11
UVW1	56818.4 ± 0.2	16.18 ± 0.02	1.02 ± 0.05
U	56819.0 ± 0.2	14.28 ± 0.02	1.27 ± 0.07
B	56822.5 ± 0.3	14.75 ± 0.02	0.84 ± 0.05
V	56823.2 ± 0.2	14.83 ± 0.01	0.60 ± 0.04
R	56825.7 ± 0.4	14.87 ± 0.02	0.61 ± 0.04
I	56822.7 ± 0.2	15.10 ± 0.02	0.67 ± 0.02

two categorizations. Light curve parameters for the ground-based Lijiang 2.4m and TNT photometry were calculated using smooth interpolating spline fits to the data. Our calculated light curve parameters are presented in Table 3.4

3.1.3 Photometric Colors

The color evolution of iPTF14bdn in (*uvm2* - *uvw1*) and (*uvw1* - *V*) are presented in Figure 3.2. In both colors, iPTF14bdn is bluer than normal at the earliest epochs. Its early time evolution is toward redder colors in contrast to normal SNe Ia at this epoch. Around +5 days prior to B-band maximum we observe iPTF14bdn to transition to normal SNe Ia evolution in both colors.

3.1.4 Spectra

The spectra of iPTF14bdn shown in Figure 3.3 represent the first published ultraviolet time-series spectra of a 1999aa-like SN Ia. Upon visual inspection we observe a weak Ca II H & K feature near 3800 Å at early times and its subsequent evolution towards normal SN Ia levels starting around maximum light. This characteristic was first observed by Filippenko et al. (1992a) in SN 1991T and later by Garavini et al. (2004) in SN 1999aa. We see a lack of strong Si II 6355 Å features prior to maximum

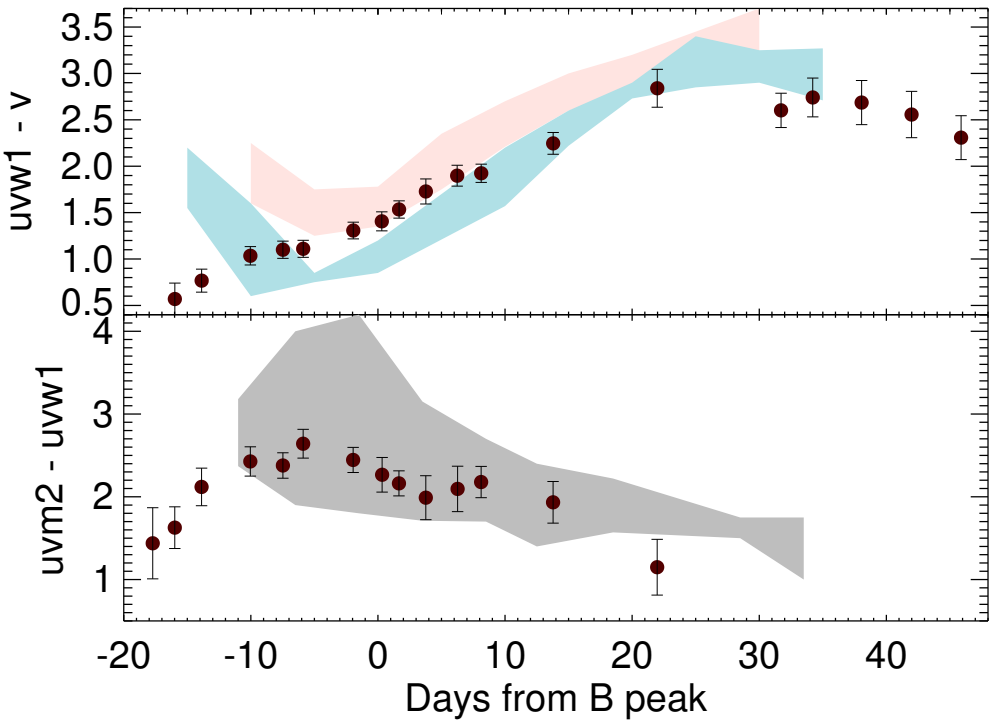

Figure 3.2: SN iPTF14bdn UV colors vs SN phase.
The color evolution of iPTF14bdn in the UVOT bandpasses. The red and blue shaded regions outline the range of colors observed for the evolution of NUV-red and NUV-blue normal SNe Ia respectively, as defined by Milne et al. (2013). The gray shaded region outlines the range of colors observed for normal SNe Ia found by Brown et al. (2014c). The early-time evolution is shown to contrast normal SN Ia in both colors and transition towards the normal evolution trend around -5 days relative to B-band maximum.

light and its subsequent development days after maximum light, also characteristic of 1991T-like and 1999aa-like objects (Filippenko et al., 1992a; Garavini et al., 2004).

3.1.5 Classification

To classify iPTF14bdn we compared the B-band photometric light curve parameters and -6 day spectrum to those of SNe Ia subclasses. We find that $\Delta m_{15}(B) = 0.84$ mag of iPTF14bdn is consistent with that of SN 1999aa with $\Delta m_{15}(B) = 0.85$ mag (Jha, 2002) and SN 1991T with $\Delta m_{15}(B) = 0.95$ mag (Lira et al., 1998). A spectral comparison of iPTF14bdn at -6 days to SNe 1999aa, 1991T and a normal SNe Ia (SN 2011fe) is shown in Figure 3.4. We conclude that in the optical iPTF14bdn is a clone of SN 1999aa at this epoch.

3.1.6 Comparison to SN 2011fe

Using abundance tomography modeling, Sasdelli et al. (2014) determined that the optical spectra of SN 1991T at early times displayed several highly ionized features not associated with normal SNe Ia, notably strong Fe III, Co III, Si III, and the lack of strong Si II and Ca II H & K features. In the week prior to maximum light the spectra develop more normal Si II features and then evolve to be indistinguishable from normal SNe Ia by one week after maximum light. Garavini et al. (2004) cites similar findings for SN 1999aa and notes that the resemblance to normal spectra is seen to occur at slightly earlier epochs than SN 1991T.

In the ultraviolet we observe an overall similar trend from deviancy toward normalcy upon comparison to SN 2011fe in Figure 3.5 (Mazzali et al., 2014). The Ca II H & K feature near 3800 Å is initially very weak at more than a week prior to maximum light and grows progressively more normal with time, becoming indistinguishable between +5 and +9 days. This is indicative of a highly energized atmosphere prior to maximum light.

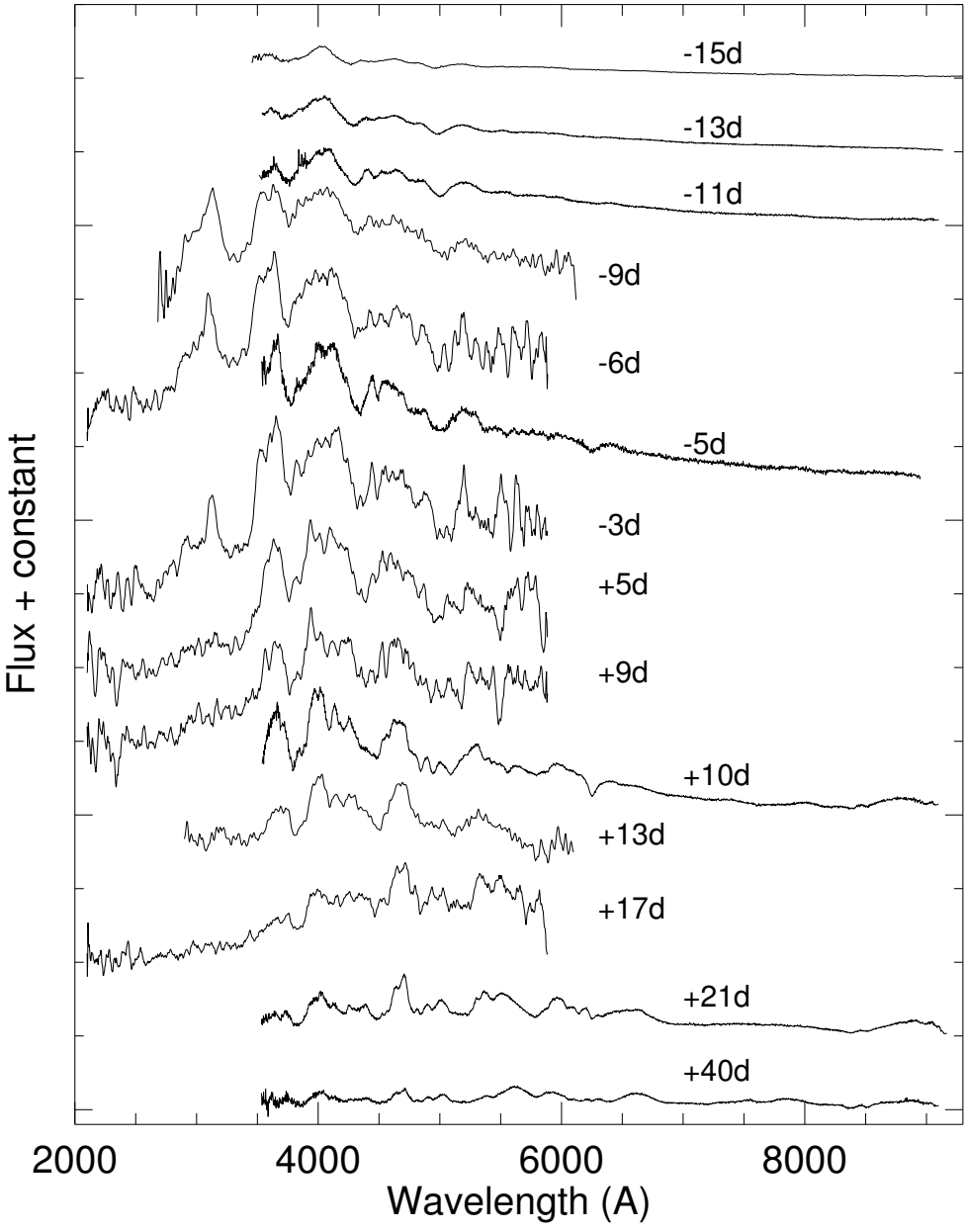

Figure 3.3: Spectral series of iPTF14bdn.
Phases are calculated relative to B-band maximum light at $MJD = 56822.5 \pm 0.3$.

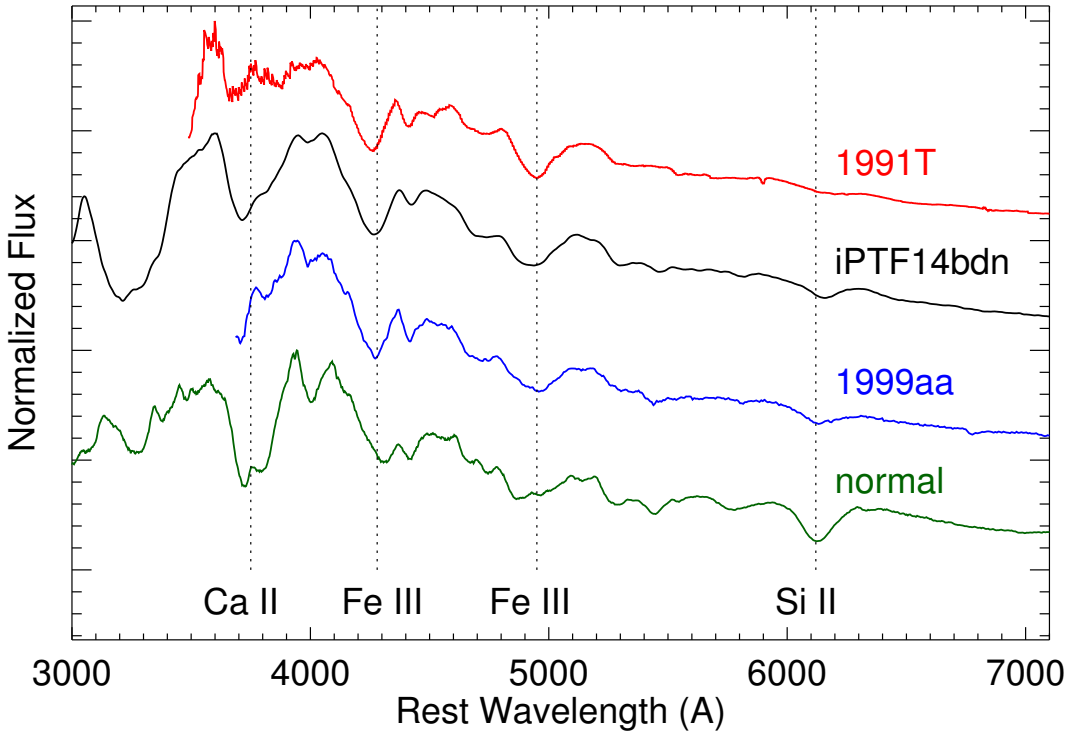

Figure 3.4: Spectroscopic classification of iPTF14bdn.
We spectroscopically classify iPTF14bdn at −6 days by comparison to the spectra shown. The features of weak Si II, strong Fe III and the detection of Ca II are most consistent with SN 1999aa. The normal SN Ia shown is SN 2011fe. All comparison spectra are from epochs within 1 day of our spectrum. (Mazzali et al., 1995; Garavini et al., 2004; Mazzali et al., 2014).

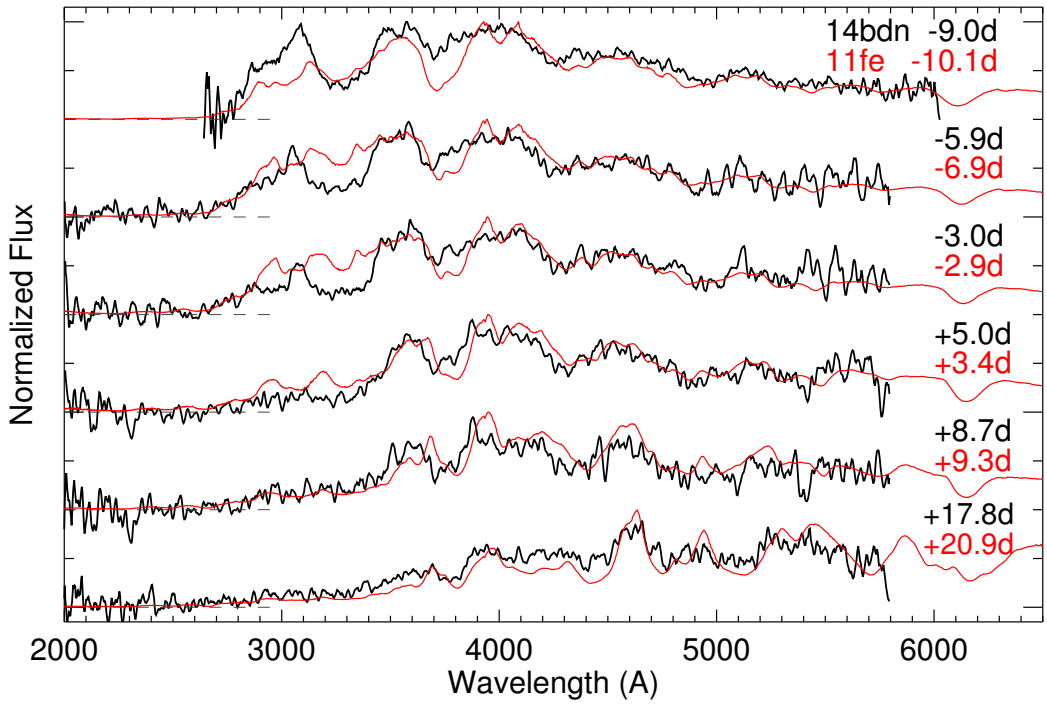

Figure 3.5: Spectral series of iPTF14bdn and SN 2011fe.
Comparison of the rest-frame spectra of iPTF14bdn to the normal SN 2011fe.

In the $2800 - 3200$ Å range we see much less UV absorption than is normal at -9 days relative to maximum light. This bright feature is shown to evolve to normal flux levels by -6 days relative to maximum light. Leading up to maximum light we see a significant deficiency of flux in the $3000 - 3500$ Å range. The models of SN 1991T of Sasdelli et al. (2014) suggest that this strong absorption feature is attributable to a combination of Fe III, Co II, and Co III indicating a highly energized atmosphere. By +5 days relative to maximum light we observe the evolution blueward of 3500 Å to be largely indistinguishable from SN 2011fe.

We observe no major differences between SN 2011fe and iPTF14bdn blueward of 2800 Å. In this region both SNe appear to evolve similarly, indicating that line blanketing is playing a major role in suppressing flux.

3.1.7 Comparison to SN 2012fr

Based on a thorough analysis of the optical spectra of SN 2012fr, Childress et al. (2013) concluded that 2012fr was not a 1991T-like or 1999aa-like SN with high velocity features superimposed, but was rather best classified as a very luminous, slow declining normal SN with $\Delta m_{15}(B) = 0.80$ mag. This conclusion was based on the strong presence and high velocity of a Si II 6355 Å feature and a lack of strong Fe signatures characteristic of 1991T-like SNe. In a separate analysis, Zhang et al. (2014) presented *Swift* UVOT and optical photometry and optical spectra of SN 2012fr. Their analysis found $\Delta m_{15}(B) = 0.85$ mag and concluded that SN 2012fr is likely a member of a subset of 1991T-like SNe Ia whose differences can be the result of viewing angle and asymmetric ejecta.

In Figure 3.6 we present a comparison of UVOT UV-grism spectra of SN 2012fr and iPTF14bdn. We extracted and coadded the spectra of SN 2012fr using the same methods as iPTF14bdn. No galaxy template images were used in the extraction of

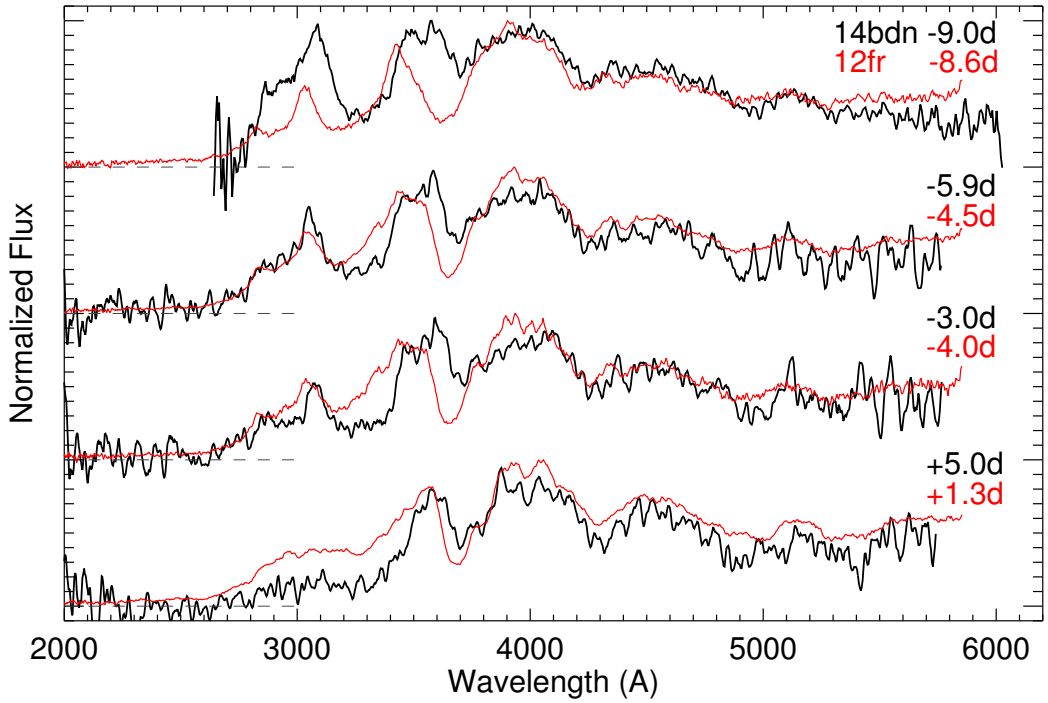

Figure 3.6: Spectral series of iPTF14bdn and SN 2012fr.
Comparison of the rest-frame spectra of iPTF14bdn to UVOT UV-grism spectra of the luminous, slow declining, normal SN 2012fr.

these spectra because no signs of contamination are present. A composite maximum light UVOT spectrum of this SN was first presented by Brown et al. (2014b), and the full UVOT spectral series is presented here for the first time.

Redward of 4000 Å we note that the spectra appear very similar at all epochs for which we make comparisions. We see weaker Ca II H & K absorption in iPTF14bdn than is present in SN 2012fr, as Childress et al. (2013) reported for 1991T-like SNe.

As with SN 2011fe, we see less absorption between $2800 - 3200$ Å in iPTF14bdn around 9 days prior to maximum light. We note that the shapes of the features in this region are more similar here than was the case with SN 2011fe. Continuing to maximum light we also again observe a deficiency of flux in the $3000 - 3500$ Å

range in iPTF14bdn, where we now note that the overall shape of these absorption features are more similar than was the case with SN 2011fe. We notice no significant differences blueward of 2800 Å.

3.1.8 SYNAPPS Models of iPTF14bdn

The synthetic spectra synthesis program SYN++ (Thomas et al., 2011) is derived from SYNOW (Fisher et al., 1997). It computes synthetic spectra of SNe Ia in the photospheric phase by modeling the radiative transfer of photons emitted by a sharp photosphere below an expanding ejecta atmosphere. Spectra lines are assumed to form by resonance scattering using the Sobolev approximation of a moving atmosphere (Sobolev, 1960; Jeffery, 1989). The SYNAPPS code automates a χ^2 minimization routine which identifies the combination of SYN++ model atmosphere parameters that provide the best matching synthetic spectrum to an observed spectrum. The SYN++ and SYNAPPS fitting parameters include the photospheric temperature and velocity, and individual ion temperatures, velocities, ionization states, and optical depths. The program does not distinguish between stable and radioactive atomic species and does not simulate isotopic line shifts. We chose to focus only on line identifications made by the SYN++ and SYNAPPS programs in our observed spectra. It is noteworthy that SYNAPPS is not an ab initio SNe Ia modeling code and so does not offer as much insight into the SN progenitor system and explosion mechanism as other methods (Woosley & Kasen, 2011). Thus, we encourage additional analysis of the data we present here using other modeling techniques.

To investigate the atomic structure of the SN ejecta we performed SYNAPPS model fits to the spectra near -10 and $+10$ days relative to B-band maximum light. Timely computation of the model fits required the use of a high performace computer cluster. For this purpose the UVOT and optical spectra at the epochs nearest these

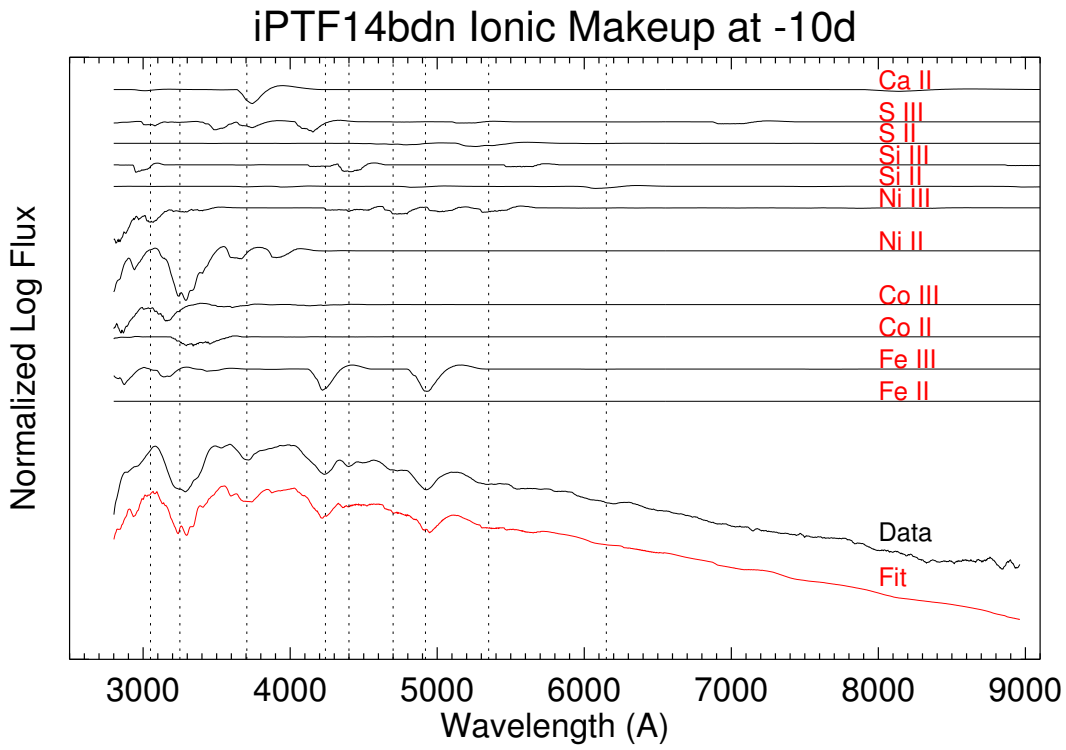

Figure 3.7: SYNAPPS fits of iPTF14bdn at -10 days.
SYNAPPS fit of combined UV and optical spectra of iPTF14bdn at -10 days relative to B-band maximum. The observed spectrum is labeled as 'Data' and plotted in black. The best SYNAPPS fit is labeled as 'Fit' and plotted in red. Individual ion absorption features of the SYNAPPS fit were calculated using SYN++ and are shown above the data.

phases were smoothed, normalized, and stitched together. The model parameters assumed that all ions were attached to the photosphere and equal weight was placed on all wavelengths of the spectra. Individual ionic contributions were generated using SYN++ and the best fit parameters computed by SYNAPPS. The resulting model fits with the ion line strengths are presented in Figures 3.7 & 3.8. The model fits included all ions shown and additional contributions from Mg II, Na I and O I, which are not shown.

In the model fit of the -10 day spectrum we find evidence that singly and doubly

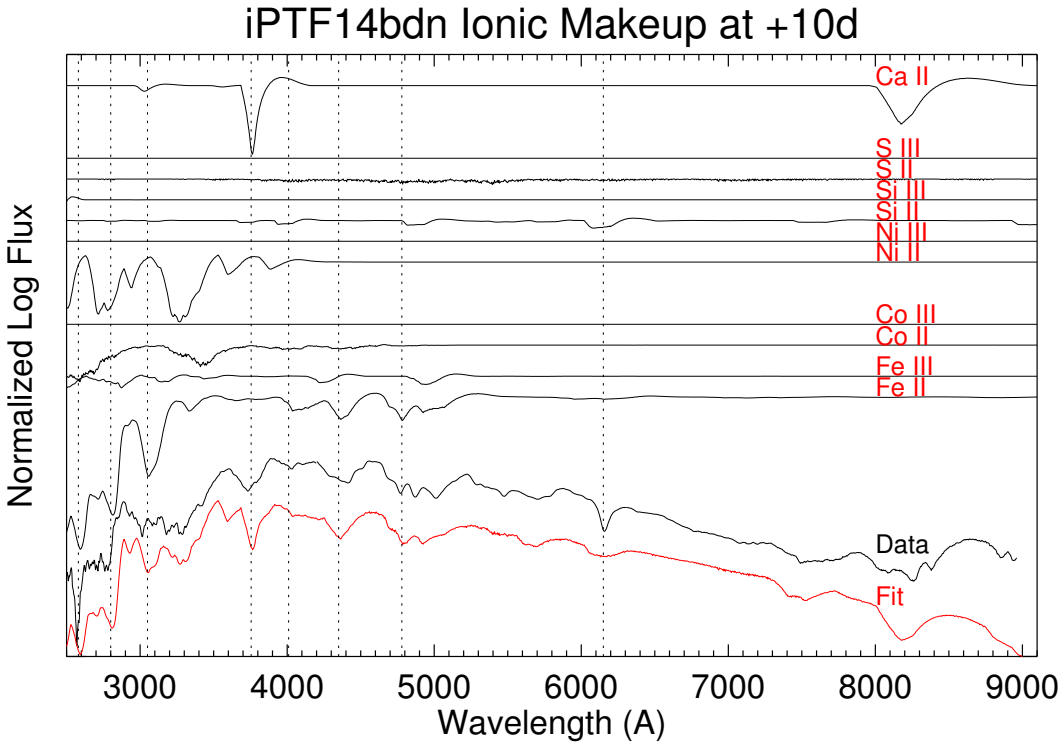

Figure 3.8: SYNAPPS fits of iPTF14bdn at +10 days.
SYNAPPS fit of combined UV and optical spectra of iPTF14bdn at +10 days relative to B-band maximum. The observed spectrum is labeled as 'Data' and plotted in black. SYNAPPS fit is labeled as 'Fit' and is plotted in red. Individual ion absorption features of the SYNAPPS fit were calculated using SYN++ and are shown above the data.

ionized iron group elements dominate the line forming regions. The two strongest features in the optical near 4250 Å and 4910 Å are attributed to Fe III absorption. Ni III is also identified in the optical by shallow features near 4700 Å and 5350 Å. Both of these ions also display significant absorption blueward of 3500 Å. Co III is shown to have little to no absorption redward of 4000 Å while contributing significantly blueward of 3300 Å. Fe II and Co II are shown to produce less absorption than their doubly ionized counterparts while Ni II dominates blueward of 4000 Å. Si III and S III are shown to be more prominent than their singly ionized counterparts. Very weak Si II absorption is observed near 6100 Å. A Ca II H & K absorption feature was required by the model to fit the observed absorption feature near 3700 Å. This Ca II feature is weaker than that of a normal SN Ia at this early epoch and when present with strong doubly ionized iron group elements is considered to be the hallmark of a 1999aa-like SN Ia as opposed to a 1991T-like SN Ia (Garavini et al., 2004).

At +10 days our model shows the iron group elements to be predominantly in the first ionization state. While Fe III still shows weak absorption features, Fe II now dominates in both the optical and UV. We find that absorption blueward of 3000 Å is predominantly the result of Fe II with Ni II contributing to a lesser degree. Our model now finds no evidence of Co III and Ni III and instead find significant absorption from Co II and Ni II. The transition from doubly ionized iron group elements to singly ionized states is shown to now suppress the early-time feature near 3000 Å. In particular, the strong Fe II absorption feature that has developed at this wavelength suggests that it is the ion primarily responsible for the evolution of this feature. Si II is now prominent and comparable in strength to normal SNe Ia with no Si III features evident. Ca II is now prominent near 3700 Å and 8200 Å and comparable in strength to SN 2011fe.

In Figure 3.9 we show the −10 and +10 day best-fit model spectra divided by the

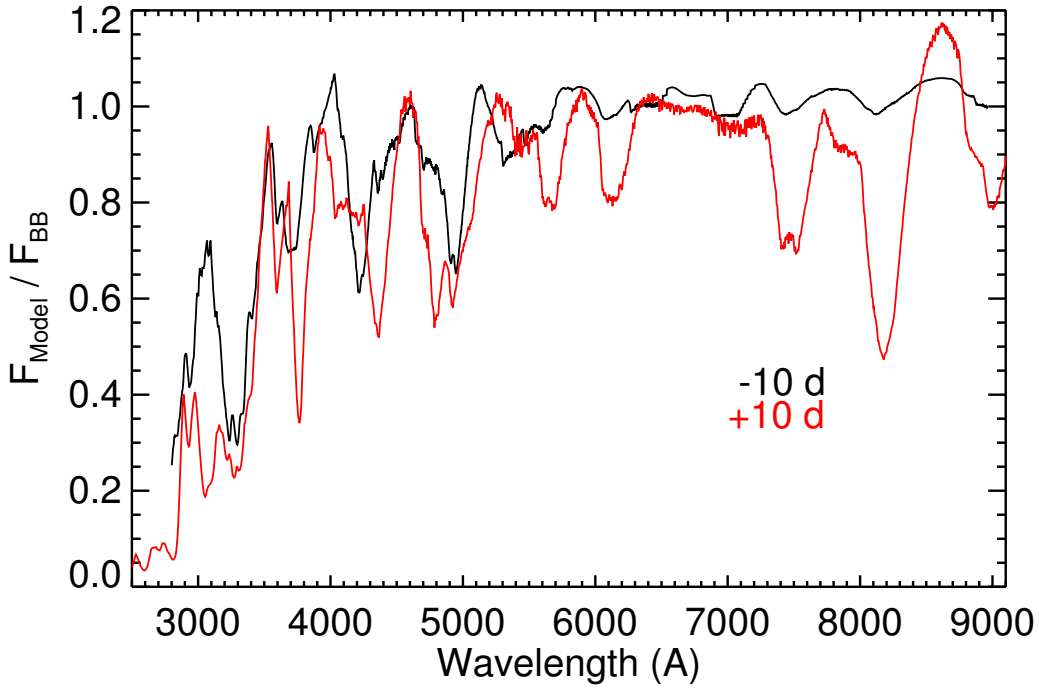

Figure 3.9: SYNAPPS model opacities of iPTF14bdn.
The best-fit SYNAPPS model spectra of the data at -10 and $+10$ days divided by the corresponding best-fit models' underlying blackbody emission. The -10 day data shows significant transmission of the blackbody flux between $2800 - 3200$ Å, suggesting a low opacity at this epoch within this wavelength range. We attribute this opacity window to iron group ions at higher than normal temperatures above the photosphere based on the ion analysis in Figures 3.7 & 3.8. This transmission decreases in the $+10$ day model.

best-fit blackbody emission profiles as calculated by SYNAPPS and SYN++. The best-fit model photospheric temperatures were $9,200$ and $8,800$ K for the -10 and $+10$ day spectra respectively. This provides insight into the total effective opacity of the line forming region in the model as a function of wavelength and is useful for comparison to other models (Hoeflich et al., 1993). In the -10 day model near 3000 Å we see evidence for significant transmission of the underlying blackbody flux. The proportion of transmitted flux is greatly reduced in the $+10$ day model.

3.1.9 Comparison to 1999aa and 1991T-like SNe Ia

In Figure 3.10 we compare the rest-frame of iPTF14bdn at -6 days relative to B-band maximum light to comparable epoch spectra of 1991T (Mazzali et al., 1995), two high-z 91T-like SNe Ia from the ESSENCE Project (Miknaitis et al., 2007; Foley et al., 2009) and SN 1999aa (Garavini et al., 2004). We observe iPTF14bdn to closely resemble SN 1999aa at this epoch. Within the regions of spectral overlap we find an overall good agreement among the spectra with the exception of the range $3500 - 4000$ Å, where we observe heterogeniety. Sasdelli et al. (2014) performed abundance tomography modeling of the spectra of SN 1991T within this wavelength range and determined that the ions which made the strongest contributions to SN 1991T at this epoch were Co III, S III or Si III with minimal contribution from Ca II H & K. Garavini et al. (2004) defines the presence of a Ca H & K absorption feature in this region to be the primary distinctive characteristic between 1999aa-like and 1991T-like SNe Ia. Among all of these SNe the strengths of this absorption feature is much weaker than that of a normal SNe Ia.

Among the SNe plotted we observe a continuum of absorption strengths within this wavelength range. We computed SYNAPPS fits of the iPTF14bdn, SN 1991T and the ESSENCE SNe spectra using the same ions as our previous analysis and

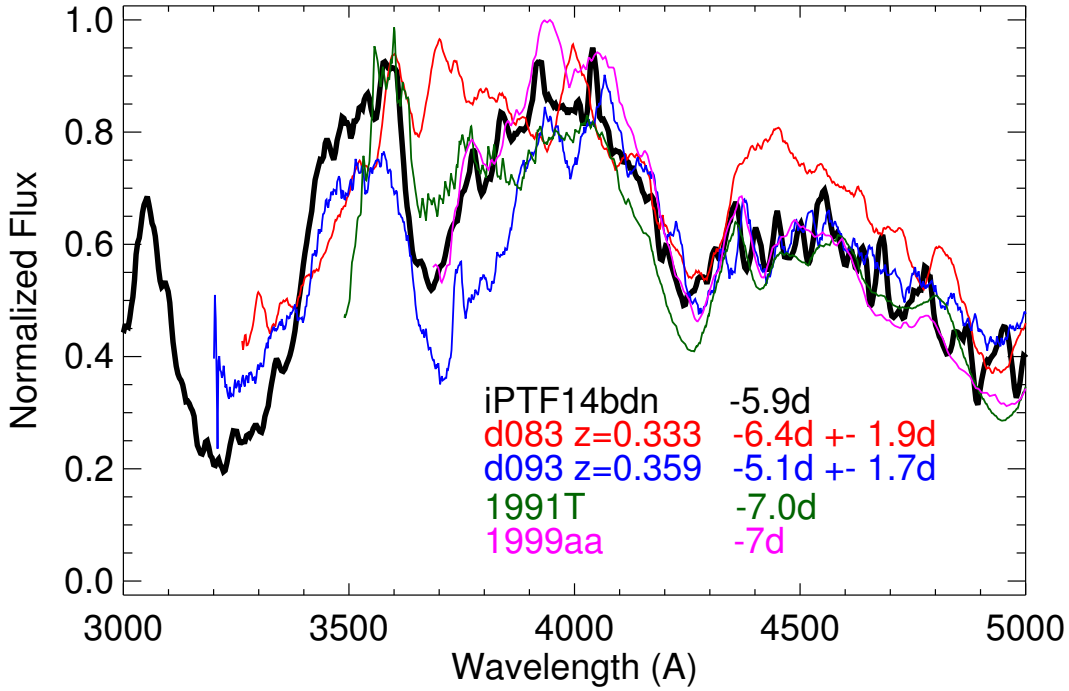

Figure 3.10: Rest-frame UV spectra of 1991T and 1999aa-like SNe Ia. Comparison of the rest-frame UV spectra of iPTF14bdn, SN 1991T, the ESSENCE sample of 1991T-like SNe and SN 1999aa around -6 days relative to B-band maximum light. We observe a heterogeniety in ion features within the wavelength range of $3500 - 4000$ Å, likely due to the variable contribution of Ca II H & K. The presence or lack of a Ca II H & K feature in this range is used as the classification criteria for 1999aa-like or 1991T-like SN. We observe that iPTF14bdn is most similar to SN 1999aa. The distribution of absorption strengths in this region suggests that these two subclasses of SNe Ia are not distinct events, but rather form a continuum.

found that the varying strength of the absorption feature in this range corresponds to a varying contribution of Ca II H & K. The SYNAPPS fits and the relative strengths of the Ca II absorptions are shown in Figure 3.11. This can be indicative that 1991T-like and 1999aa-like events are part of a continuous distribution of physical parameters.

It is noteworthy that of the five SNe we analyzed d093 of the ESSENCE project displays the strongest absorption feature in this wavelength range. The classifications of Foley et al. (2009) grouped 1991T-like and 1999aa-like SNe Ia into a single category due to their spectroscopic similarities. The absorption feature between $3500-4000$ Å and its attribution to Ca II presented here suggest that this SN is most appropriately classified as a 1999aa-like event.

3.1.10 Origin of Early-time UV Flux

The analysis of SNe Ia absolute magnitudes in the UVOT bandpasses of Brown et al. (2010) included two 1991T-like SNe Ia: 2007S and 2007cq, and no 1999aa-like SNe. In this work it was shown in the *uvm2* ($\lambda_{eff\_SNe\_Ia} = 2360$ Å) filter the absolute peak magnitude of 2007cq was ~ 2 mag brighter than normal SNe Ia. The data of 2007S (Milne et al., 2010) shows *uvw1* peaking 2.4 days earlier than the B-band maximum.

UVOT photometry has previously been presented for the 1991T-like SNe 2007S, 2007cq and 2011dn (Brown et al., 2010; Milne et al., 2010, 2013; Brown et al., 2014c). UV colors are observed for 2007cq at ~ -7 days to $+21$ days and 2011dn for ~ -5 days to $\sim +12$ days. Milne et al. (2010) found SN 2007S to have a high reddening value of $E(B-V) = 0.53$ and did not present data in the *uvm2* band, and thus we opt to not use this SN as a comparison object in this case. In the $(uvw1 - v)$ color the three SNe trace the evolution of normal SNe Ia at epochs later than ~ 5 days.

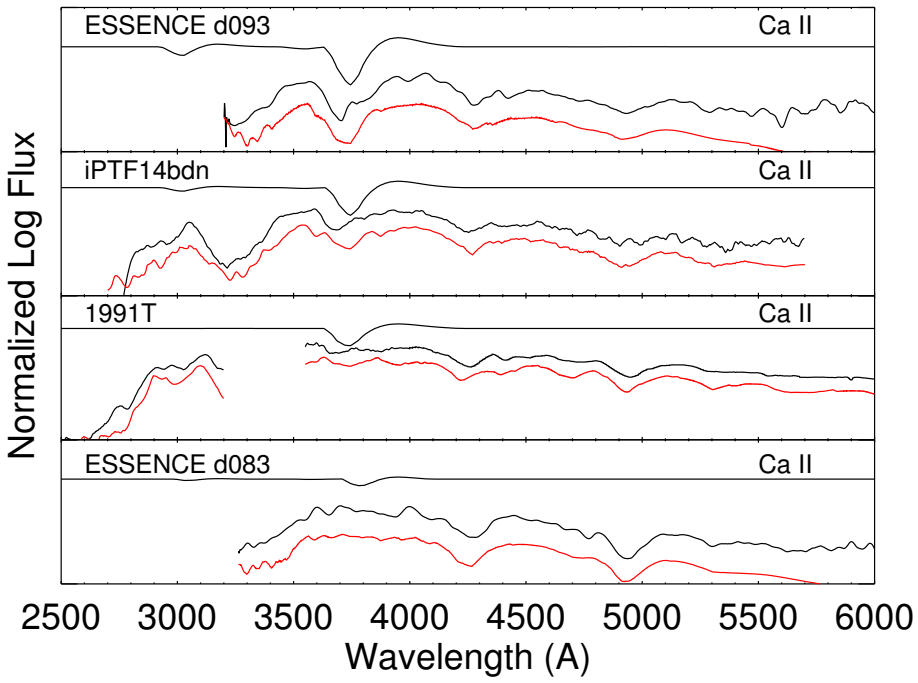

Figure 3.11: SYNAPPS models of Ca II.
SYNAPPS model fits to iPTF14bdn, SN 1991T, and ESSENCE SNe d083 and d093 are presented in red. The SN 1991T spectrum is composed of *IUE* and ground based data. The SYN++ model absorption profiles of the Ca II ion from the best SYNAPPS fits are plotted above each spectrum. Ca II is found to be present in all spectra, even when not detectable by visual analysis. The strength of the Ca II absorption is shown to be proportional to the depth of the $3500 - 4000$ Å absorption feature.

In ($uvm2 - uvw1$) iPTF14bdn and SN 2011dn show normal evolution later than ~ 5 days while SN 2007cq is ~ 1 mag bluer. For both colors it is only in the case of iPTF14bdn that the earliest epoch photometric observations exist and show bluer than normal colors and color evolution towards redder values, contrasting normal evolution.

The photometric evidence for increased UV flux at early phases is in agreement with our observation of the $2800 - 3200$ Å feature in the earliest UV spectra of iPTF14bdn. It is likely that this feature is the source of the greater than normal *uvw1* luminosity of the 1991T-like SN measured by Brown et al. (2010) and in the photometry presented here for a 1999aa-like SN. This feature is also likely to contribute to the observed high luminosity in the *uvm2* band, which is moderately sensitive to this wavelength regime. Our SYNAPPS analysis of this epoch's spectra suggests that the origin of this greater than normal luminosity is largely due to the presence of doubly ionized iron group elements which provide a low opacity window at these early epochs. For 1999aa-like SNe we conclude that the UVOT photometric filters appear able to trace the effect of temperature evolution of the iron group elements, most notably the progression of Fe III cooling to Fe II. Due to their spectroscopic similarities, we also expect this to be true for 1991T-like SNe Ia as well.

3.1.11 Progenitor System

In Section 3.1.8 we presented evidence of Fe III, Co II, Co III, Ni II and Ni III in the -10 day UV-optical spectrum of iPTF14bdn. By $+10$ days we see an evolution towards Fe II, Fe III, Co II and Ni II. If we assume a model of expanding ejecta shells above a radiating photosphere these results suggest a continuous distribution of iron group elements in the ejecta. In this scenario, the higher than normal temperatures at early times can be explained by the radioactive decay of greater than normal Ni

ion abundances in the outer layers. The possible physical origin of this behavior can be an explosion mechanism that produces significant mixing of newly synthesized iron group elements into the outer layers.

3.1.12 Origin of the I-band Secondary Maximum

Secondary maxima in infrared light curves are often observed in SNe Ia. Models of the physical origins of these features have suggested that the effect is dependent upon the mass and distribution of ^{56}Ni in the ejecta, and upon the recombination of doubly ionized iron group ions (Hoeflich et al., 1995; Kasen, 2006). The analysis of Jack et al. (2015) identified the secondary maximum in the *I*-band to be the result of Fe II emission from high excitation transitions following recombination of doubly ionized elements to singly ionized states. Their conclusion was that the *I*-band captures a transient Fe II emission feature at ~ 7500 Å which temporarily increases the in-band flux. Evidence supporting this conclusion was presented using optical spectra of the normal SNe 2014J and 2011fe just before and during the secondary maximum and PHOENIX models at similar epochs. They made no investigation of the presence of this feature in peculiar SNe Ia.

The photometry of iPTF14bdn in Figure 3.1 displays a secondary maximum in the *I*-band occurring around +20 days after B-band maximum light. Our identification in Sec. 3.1.8 of Fe III recombining to Fe II between −10 and +10 days, the persistent presence of Fe III at +10 days, and the well documented similarities of normal, 1991T-like and 1999aa-like SNe at these epochs suggest that the secondary maximum may be caused by the same feature as Jack et al. (2015). Our spectroscopic sample enables us to investigate the occurrence of this phenomenon in our data set by making a comparison of the optical spectral features just prior to and during the *I*-band secondary maximum. In Figure 3.12 we compare the optical spectra of June 24 and

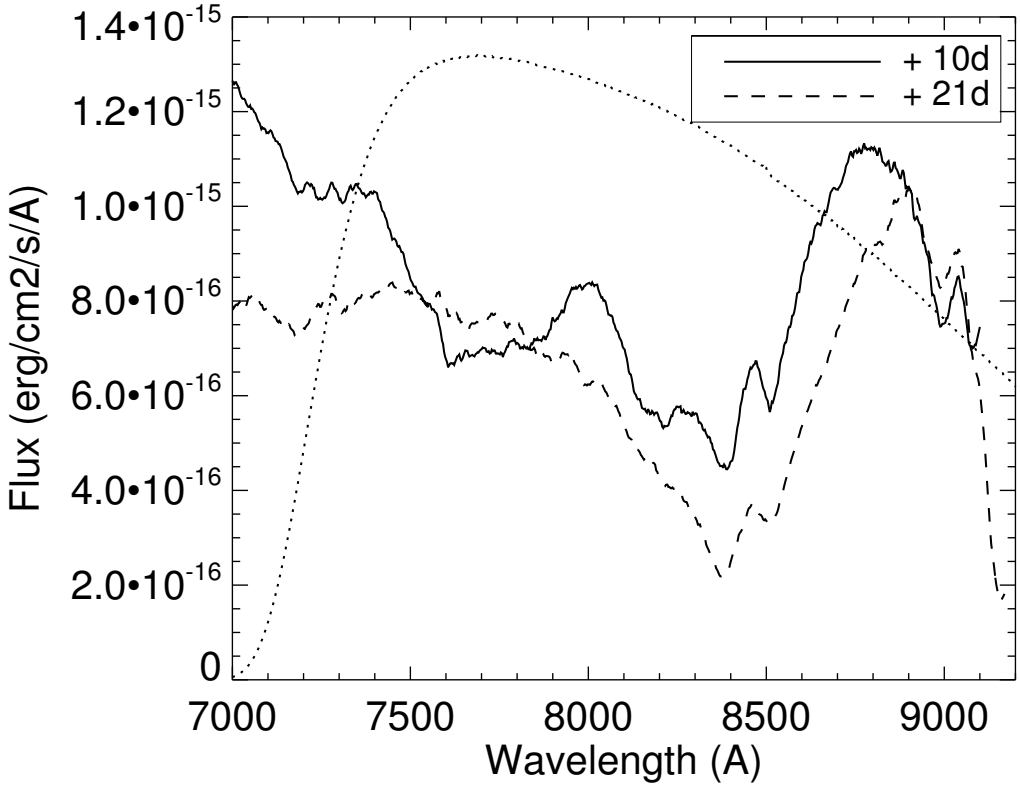

Figure 3.12: SN iPTF14bdn near *I*-band secondary maximum.
Spectra of iPTF14bdn at phases prior to and during the *I*-band secondary maximum. The dotted curve represents the normalized YFOSC *I*-band filter transmission function. We see evidence of an increase in flux at the epoch of *I*-band secondary maximum near ~ 7500 Å. In the normal SNe Ia 2014J and 2011fe this feature was attributed to recombination of Fe III to Fe II and was identified as the source of the *I*-band secondary maximum by Jack et al. (2015).

July 5, at phases +10 and +21 days respectively, in the region of the Lijiang 2.4 m's YFOSC *I*-band sensitivity. The combined transmission efficiency of the YFOSC *I*-band filter and CCD quantum efficiency is shown as a dotted line to highlight the spectral region to which our photometric observations are most sensitive. We show that the photometric system used is most sensitive to ~ 7700 Å, and is thus well suited for detecting the 7500 Å Fe II emission noted by Jack et al. (2015).

In iPTF14bdn we observe a similar increase in flux around ~ 7500 Å as Jack et al. (2015) at the epoch of *I*-band secondary maximum. This confirms that the same physical processes of the normal SNe 2014J and 2011fe are likely at work in this 1999aa-like SN. We conclude that the source of the *I*-band secondary maximum in iPTF14bdn is likely attributable to the same Fe II emission as in normal SNe.

We note that here the comparison spectra come from epochs of roughly equal *I*-band magnitude, the earlier epoch being about 5 days prior to the *I*-band trough minimum. This is in slight contrast to those of Jack et al. (2015), whose pre-secondary maximum spectra are timed closer to the trough minimum and lower fluxes. Thus, we expect our flux differences to be less stark, as is the case.

3.1.13 Identification of Peculiar SNe Ia

Our analysis of iPTF14bdn ties physical origins and spectroscopic features to an easily observable photometric characteristic: the early-time UV color. If future early-time, UV observations of 1999aa-like and 1991T-like SNe Ia display the same spectroscopic and color trends, then it may be possible to use rest-frame UV photometry alone to identify peculiar SNe Ia. This would prove very useful for identifying peculiar SNe Ia in data from large, photometry-only surveys, like LSST and DES, which will observe the rest-frame UV for high-z SNe.

3.2 NUV-Red and NUV-Blue SNe Ia

The photometric analysis of Milne et al. (2013) established an observational dichotomy in SN Ia NUV colors: NUV-red and NUV-blue. This analysis utilized *Swift* UVOT photometry of 23 SNe Ia between the epochs -10 to $+20$ days. They attributed the difference between the classes to a fundamental spectral difference in the $2900 - 3500$Å range possibly caused by differing abundances of synthesized Iron group elements in the outer layers of the ejecta. Their interpretation was that NUV-blue SNe allow more UV radiation to escape because they have less synthesized Iron group ions in the atmosphere above the photosphere, whose absorption lines strongly blanket the UV portion of the spectrum. This interpretation contrasts that of the 1999aa-like iPTF14bdn, which is also UV-bright, but whose pre-maximum light optical spectra clearly show Fe III near ~ 4200Å and ~ 4900Å, and thus require an interpretation in which Iron group ions be present above the photosphere. The presence of Carbon seen in all NUV-blue SN ejecta, and lack thereof in NUV-red SNe Ia, was interpreted as evidence that the fusion burning front reaches farther out in NUV-red SNe than in NUV-blue SNe. This analysis included the HST ACS spectra of Wang et al. (2012) for SN 2004dt (NUV-blue) and 2005cf (NUV-red). A clear UV excess was shown between $2700 - 3500$Å at -2 days, though the low resolution of these spectra (~ 50 Å/pix near 3000Å, Larsen et al., 2006) prevented in depth analysis of the root cause (Figure 9 of Wang et al. (2012), Figure 15 of Milne et al. (2013)). These spectroscopic differences were seen to diminish with time and be absent by $+5$ days.

The additional analysis of Milne et al. (2015) found that some of the color difference between NUV-blue and NUV-red SNe Ia could be explained by the observation that NUV-red SNe are demonstrated to have near-maximum Si II and Ca II H&K

ejecta velocities on average 12% greater than NUV-blue SNe. Their interpretation was that the high velocity lines are believed to produce broader features, which contribute to a greater opacity in the UV and blue regions where line blanketing is significant. Using rest-frame UV spectra spanning with wavelengths as short as ~ 3000Å of SNe within $0.11 \leq z \leq 0.37$ (Foley et al., 2012c), Milne et al. (2015) showed that SN spectroscopic pairs (i.e. SNe with similar lightcurve widths at similar epochs) exhibit a behavior in agreement with this scenario. Figure 5 of Milne et al. (2015) shows that these NUV-blue and NUV-red spectroscopic pairs exhibit similar UV features with differing UV continua while having few differences redward of 4500Å. Low signal-to-noise in the UV portions of the spectra hindered a more thorough analysis. Milne et al. (2015) stated that UV opacity differences resulting from ejecta velocity characteristics can account for some, but not the entirety, of the observed color differences, and that additional causes are likely at work.

An alternative explanation for the UV and optical differences between NUV-red and NUV-blue SNe is atmospheric metallicity and its effect on UV emission in the outer atmospheres (Mazzali, 2000). In this process, optical photons in the low density outer layers of ejecta are absorbed by the strongest Mg II, S II, Si II metal lines (with some contribution from Cr II and other Fe group ions) and emitted primarily as UV flux between $2800 - 3300$Å. This reverse fluorescence emission was modeled to have characteristic peak features near 2900 and 3100Å, and exhibits a trend in which lower metal content provides greater UV flux (Walker et al., 2012). This model is pictured in Figure 3.13. The Walker et al. (2012) model was trained to match the near-maximum-light (-0.9 days) UV and optical spectra of SN 2005cf, a SN Ia with $\Delta m_{15}(B) = 1.1$ renowned for its normal behavior (Wang et al., 2009). The best-fit model was then tweaked to investigate greater and lesser luminosities and atmospheric metallicities. The model's η parameter is the multiplicative factor used

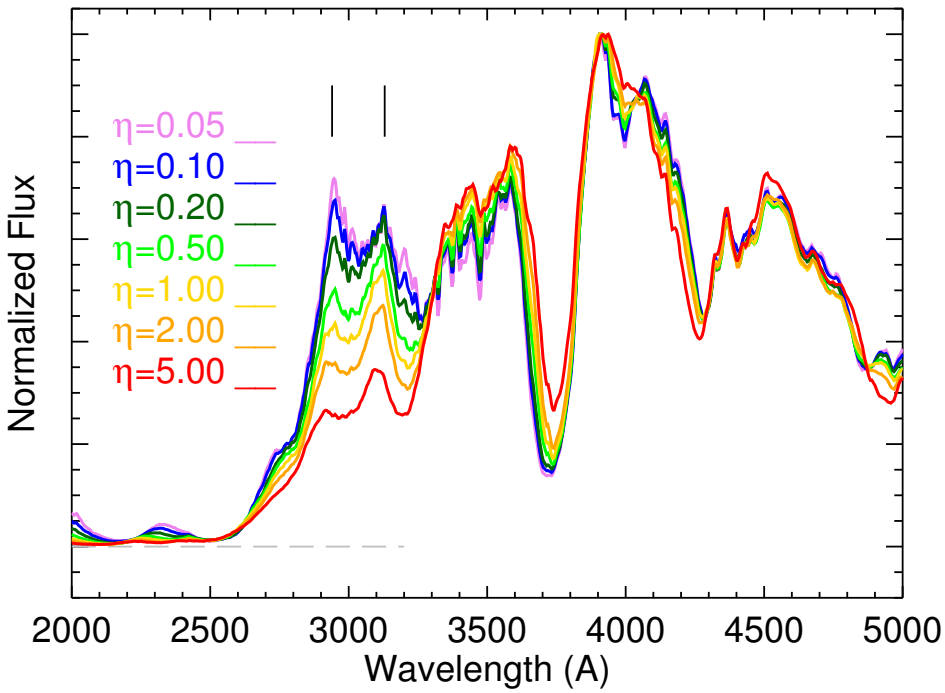

Figure 3.13: SNe Ia metallicity models
Synthetic SNe Ia spectra for $log(L_{bol}/L_{\odot}) = 9.6$ modeled by Walker et al. (2012). The η parameter is a multipicative metallicity scaling factor for elements with atomic number $Z > 20$. The vertical lines demark NUV double peak features whose strengths are shown to vary as a function of model atmospheric metallicity.

to vary the model metallicity in the ejecta shell for elements with atomic number $Z > 20$. The effects of varying η on the model UV spectra for a SN with $log(L_{bol}/L_{\odot}) = 9.6$ is demonstrated in Figure 3.13.

The limitations of UV spectroscopic resolution for Wang et al. (2012); Milne et al. (2013) and the spectroscopic cutoff at ~ 3000Å of Milne et al. (2015) lead us to continue the investigation of NUV-blue and NUV-red spectroscopic differences using our *Swift* UVOT sample. This is enticing because our spectroscopic data has spectral coverage deeper into the UV and better resolution than the *HST* ACS

spectra. The SNe with NUV-red photometric classifications for which we have UV spectra are: SNe 2005cf, 2005df, 2007sr, and 2009an. The SNe with NUV-blue photometric classifications for which we have UV spectra are: SNe 2011by, and 2011fe. This sample contains only SNe Ia at redshifts $z < 0.01$, and consists of SNe with decline rates $1.0 < \Delta m_{15}(B) < 1.2$ mag, with the exception of SN 2009an with $\Delta m_{15}(B) = 1.5$. With this single exception for SN 2009an, we used the same comparison criteria as Milne et al. (2015) of using SNe with similar lightcurve shapes, at similar phases. Adopting these criteria make it less likely that any differences in the spectra are attributable to luminosity or phase variations (Brown et al., 2010), and are more likely due to an intrinsic UV variability among optically-similar SNe. The timing of the observations in our sample relative to B-band maximum light allow us to compare spectra observed at phases within ~ 1 day of each other for phases between -7 to $+20$ days. We show these comparisons in Figures 3.14 and 3.15. The spectra shown in these figures are all in the rest-frame, have no applied extinction corrections, and have been multiplicatively flux-scaled such that match in flux is achieved between $4000 - 5000$Å.

We show in Figures 3.14 and 3.15 that the NUV-blue SNe have greater flux within the wavelength range $2700 - 3500$Å at epochs prior to $\sim +10$ days. At wavelengths shorter than 2600Å, the spectra continua converge within the limits of our flux uncertainties. The difference between the classes is most significant at the earliest epochs and decreases with time. The differences between spectral sets within the wavelength range $2700 - 3500$Å appear to be twofold: 1) the continua fluxes are higher in NUV-blue SNe, and 2) NUV-blue SNe show double peak features near 2900Å and 3100Å, which are not present or are significantly weaker in the NUV-red sample. We made no attempts to meaure individual ion structures or velocities as did Milne et al. (2015).

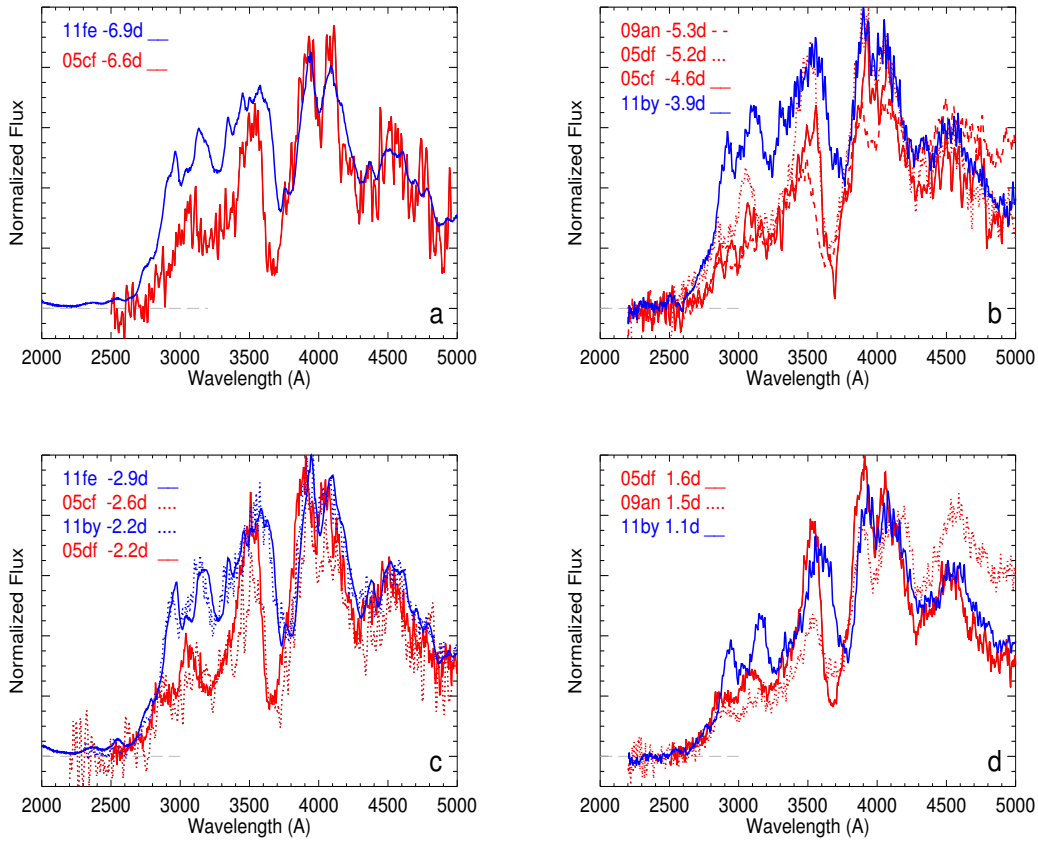

Figure 3.14: Near-UV spectra.
We compare NUV-red and NUV-blue UV spectra at epochs between -7 and $+2$ days. NUV-red spectra are displayed as red, while NUV-blue spectra are blue. Epochs are relative to B-band maximum light.

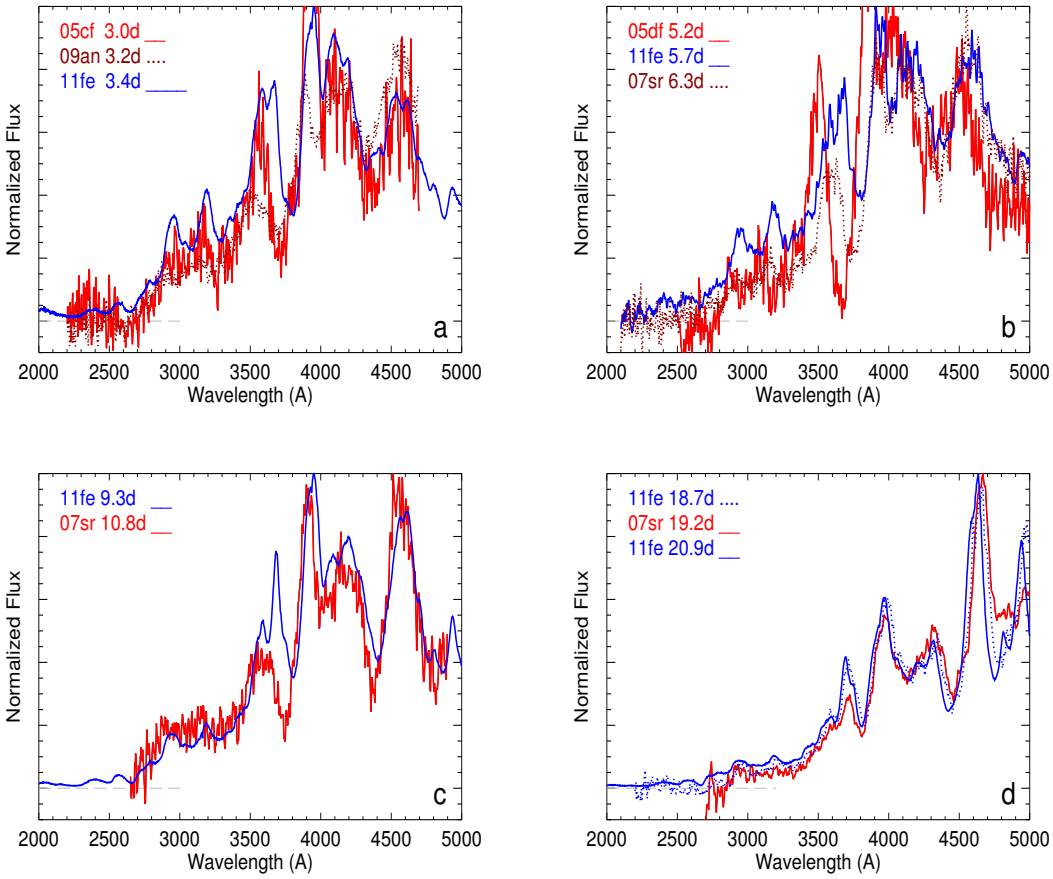

Figure 3.15: Near-UV spectra.
We compare NUV-red and NUV-blue UV spectra at epochs between +3 and +20 days. NUV-red spectra are displayed as red, while NUV-blue spectra are blue. Epochs are relative to B-band maximum light.

The evolution timescale we find is consistent with the photometric color trends in Figure 4 of Milne et al. (2013). The (*uvm2* - *u*), (*uvm2* -*v*), and (*uvw2* -*v*) colors of both subclasses were demonstrated to converge between +5 and +20 days. Also, in Milne et al. (2013)'s Figure 15, the low-resolution spectra are shown to converge around +5 days.

The differences between the NUV-blue and NUV-red continua that we find are similar to those presented in Milne et al. (2013) (Figures 13 & 15) for phases −2 days and later. The same is true for the mid-z, rest-frame UV spectra sample of Milne et al. (2015) (Figure 5) with the exception of their −7 day spectral comparison. At this epoch, their NUV-blue SN (03D4cj) shows a large lightcurve stretch, very weak Ca II H & K absorption, no Si II λ6355 absorption, and a well defined absorption feature around 4900Å; these characteristics suggest that this SN is a 1991T-like or 1999aa-like SN and is likely to have spectroscopic differences outside of the typical NUV-red and NUV-blue variations. For this reason, we think that we should avoid comparing our −7 day spectra to Milne et al. (2015) at this epoch.

In our spectral comparisons (Figures 3.14 and 3.15) we see a difference in the UV features for the epochs −7 through +10 days. Here, in addition to the continua differences, the NUV-blue spectra show double peaked features near 2900 and 3100Å. These features are weak or absent in the NUV-red spectra, which instead display a single peak near 3000Å. When we have multiple spectra for the same UV classification and epoch, we find consistent behavior of the features among spectra. Based on this sample, we conclude that these features constitute a fundamental difference between NUV-red and NUV-blue SNe Ia. This behavior was not detected by Milne et al. (2015) due to the low signal-to-noise of the mid-z SNe spectra within this wavelength range. It was also not detected in Milne et al. (2013) UV spectra sample (Figure 15), possibly due to the feature widths being just a few times greater than the *HST*-ACS

detector resolution of $\sim$ 50 Å/pix near 3000Å (Larsen et al., 2006). The optical spectral sample of Milne et al. (2013) displays hints of this behavior around the epochs +4 days, though the low signal-to-noise at the necessary wavelengths would have made a diagnosis difficult. We note that our conclusion is based on a relatively small number of SNe for which the effect of extinction has not been accounted for, and encourage further investigation of this matter.

The double peak features near 2900 and 3100Å at pre-maximum epochs bear resemblance to model spectra which attribute these features to UV emission in the outer ejecta layers (Walker et al., 2012). Interpretation of our observed spectroscopic feature diversity through this lens indicates that UV emission may play a role in the formation of the NUV-blue SNe flux while playing a reduced role for NUV-red SNe. The contrast in spectral features we observe at -7 days and gradual evolution toward unity around +10 days suggest that the UV emission is greatest at early times and then tapers off. We compare select epochs of our NUV spectra to the models of Walker et al. (2012) in Figure 3.16. We find that at the epochs -7 and -2 days the model features are a very good match to the features between $2700 - 3300$Å, a moderately good match between $3300 - 3900$Å, and a good match redward of this. We find that differing model atmospheric metallicities capture the double peak behavior of the NUV-blue spectra and single peak behavior of the NUV-red. At +6 days, we find that the model continua are a poorer match to both the NUV-red and NUV-blue SNe at wavelengths shortward of 3500Å, and that the features are roughly traced. Taken as a whole, this analysis suggests that lower metallicity in the outer atmospheric layers of NUV-blue SNe is partially responsible for the NUV dichotomy.

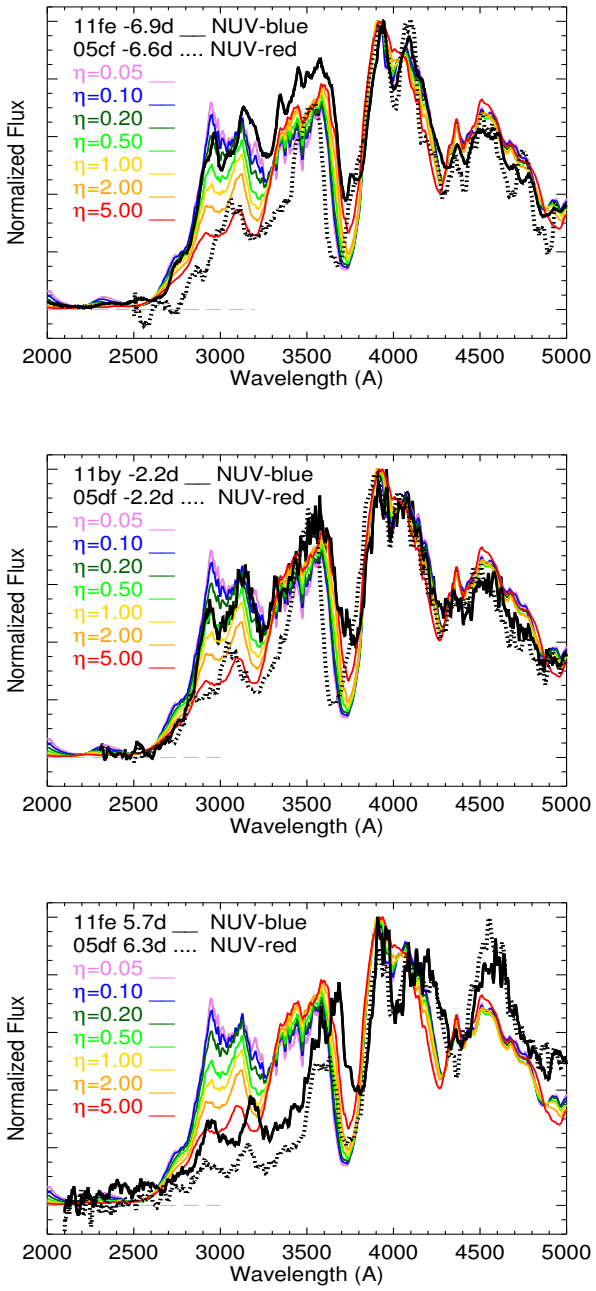

Figure 3.16: Near-UV spectra and model spectra.
Synthetic SNe Ia spectra for a SN near maximum light with $log(L_{bol}/L_{\odot}) = 9.6$ as modeled by Walker et al. (2012) are compared to NUV-blue and NUV-red observed spectra at $-7, -2, +6$ days. The η model parameter is an atmospheric metallicity scaling factor for elements with atomic number $Z > 20$.

4. THE UV-O-IR SPECTRAL ATLAS

We combine the UVOT UV spectra with optical and near-infrared spectra to produce time-series spectra between $1600 - 25000\,\text{Å}$ of SNe Ia near maximum light. We do this for eight SNe Ia with $0.9 < \Delta m_{15}(B) < 1.8$. The process utilized to produce these UVOIR spectra is outlined below.

4.1 Lightcurve Fits

We fit the UVOT and CSP photometry (Sections 2.2.1 & 2.1.1) with lightcurve templates using the SNooPy software (Burns et al., 2011). SNooPy was designed by the CSP collaboration to provide a robust lightcurve fitting method designed to work specifically with the CSP filter sets. As a result, SNooPy calculates lightcurve fits to the observed photometry using templates generated from CSP observations of low-z, low extinction SNe Ia. This was designed to reduce complications that might arise from systematic differences between filter sets and observing apperati used in template creation and observation. Template sets exist for each filter and capture the evolution of lightcurve shape with decline rate ($\Delta m_{15}(B)$). SNooPy performs an iterative fitting process in which it cycles through the templates to find the set which provide the best fit to the data, thus yielding the decline rate parameters, times of maximum light, and maximum magnitudes. Photometric errors are incorporated into the fitting process and typical lightcurve fitting errors are documented in Section 3 of Burns et al. (2011). The best fit templates are interpolated to a cadence of one day, which provides an empirical estimate for gaps in data (due to bad weather, observing complications and scheduling)

The SNooPy software was graciously modified by its author, Chris Burns, to accept the UVOT photometric filters. The UBV filters utilize the templates of the

corresponding CSP filters (uBV) by way of single-band K-corrections (S-corrections) (Suntzeff, 2000; Stritzinger et al., 2002). The UVW2, UVM2, and UVW1 filters each utilize a single template defined by the UVOT photometry of SN 2011fe (Brown et al., 2012b). These templates are scaled in magnitude and stretch parameters, and generally provide very good fits to normal SNe Ia photometry within -10 to $+30$ days of B-band maximum light. Our lightcurve fits make no attempt to correct for dust extinction, which we correct for in a later processing step.

4.2 Spectra

The optical spectra we select for use in the construction of UV-O-IR SEDs come from direct observations of the individual SNe. This is always true with the exception of a handful of epochs for SN 2007sr, for which no data were available because it was discovered a few days after B-band maximum. The spectra we select came mainly from the CSP (Folatelli et al. (2013); private communication with Nidia Morrell), and the archival data of Blondin et al. (2012) made available through WISeREP (Yaron & Gal-Yam, 2012). The sources of spectra used for each SN epoch and the wavelength ranges utilized are listed in Tables 4.2 - 4.9. A handful of spectra from additional sources and are listed in these tables when relevant.

The UV spectra we select for use in the construction of UV-O-IR SEDs come from two sources: our UV spectral atlas (Section 3) and the *HST* STIS spectral series of SN 2011fe (Mazzali et al., 2014). For each SN in the UV-O-IR sample, we select UV spectra based on the following criteria. When UV spectra of the individual SN were available, they were given highest priority. Next, when individual SN spectra were not available, substitute UV spectra were employed. The substitute spectra were drawn from SNe at similar phases relative to B-band maximum (within ± 3 days), with similar optical classifications, B-band decline rates ($\Delta m_{15}(B) \sim \pm 0.1$),

and UV classifications (when known). When no substitute spectra were available for an individual SN, only then do we substitute in template data (Hsiao et al., 2007). In most cases, some template spectra are added to the UV edge to extend the wavelength range to 1600Å. This was necessary to ensure full wavelength coverage of the UVOT photometric bands and enable synthetic photometry to be computed. While this approach is not ideal, it is justified for the purpose of computing UV-O-IR luminosities because the integrated flux in the extended regions is $< 1\%$ of the UV-O-IR integrated flux.

The majority of NIR spectra we select for use in the construction of UV-O-IR SEDs come from template data (Hsiao et al., 2007). For SN 2008hv we were able to obtain suitable NIR spectra of SN 2008hv and SN 2008ec, which is optically similar enough to merit substitution.

We utilize UV and optical spectra because we wish to create SEDs which accurately reflect the spectroscopic diversity of SNe Ia as functions of time and decline rate. SNe Ia optical velocity features are known to systematically vary with phase relative to maximum light (Childress et al., 2014), and the presence of ions and strengths of features are also known to vary as well (Maguire et al., 2014). Additionally, UV colors and spectra of both normal and peculiar SNe Ia have been demonstrated to vary with phase and decline rate as well (Brown et al., 2010; Wang et al., 2012; Milne et al., 2013; Brown et al., 2014c; Milne et al., 2015; Smitka et al., 2015). This implies that a single set of SNe templates designed to capture the average time behavior of SNe Ia does not capture subtle systematic differences among the spectra (Hsiao et al., 2007). It is common practice to utilize templates to approximate the SED when one does not have spectral information. This comes at the cost of introducing these systematic differences, which can negatively impact the downstream analysis. We utilize UV and optical spectra in order to generate a set of UV-O-IR templates

which do capture the time and decline rate differences. We quantify the differences in K-corrections calculated using templates and our UV-O-IR SEDs in Section 4.11.

4.3 Color Matching

Color matching is the process of modifying the flux values of a spectrum such that the integrated flux values for several individual filters (synthetic photometry) are in agreement with measured photometric values. We are required to utilize this process because the CSP spectroscopic data were not measured in absolute flux units, and thus require color matching to be placed on an absolute flux scale.

Our criteria for selecting SNe to be included in this analysis were that an individual SN must have UV, optical and NIR photometric coverage near maximum light, and optical spectra must be available with ~ 3 day or less cadence. Our color matching scheme treats the UV, optical and NIR realms independently of each other. In the optical, the spectra used are always direct observations of the individual SN at hand. In the UV, our spectra are not always direct observations of the individual SN, and UV spectra substitutions are made using SNe with similar optical decline rates and subclassifications when known. For this reason the UV portions of the UV-O-IR SEDs are often best thought of as representations of the decline rate and class of SN, rather than a representation of the exact SN referenced. We were unable to obtain the NIR spectral samples of Howie Marion or of the CSP II effort for use in our SEDs. For this reason the NIR portions of our SEDs are generated from template data (Hsiao et al., 2007) which only trace the time evolution of the NIR.

We color match spectra using our *synth.pro* routine (described above) to force agreement between the synthetic photometry and the SNooPy lightcurve fits to the CSP and UVOT photometry (Section 4.1). The color matching procedure steps are:

- *Photometry:* interpolate in time the measured photometric magnitudes from

the SNooPy lightcurve fits to the CSP and UVOT photometry at the appropriate date of the spectrum. This process is done for all photometric filters for which the spectrum completely encompasses the full wavelength range.

- *Synthetic photometry:* compute synthetic magnitudes using *synth.pro* for each filter that is completely encompassed by the spectrum.

- *Spline fit:* compute the offsets between the photometry and synthetic photometry. Then, fit a smooth, interpolating spline to these values as a function of the filter effective wavelengths.[1] This procedure defines a smooth curve passing through each of the loci.

- *Color match:* multiply the spline fit into the spectrum. This procedure 'corrects' the spectrum such that its synthetic photometry is in better agreement with its measured photometry. A multiplicative factor is used to maintain the relative strengths of spectral features.

- *Recompute:* the synthetic photometry of the spectrum is recomputed for the modified spectrum.

- *Repeat:* the entire procedure is repeated until the offsets between observed and synthetic photometry is of the same order as the photometric errors. This is usually one or two iterations. We perform the minimum number of iterations possible in order to reduce small residual 'wiggles' between effective wavelengths which can be introduced by the spline interpolation process.

Great care was put into the treatment of the spline fits for the portions of spectra blueward and redward of the maximum and minimum effective wavelengths. The

[1]This procedure utilizes the *splint* routine of Numerical Recipes in C: The Art of Scientific Computing (Second Edition), published by Cambridge University Press.

problem is that spline fits in these regions are unconstrained and can oftentimes exhibit wildly erratic behavior, which is very likely to be a mathematical residual and of a non-physical nature. Several options for constraining this behavior were investigated and two options were deemed to be the most appropriate: Firstly, a small extrapolation of the spectrum could be performed in either direction to ensure that an additional filter can be utilized; the extra portion of spectrum is subsequently trimmed off following the color matching procedure. The extrapolated portions of spectra are drawn from the spectral templates of Hsiao et al. (2007) and provide the most general representation of spectral behavior in the extrapolated regions. Secondly, the ends of the spline fits blueward and redward are trimmed and all values of the correcting spline are replaced with the values at the minimum or maximum wavelength spline knots.

We perform the color matching procedure independently for the UV, optical and NIR realms. This is done because the spectra are observed independently in these regions and because the final, color matched spectral regions of overlap provide a check of the quality of the finished data products.

4.4 UV-O-IR Compilation

Following color matching, the spectral pieces at each epoch are assembled into a single UV-O-IR spectrum. In this process we trim areas of wavelength overlap. The final spectra span the wavelengths $1600 - 25000$Å.

4.5 Extinction Corrections

The light comprising all of the photometry and spectroscopy measured by CSP and UVOT has been altered by dust extinction in both the Milky Way and host galaxies. We apply corrections for foreground Milky Way extinction to the SEDs using $E(B-V)$ values from the Schlafly & Finkbeiner (2011) recalibration of the

Table 4.1: Extinction and distance values.
The Milky Way and host galaxy reddening and extinction values, and distances to the host galaxies for the SNe Ia in the bolometric sample.

SN	$E(B-V)_{MW}$ (mag)	$E(B-V)_{Host}$ (mag)	R_{V_Host}	Distance Modulus (mag)
2005am	0.054(0.002)	0.053(0.017)	2.7(1.0)	32.85(0.23)
2007S	0.022(0.002)	0.478(0.026)	2.0(0.2)	33.98(0.19)
2007af	0.034(0.001)	0.178(0.024)	2.0(0.6)	31.72(0.07)
2007on	0.010(0.001)	0.003(0.001)	2.7(1.2)	31.51(0.05)
2007sr	0.047(0.001)	0.199(0.007)	2.0(0.8)	31.66(0.08)
2008hv	0.028(0.001)	0.074(0.023)	1.7(1.2)	33.76(0.16)
2009Y	0.102(0.002)	0.270(0.012)	2.0(0.6)	33.11(0.16)
2009cz	0.026(0.001)	0.091(0.011)	3.1(0.7)	34.82(0.16)

Schlegel et al. (1998) infrared dust maps[2]. Using these $E(B-V)$ values and the average Milky Way average ratio of total to selective extinction, $R_V = 3.1$, we applied the extinction law of Fitzpatrick (1999) using the *fm_unred.pro* package (Landsman, 1998). The Milky Way foreground $E(B-V)$ values applied for each SN are presented in Table 4.1.

We apply corrections for host galaxy extinction to the SEDs using a two part procedure. We first measured the host galaxy $E(B-V)$ and R_V values from the photometry. This process is carried out using the SNooPy lightcurve fitter's 'color_model' package. The host galaxy parameters are estimated by assuming an intrinsic set of SN colors and iteratively determining the most likely combination of $E(B-V)$ and R_V values that reproduce the photometric measurements. Burns et al. (2014) describes in great detail the basis for defining the intrinsic colors from a sample of nearby SNe Ia believed to have minimal dust extinction. This benchmark sample is used by the SNooPy software, which provides the measured host galaxy $E(B-V)$

[2]This research has made use of the NASA/IPAC Extragalactic Database (NED) which is operated by the Jet Propulsion Laboratory, California Institute of Technology, under contract with the National Aeronautics and Space Administration.

and R_V values. Burns et al. (2014) published host galaxy extinction values for for SNe 2005am, 2007S, 2007af, 2007on, and 2008hv. We used a local installation of SNooPy to solve for the extinction values for SNe 2007sr, 2009Y, and 2009cz. As was the case with Milky Way extinction, we applied corrections using the extinction law of Fitzpatrick (1999). The host galaxy $E(B-V)$ and R_V values utilized for each SN are presented in Table 4.1.

Following the application of the extinction corrections, the SEDs are in their final form. These are presented in Figures 4.1 - 4.8. The sources from which the SEDs component spectra are taken are documented in Tables 4.2 - 4.9.

4.6 Integration

The SED flux densities of the UV-O-IR spectra were integrated using trapezoidal integration at the resolution of the component spectra. Integrations were performed within the wavelength range $1600 - 25000\mathring{A}$.

4.7 Distances

We adopted distances to SNe 2007sr and 2007af from the Cepheid distances to the host galaxies presented by Riess et al. (2011). We adopted a distance to the host galaxy of SN 2007on from the mean Fornax cluster distance calculated by Jensen et al. (2015) using the infrared surface brightness fluctuations technique and the HST WFC3 instrument. We believe this is justified because NGC 1404 is very close to the center of the cluster. No low-uncertainty distance measurements independent of SNe Ia derived measurements were available for the remaining SNe, so for these we applied the technique of Mould et al. (2000), which relates recessional velocity of the host galaxy to distance by means of assuming a set of cosmological parameters and correcting for the host galaxy motion due to gravitational attraction from the Virgo, Great Attractor, and Shapley clusters. In these calculations we assume the

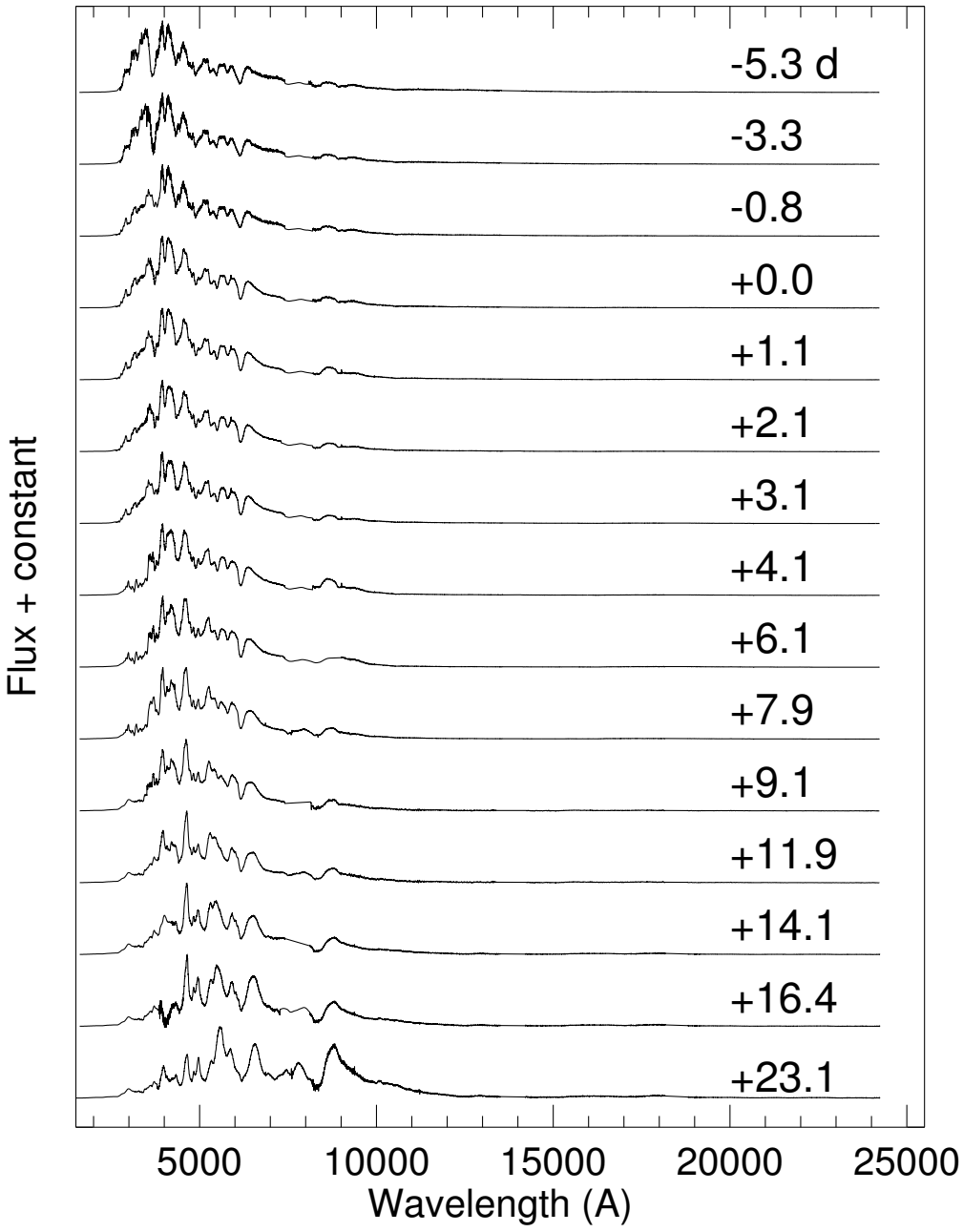

Figure 4.1: Time-series UV-O-IR spectral series of SN 2005am.

Table 4.2: Spectra sources of SN 2005am.

Spectra sources compiled in the UV-O-IR spectra of SN 2005am. Citation scheme: [1] This publication. [2] Blondin et al. (2012). [3] Folatelli et al. (2013). [4] Private communication with Howie Marion.

Phase	UV SN	UV Source	UV λ (Å)	Optical Source	Optical λ (Å)	NIR SN	NIR Source	NIR λ (Å)
-5.3	2009an	1	2750 – 3750	2	3750 – 8078	2005am	4	8078 – 24223
-3.3	2009an	1	2750 – 3500	2	3500 – 8200	2005am	4	8200 – 24223
-0.8	2005am	1	2600 – 3900	2	3900 – 8200	2005am	4	8200 – 24223
0	2005am	1	2600 – 3600	2	3600 – 8200	2005am	4	8200 – 24223
1.1	2005am	1	2600 – 3650	2	3650 – 8200	2005am	4	8200 – 24223
2.1	2005am	1	2600 – 3450	2	3450 – 8200	2005am	4	8200 – 24223
3.1	2005am	1	2600 – 3800	2	3800 – 8200	2005am	4	8200 – 24223
4.1	2008Q	1	2900 – 3550	2	3550 – 8200	2005am	4	8200 – 24223
6.1	2008Q	1	2900 – 3550	2	3550 – 8200	2005am	4	8200 – 24223
7.9	2008Q	1	2900 – 3900	3	3900 – 9235	2005am	4	9235 – 24223
9.1	2005am	1	3150 – 3500	2	3500 – 7411	2005am	4	8138 – 24223
11.9	2005am	1	3150 – 3800	3	3800 – 9235	2005am	4	9235 – 24223
14.1	2005am	1	3150 – 4200	2	4200 – 7411	2005am	4	8117 – 24245
16.4	2005am	1	3150 – 4500	3	4500 – 8117	2005am	4	8117 – 24245
23	2005am	1	3150 – 3800	3	3800 – 8200	2005am	4	8200 – 24245

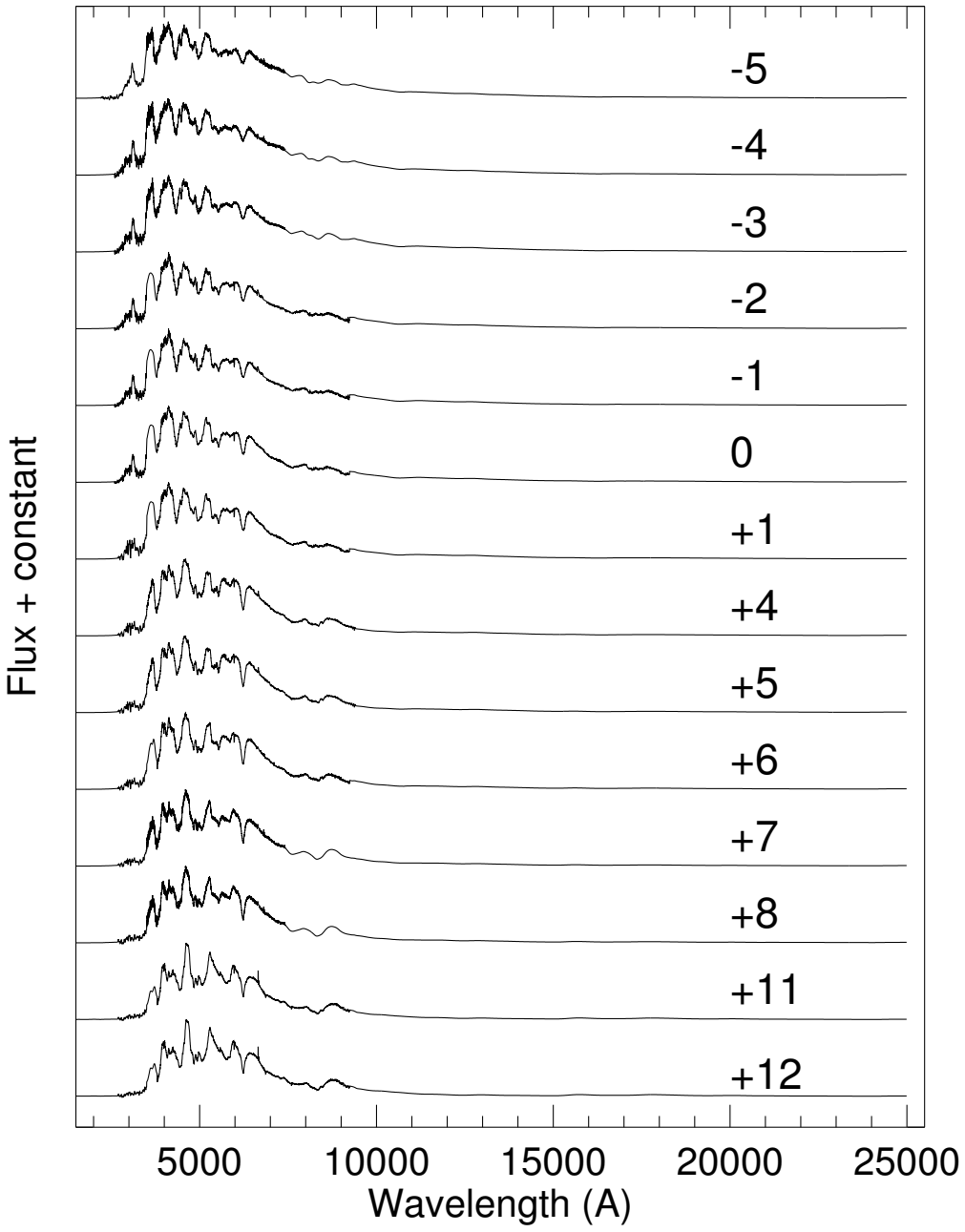

Figure 4.2: Time-series UV-O-IR spectral series of SN 2007S.

Table 4.3: Spectra sources of SN 2007S.
Spectra sources compiled in the UV-O-IR spectra of SN 2007S. Citation scheme: [1] This publication. [2] Blondin et al. (2012). [3] Folatelli et al. (2013). [4] Hsiao et al. (2007). [5] Silverman et al. (2012a).

Phase	UV SN	UV Source	UV λ (Å)	Optical Source	Optical λ (Å)	NIR Source
-5	iPTF14bdn	1	$2202 - 3500$	2	$3500 - 7414$	4
-4	iPTF14bdn	1	$2600 - 3500$	2	$3500 - 7417$	4
-3	iPTF14bdn	1	$2600 - 3500$	2	$3500 - 7417$	4
-2	iPTF14bdn	1	$2600 - 3500$	3	$3500 - 9235$	4
-1	iPTF14bdn	1	$2600 - 3500$	3	$3500 - 9235$	4
0	iPTF14bdn	1	$2600 - 3500$	3	$3500 - 9235$	4
1	iPTF14bdn	1	$2700 - 3500$	3	$3500 - 9235$	4
4	iPTF14bdn	1	$2700 - 3500$	5	$3500 - 10500$	4
5	iPTF14bdn	1	$2700 - 3500$	5	$3500 - 10500$	4
6	iPTF14bdn	1	$2700 - 3500$	3	$3500 - 9235$	4
7	iPTF14bdn	1	$2700 - 3500$	2	$3500 - 7417$	4
8	iPTF14bdn	1	$2700 - 3500$	2	$3500 - 7417$	4
11	iPTF14bdn	1	$2700 - 3500$	3	$3500 - 9235$	4
12	iPTF14bdn	1	$2700 - 3500$	3	$3500 - 9235$	4

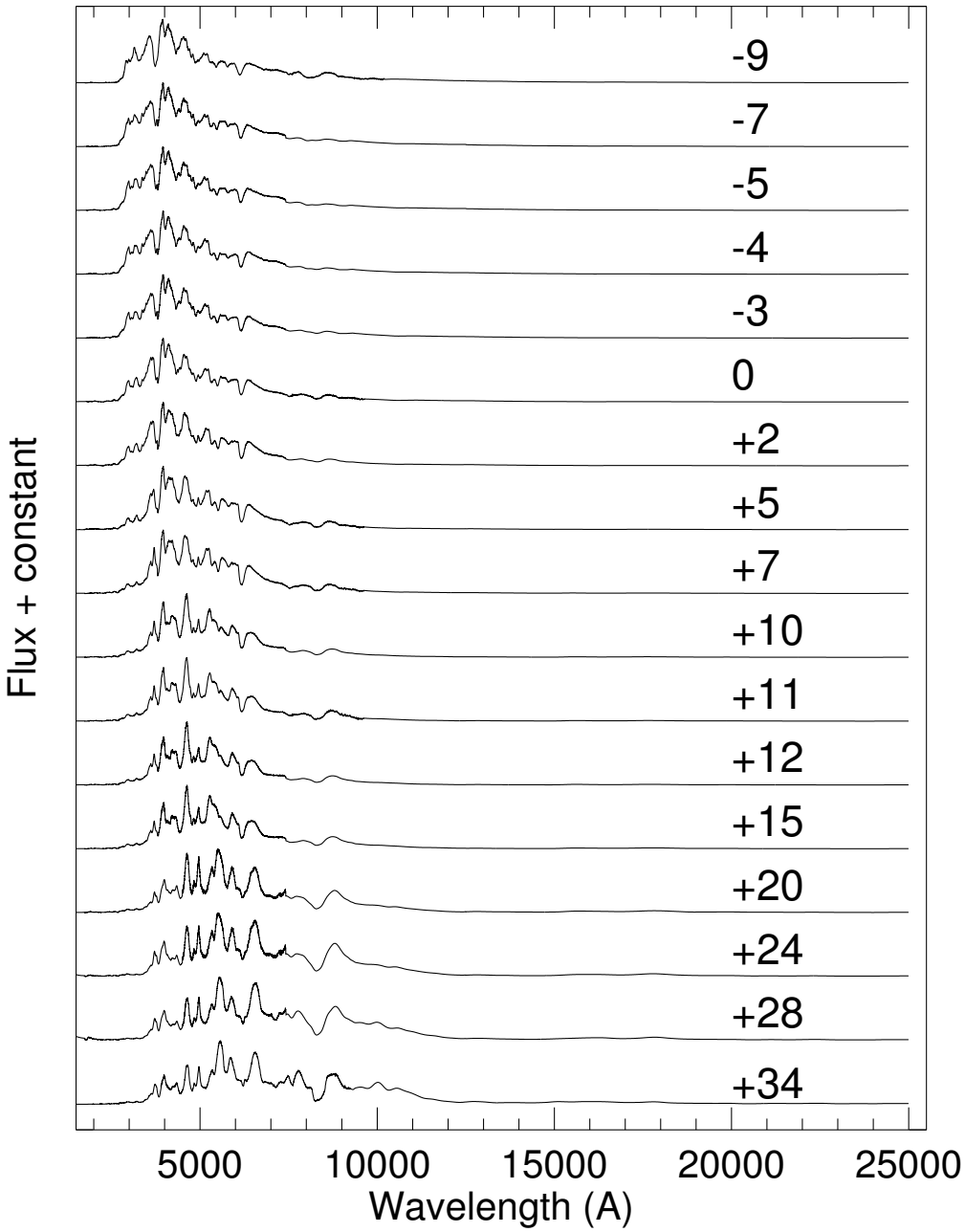

Figure 4.3: Time-series UV-O-IR spectral series of SN 2007af.

Table 4.4: Spectra sources of SN 2007af.
Spectra sources compiled in the UV-O-IR spectra of SN 2007af. Citation scheme: [1] Mazzali et al. (2014). [2] Blondin et al. (2012). [3] Folatelli et al. (2013). [4] Hsiao et al. (2007), [5] Smitka et al. (2016).

Phase	UV SN	UV Source	UV λ (Å)	Optical Source	Optical λ (Å)	NIR Source
-9	2005df	5	$2600 - 3800$	3	$3800 - 10200$	4
-7	2005df	5	$2600 - 3800$	2	$3800 - 7414$	4
-5	2005df	5	$2600 - 3800$	2	$3800 - 7414$	4
-4	2005df	5	$2600 - 3800$	2	$3800 - 7414$	4
-3	2005df	5	$2600 - 3800$	2	$3800 - 7414$	4
0	2005df	5	$2600 - 3800$	3	$3800 - 9645$	4
2	2005df	5	$2600 - 3800$	2	$3800 - 7414$	4
5	2005df	5	$2850 - 3800$	3	$3800 - 9625$	4
7	2007sr	5	$2200 - 3800$	3	$3800 - 9625$	4
10	2007sr	5	$2700 - 3800$	2	$3800 - 7414$	4
11	2007sr	5	$2700 - 3800$	3	$3800 - 9607$	4
12	2007sr	5	$2700 - 3800$	2	$3800 - 7414$	4
15	2007sr	5	$2500 - 3800$	2	$3800 - 7414$	4
20	2007sr	5	$2700 - 4500$	2	$4500 - 7414$	4
24	2007sr	5	$2700 - 4500$	2	$4500 - 7414$	4
28	2011fe	1	$1748 - 4500$	2	$4500 - 7414$	4
34	2011fe	1	$1748 - 3900$	3	$3900 - 9235$	4

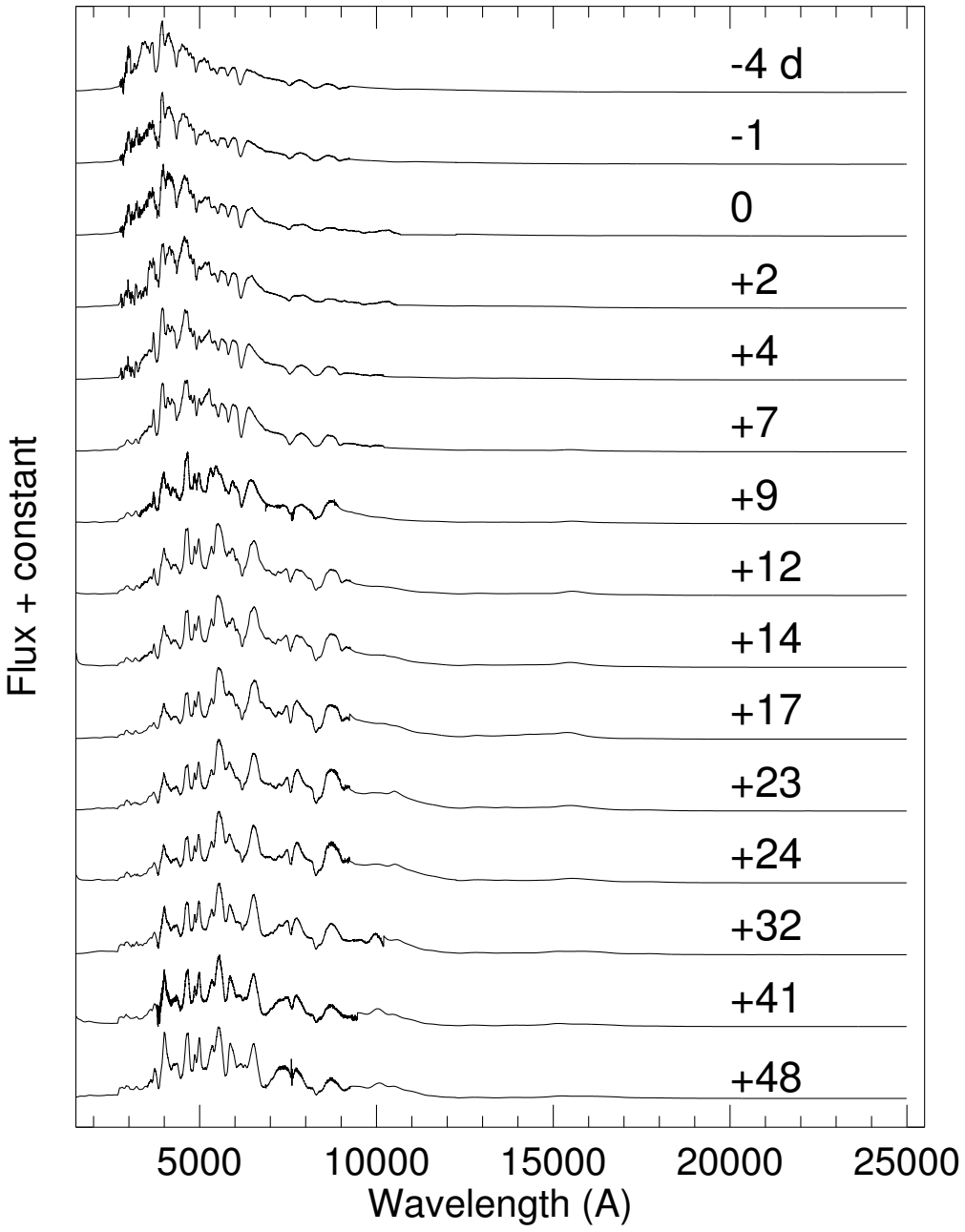

Figure 4.4: Time-series UV-O-IR spectral series of SN 2007on.

Table 4.5: Spectra sources of SN 2007on.
Spectra sources compiled in the UV-O-IR spectra of SN 2007on. Citation scheme: [1] This publication. [2] Folatelli et al. (2013). [3] Hsiao et al. (2007).

Phase	UV SN	UV Source	UV λ (Å)	Optical Source	Optical λ (Å)	NIR Source
-4	2008Q	1	$2752 - 3050$	2	$3050 - 9235$	3
-1	2008Q	1	$2752 - 3900$	2	$3900 - 9235$	3
0	2008Q	1	$2752 - 4050$	2	$4050 - 10674$	3
2	2008Q	1	$2758 - 4350$	2	$4350 - 10600$	3
4	2008Q	1	$2758 - 3300$	2	$3300 - 10500$	3
7	Template	3	...	2	$3300 - 10500$	3
9	Template	3	...	2	$3300 - 9472$	3
12	Template	3	...	2	$3300 - 9260$	3
14	Template	3	...	2	$3300 - 9260$	3
17	Template	3	...	2	$3800 - 9235$	3
23	Template	3	...	2	$3800 - 9235$	3
24	Template	3	...	2	$3800 - 9235$	3
32	Template	3	...	2	$3200 - 10200$	3
41	Template	3	...	2	$3800 - 9454$	3
48	Template	3	...	2	$3300 - 9260$	3

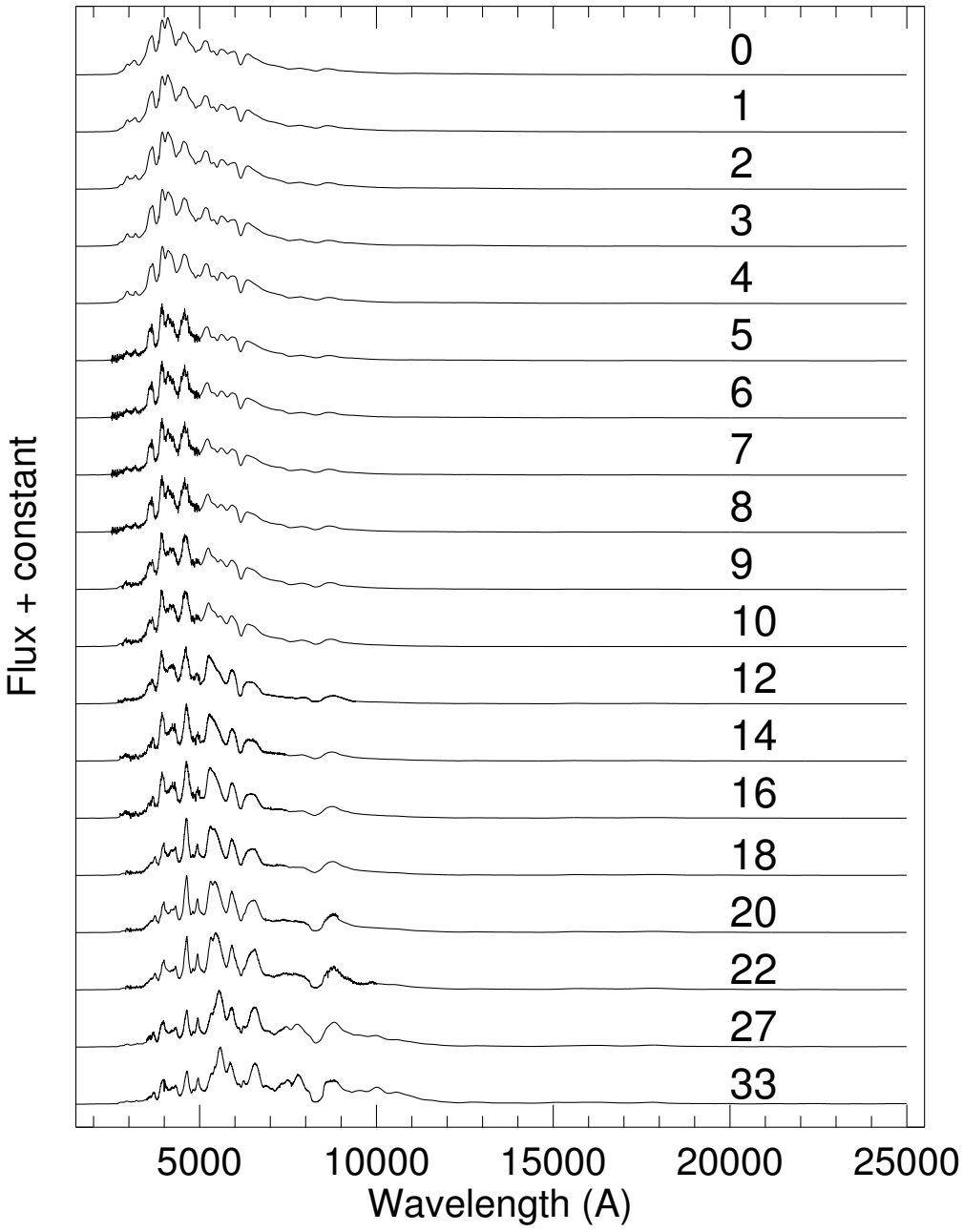

Figure 4.5: Time-series UV-O-IR spectral series of SN 2007sr.

Table 4.6: Spectra sources of SN 2007sr.
Spectra sources compiled in the UV-O-IR spectra of SN 2007sr. Citation scheme: [1] This publication. [2] Folatelli et al. (2013). [3] Blondin et al. (2012). [4] Hsiao et al. (2007).

Phase	UV SN	UV Source	UV λ (Å)	Optical Source	Optical λ (Å)	NIR Source
0	Template	4	...	4	...	4
1	Template	4	...	4	...	4
2	Template	4	...	4	...	4
3	Template	4	...	4	...	4
4	Template	4	...	4	...	4
5	2007sr	1	2500 − 5000	4	...	4
6	2007sr	1	2500 − 5000	4	...	4
7	2007sr	1	2500 − 5000	4	...	4
8	2007sr	1	2500 − 5000	4	...	4
9	2007sr	1	2800 − 5000	4	...	4
10	2007sr	1	2800 − 5000	4	...	4
12	2007sr	1	2750 − 5000	2	5000 − 9400	4
14	2007sr	1	2750 − 5000	3	5000 − 7421	4
16	2007sr	1	2903 − 4000	3	4000 − 7419	4
18	2007sr	1	2903 − 4000	3	4000 − 7423	4
20	2007sr	1	2903 − 4000	2	4000 − 8910	4
22	2007sr	1	2903 − 4000	2	4000 − 10000	4
27	Template	4	...	3	3500 − 7418	4
33	Template	4	...	2	3500 − 8910	4

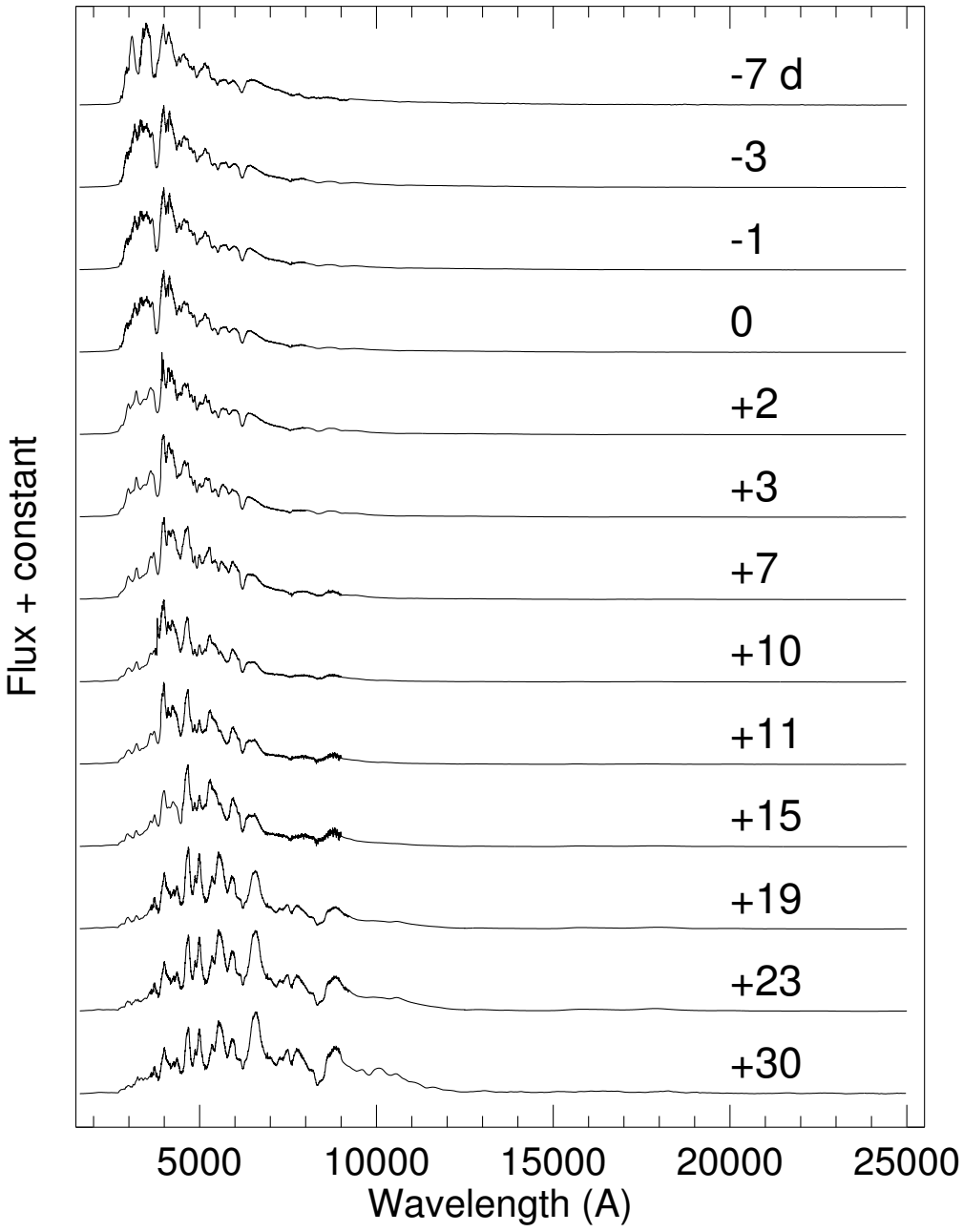

Figure 4.6: Time-series UV-O-IR spectral series of SN 2008hv.

Table 4.7: Spectra sources of SN 2008hv.

Spectra sources compiled in the UV-O-IR spectra of SN 2008hv. Citation scheme: [1] Smitka et al. (2016). [2] Folatelli et al. (2013). [3] Mazzali et al. (2014). [4] Private communication with Howie Marion, [5] Hsiao et al. (2007).

Phase	UV SN	UV Source	UV λ (Å)	Optical Source	Optical λ (Å)	NIR SN	NIR Source	NIR λ (Å)
-7	2011fe	3	1900 – 3300	2	3300 – 9210	2008hv	4	10000 – 24275
-3	2011fe	3	1900 – 3900	2	3900 – 9429	2008ec	4	9429 – 25000
-1	2011fe	3	1900 – 3900	2	3900 – 9429	2008ec	4	9429 – 25000
0	2011fe	3	1900 – 3900	2	3900 – 9429	2008ec	4	9429 – 25000
2	2011fe	3	1600 – 3900	2	3900 – 8000	2008ec	4	8000 – 25000
3	2011fe	3	1600 – 3900	2	3900 – 8000	2008ec	4	8000 – 25000
7	2011fe	1	2211 – 3900	2	3900 – 9000	2008ec	4	9000 – 25000
10	2011fe	3	1750 – 3750	2	3750 – 9000	2008ec	4	9000 – 25000
11	2011fe	3	1750 – 3900	2	3900 – 9000	2008ec	4	9000 – 25000
15	2011fe	1	2213 – 4500	2	4500 – 9000	Template	5	...
19	2011fe	3	1750 – 3600	2	3600 – 9210	Template	5	...
23	2011fe	3	1750 – 3600	2	3600 – 9210	Template	5	...
30	2011fe	3	1750 – 3600	2	3600 – 9210	Template	5	...

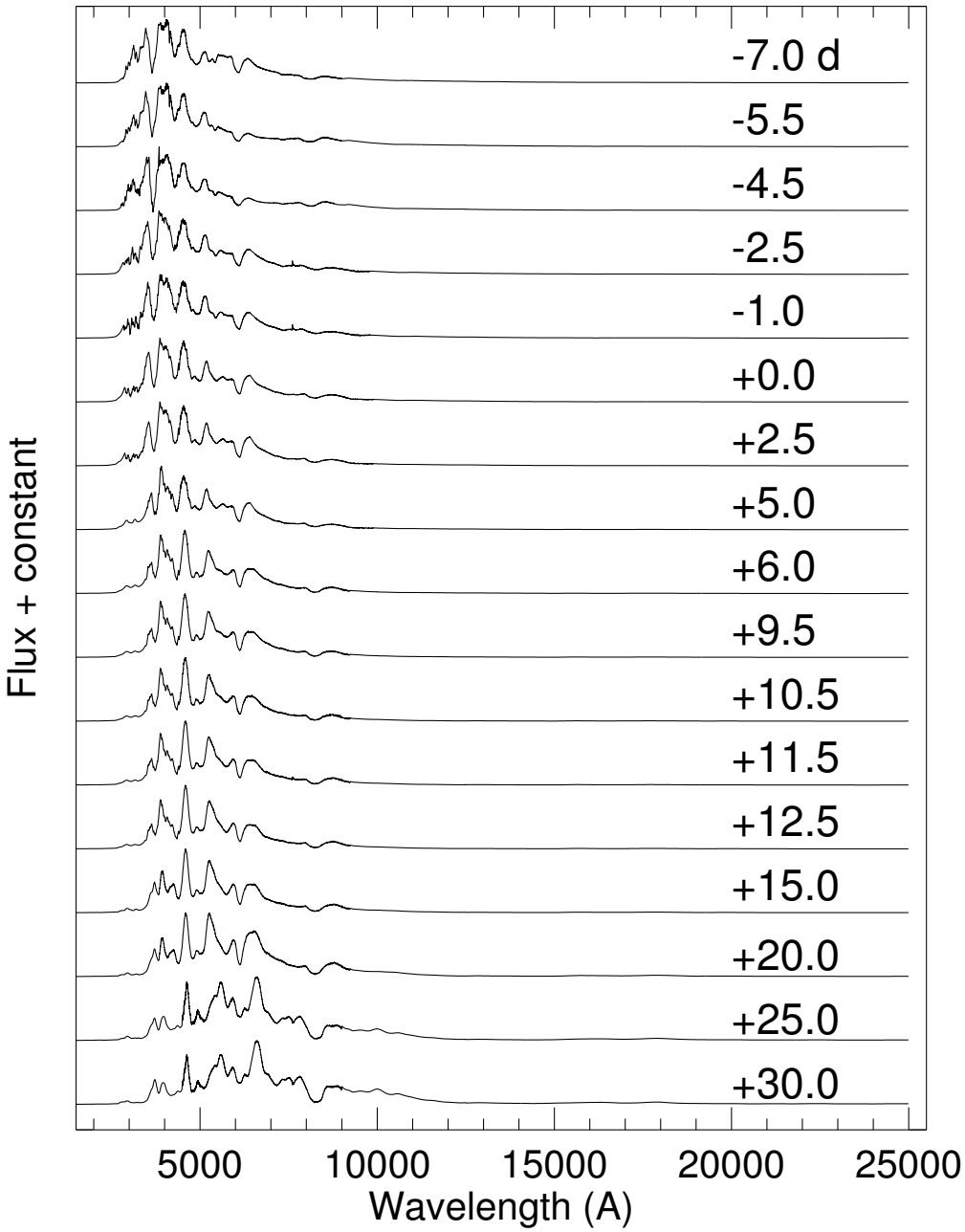

Figure 4.7: Time-series UV-O-IR spectral series of SN 2009Y.

Table 4.8: Spectra sources of SN 2009Y.
Spectra sources compiled in the UV-O-IR spectra of SN 2009Y. Citation scheme: [1] This publication. [2] Folatelli et al. (2013). [3] Hsiao et al. (2007).

Phase	UV SN	UV Source	UV λ (Å)	Optical Source	Optical λ (Å)	NIR Source
-7.0	2009Y	1	$2802 - 3900$	2	$3900 - 9000$	3
-5.5	2009Y	1	$2802 - 3900$	2	$3900 - 9000$	3
-4.5	2009Y	1	$2752 - 3850$	2	$3850 - 8797$	3
-2.5	2009Y	1	$2850 - 4300$	2	$4300 - 9799$	3
-1.0	2009Y	1	$2850 - 4400$	2	$4400 - 9799$	3
0.0	2009Y	1	$2902 - 4400$	2	$4400 - 9899$	3
2.5	2009Y	1	$2902 - 4400$	2	$4400 - 9899$	3
5.0	2009Y	1	$3500 - 4300$	2	$4300 - 9899$	3
6.0	2009Y	1	$3500 - 4400$	2	$4400 - 9235$	3
9.5	2009Y	1	$3500 - 4400$	2	$4400 - 9235$	3
10.5	2009Y	1	$3500 - 4400$	2	$4400 - 9235$	3
11.5	2009Y	1	$3500 - 4400$	2	$4400 - 9235$	3
12.5	2009Y	1	$3500 - 4400$	2	$4400 - 9235$	3
15.0	Template	3	...	2	$3850 - 9235$	3
20.0	Template	3	...	2	$3850 - 9235$	3
25.0	Template	3	...	2	$4500 - 9000$	3
30.0	Template	3	...	2	$4500 - 9000$	3

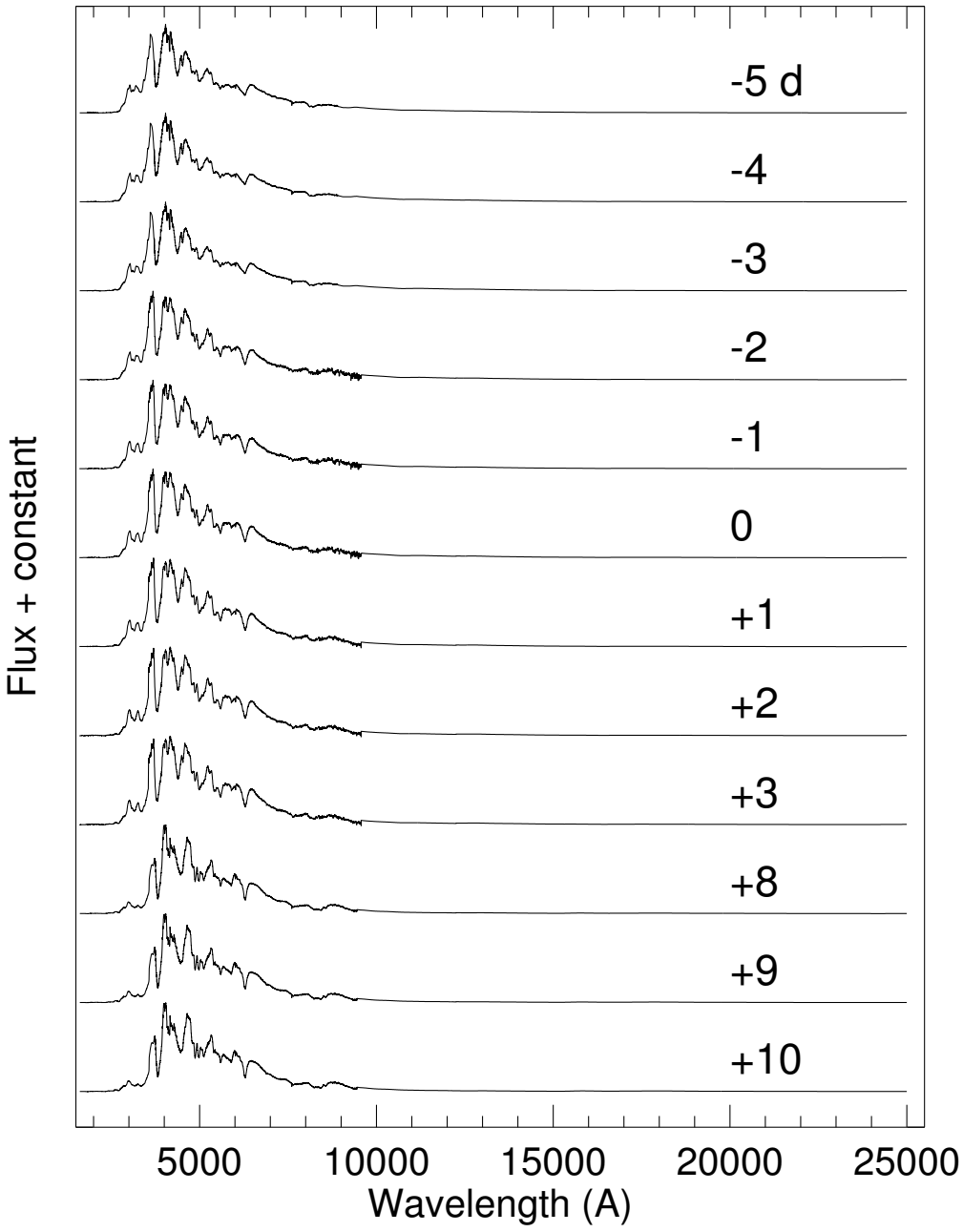

Figure 4.8: Time-series UV-O-IR spectral series of SN 2009cz.

Table 4.9: Spectra sources of SN 2009cz.
Spectra sources compiled in the UV-O-IR spectra of SN 2009cz. Citation scheme: [1] Mazzali et al. (2014) [2] Private communication with Nidia Morrell. [3] Hsiao et al. (2007).

Phase	UV SN	UV Source	UV λ	Optical Source	Optical λ	NIR Source
-5	2011fe	1	$1817 - 3600$	2	$3600 - 9435$	3
-4	2011fe	1	$1817 - 3600$	2	$3600 - 9435$	3
-3	2011fe	1	$1817 - 3600$	2	$3600 - 9435$	3
-2	2011fe	1	$1817 - 3550$	2	$3550 - 9568$	3
-1	2011fe	1	$1815 - 3550$	2	$3550 - 9568$	3
0	2011fe	1	$1815 - 3550$	2	$3550 - 9568$	3
1	2011fe	1	$1815 - 3550$	2	$3550 - 9567$	3
2	2011fe	1	$1600 - 3550$	2	$3550 - 9567$	3
3	2011fe	1	$1600 - 3550$	2	$3550 - 9567$	3
8	2011fe	1	$1776 - 3570$	2	$3570 - 9445$	3
9	2011fe	1	$1776 - 3570$	2	$3570 - 9445$	3
10	2011fe	1	$1776 - 3570$	2	$3570 - 9445$	3

Table 4.10: Details of the SNe in our bolometric sample.

SN	$\Delta m_{15}(B)$ (mag)	$JD\,B_{Max}$ (+2450000)	$JD\,Bolo_{Max}$ (+2450000)	Peak Luminosity ($\frac{erg}{sec} \times 10^{43}$)	^{56}Ni Mass ($M_{\odot}$)
2005am	1.51(08)	3436.6	3436.3	1.49(24)	0.61(10)
2007S	0.95(03)	4144.7	4143.3	1.71(35)	0.89(18)
2007af	1.20(03)	4174.7	4173.4	1.08(15)	0.47(07)
2007on	1.86(03)	4420.2	4419.1	0.66(10)	0.26(04)
2007sr	0.92(04)	4449.4	4449.4	1.51(27)	0.68(12)
2008hv	1.25(01)	4816.8	4816.3	1.24(21)	0.55(09)
2009Y	0.88(06)	4876.4	4875.5	2.35(50)	1.14(24)
2009cz	0.92(03)	4943.5	4941.9	1.55(24)	0.67(10)

cosmological prarameters: $H_o = 73.0$, $\Omega_{matter} = 0.27$, and $\Omega_{vacuum} = 0.73$, redshifts measured relative to the cosmic microwave background standard of rest, and add an uncertainty in radial velocity of $300\frac{km}{sec}$ due to uncertainty in the peculiar velocities.[3] Our adopted distance moduli values are presented in Table 4.1.

4.8 UV-O-IR Luminosities

Next, to calculate the SN UV-O-IR luminosities from the integrated fluxes, we utilized the basic flux-luminosity distance definition,

$$L = 4\pi D_L^2 F, \tag{4.1}$$

where L is the UV-O-IR luminosity, D_L is the luminosity distance (Section 4.7), F is the integrated flux (Section 4.6), and π is delicious. The UV-O-IR luminosities ('bolometric lightcurves') are presented in Figure 4.9. We calculated peak luminosities and the Julian dates at which these occur using smooth interpolating spline fits (Table 4.10).

[3]This research has made use of the NASA/IPAC Extragalactic Database (NED) which is operated by the Jet Propulsion Laboratory, California Institute of Technology, under contract with the National Aeronautics and Space Administration.

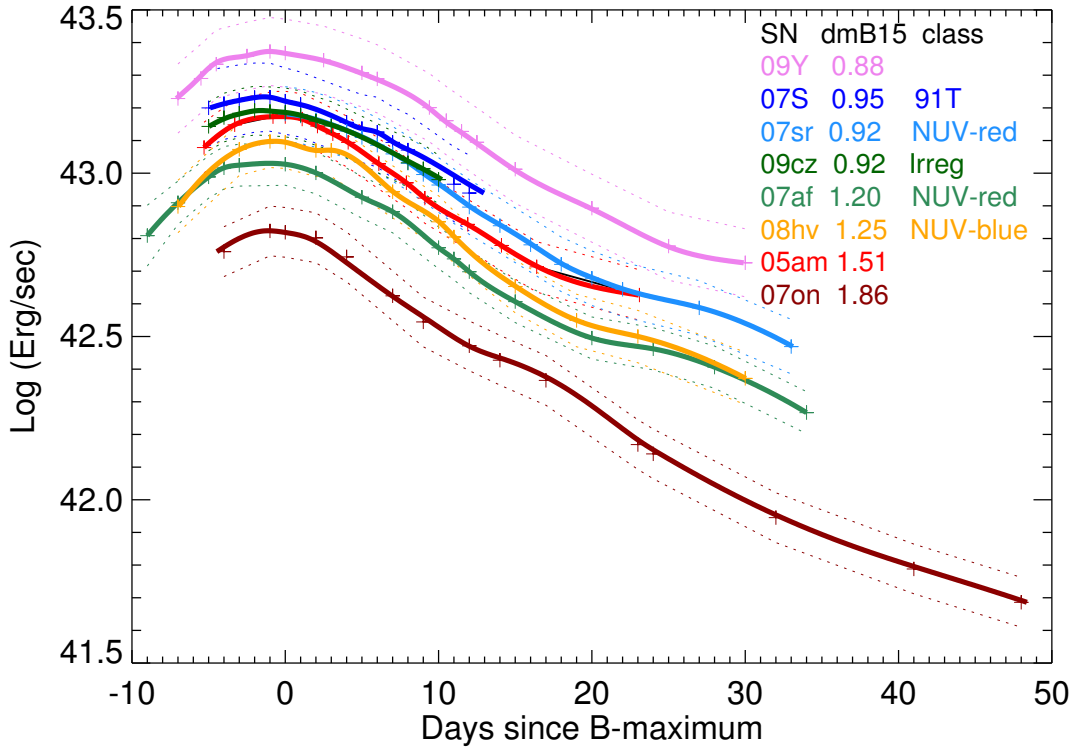

Figure 4.9: UV-O-IR integrated luminosities vs SN phase.
UV-O-IR luminosities calculated from integrating the SNe SEDs that were color-matched to the photometry, Milky Way and host galaxy extinction corrected, and distance corrected. The curves shown are smooth interpolating spline fits to the data. Decline rates ($\Delta m_{15}(B)$) are presented to demonstrate that we observe slow-declining SNe Ia to be more luminous than fast-declining SNe Ia. Error contours are shown as dashed curves, and were calculated according to the prescription in Section 4.9.

In Figure 4.9 we display the optical decline rates ($\Delta m_{15}(B)$) of the individual SNe to demonstrate that we observe slow-declining SNe Ia to be more luminous than fast-declining SNe Ia. The physical interpretation follows that peak luminosity coincides with the peak of energy injection into the atmosphere by radioactive decay, and thus is directly proportional to the total mass of ^{56}Ni synthesized (Arnett, 1982; Arnett et al., 1985).

4.9 Luminosity Uncertainties

The uncertainties associated with the measurements of the SN photometry, Milky Way extinction, host galaxy extinction, and distances all effect the SN luminosities we calculate. We calculate uncertainties for each SN at each epoch at which we make a luminosity measurement.

The contribution of photometric uncertainties to the color-matched SEDs are calculated using the method of Bevington & Robinson (2003),

$$P = F(U, V, W, \ldots), \tag{4.2}$$

where P represents the final integrated sum, F represents a complex function applied to the SEDs (the color-matching process), and U,V,W, ... represent the filter band-passes used in making the photometric measurements. In this form, the uncertainty of each filter's contribution is calculated iteratively as,

$$d \otimes U = F(U + dU,\, V,\, W,\, \ldots) \tag{4.3}$$

$$d \otimes V = F(U,\, V + dV,\, W,\, \ldots) \tag{4.4}$$

$$d \otimes W = F(U,\, V,\, W + dW,\, \ldots), \tag{4.5}$$

and the total photometric uncertainty for the epoch is,

$$dP^2 = (\, d \otimes U)^2 + (d \otimes V)^2 + (d \otimes W)^2 + \ldots. \tag{4.6}$$

The uncertainties associated with both Milky Way and host galaxy extinction corrections were calculated using the prescription outlined in the extinction law documentation of Fitzpatrick (1999) (Section 3). For both extinction contributions, the uncertainty at each epoch was calculated as,

$$dE^2 = dE(B-V)^2 \times k^2 + E(B-V)^2 \times dk^2 + dR_V^2 \times E(B-V)^2 + R_V^2 \times dE(B-V)^2, \tag{4.7}$$

where k is the extinction law and dk is its uncertainty function (provided in Fitzpatrick, 1999), and the $E(B-V)$ and R_V values correspond to either the Milky Way or host galaxy.

The distance uncertainties we adopted for SNe 2007sr, 2007af, and 2007on were the uncertainties in the distance moduli to the host galaxies and the mean Fornax Cluster value presented by Riess et al. (2011); Jensen et al. (2015), respectively. The uncertianties we adopted for the five SNe without redshift-independent distances were quantified using the uncertainties of the radial velocity measurements used in measuring the redshift, the $300\frac{km}{sec}$ assumed uncertainty in peculiar velocity relative to the CMB frame of rest, and the uncertainty of the gravitational potential corrections of Mould et al. (2000).

In Table 4.11, for each SN at B-band maximum light we present values for the four sources of uncertainty. The total uncertainties presented are these four values summed in quadrature. Uncertainty estimates for each SN luminosity measurement

Table 4.11: Luminosity uncertainty.
We present uncertainties in the calculated luminosities. We show uncertainties for each component of the bolometric lightcurve calculation process. Values were calculated at each epoch for which we make a luminosity measurement. For simplicity, we present only the values at maximum light. Values are given in units of bolometric magnitudes.

SN	Photometric (mag)	MW Extinction (mag)	Host Extinction (mag)	Distance (mag)	Total (mag)
2005am	0.02	0.01	0.09	0.23	0.19
2007S	0.03	0.01	0.16	0.18	0.25
2007af	0.01	0.01	0.14	0.07	0.16
2007on	0.01	0.01	0.01	0.05	0.05
2007sr	0.01	0.03	0.19	0.08	0.21
2008hv	0.02	0.01	0.12	0.15	0.20
2009Y	0.01	0.02	0.20	0.15	0.26
2009cz	0.02	0.01	0.09	0.15	0.19

are presented as the dotted curves in Figure 4.9.

4.10 Nickel Synthesis

The energy radiated by the SN at peak brightness and earlier is powered primarily by the radioactive decay of ^{56}Ni synthesized in a SN Ia explosion. Using our UV-O-IR luminosities, we estimated the synthesized ^{56}Ni mass using "Arnett's rule" (Arnett, 1982; Arnett et al., 1985), which states that the peak bolometric luminosity of a SN Ia is proportional to the rate of ^{56}Ni radioactive decay, and thus directly proportional to the mass of synthesized ^{56}Ni. A simple representation is presented by Stritzinger & Leibundgut (2005) as:

$$L_{max} = (6.45\, e^{\frac{-t_r}{8.8}} + 1.45\, e^{\frac{-t_r}{111.3}})\,(\frac{M_{Ni}}{M_\odot}) \times 10^{43}\, erg\, s^{-1}, \tag{4.8}$$

where L_{max} is the maximum luminosity of the bolometric lightcurve, t_r is the rise time of the bolometric lightcurve, and M_{Ni} is the mass of ^{56}Ni synthesized in the

explosion.

To measure the peak luminosities of our UV-O-IR lightcurves we calculated interpolating spline fits to the lightcurve data. Fits were calculated with 0.1 day time resolution. The spline fits for each SN are presented in Figure 4.9. The maximum luminosities and the times at which we measure them to occur are presented in Table 4.10.

To measure rough rise times of the UV-O-IR lightcurves, we performed template fitting using the UV-O-IR lightcurve of SN 2011fe (Pereira et al., 2013) and the SN 2011fe explosion time of Nugent et al. (2011). Template fitting consisted of aligning the luminosity maxima and applying a multiplicative stretch factor to the time axis; the times of explosion relative to the times of maximum light are scaled by the best fitting stretch factors. Figure 4.10 presents the calculated ^{56}Ni masses as a function of decline rate.

4.11 K-Corrections

As discussed in Section 1.3, K-corrections are utilized to compare photometric observations of targets at different redshifts by taking into account the photometric filter transmission functions, target SED, and redshift. To quantify the effect of the SED on the K-correction, we performed identical calculations using our bolometric SEDs and the SN templates of Hsiao et al. (2007). To facilitate this, we processed the templates using the same pipeline as was used in the generation of the bolometric SEDs (color-matching, Milky Way and host-galaxy extinction corrections.) The UV portions of our bolometric SED are generated from a much greater spectroscopic sample than the sample used in generating the templates. For this reason, we chose to focus our analysis on the UV and blue portions of the SEDs. Specifically, our analysis sought to quantify the differences in cross-band K-corrections calculated in

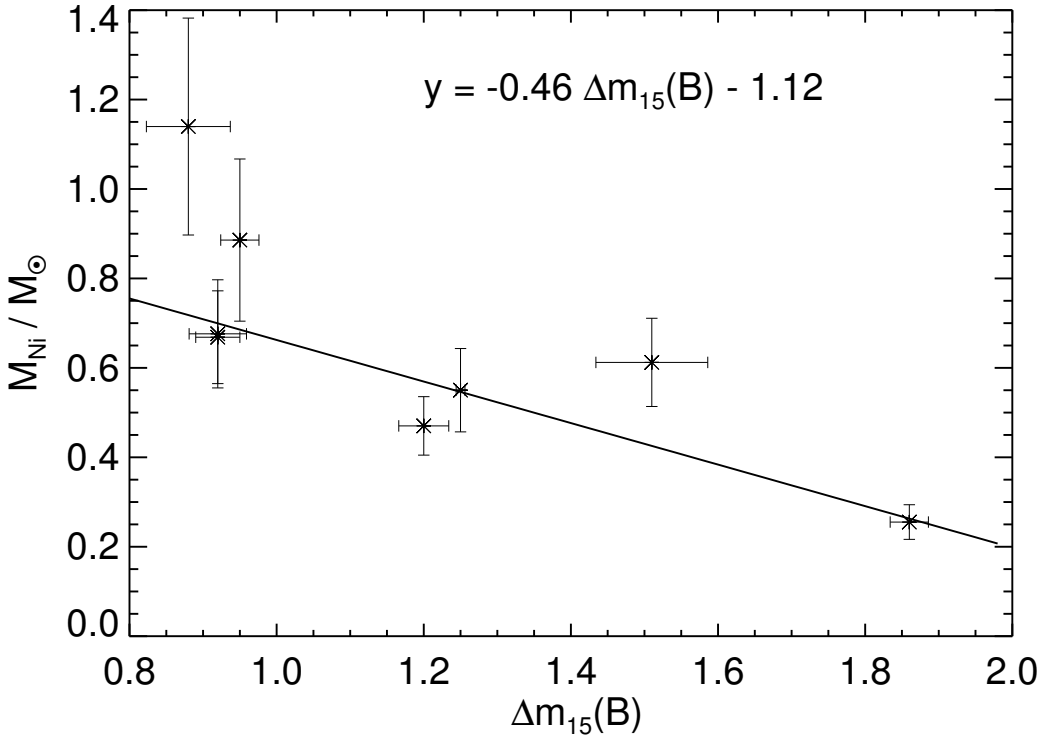

Figure 4.10: Synthesized ^{56}Ni vs $\Delta m_{15}(B)$.
Synthesized ^{56}Ni calculated using Arnett's rule vs optical decline rate. We demonstrate that optical SNe decline rate correlates with synthesized ^{56}Ni mass.

the *UVM2*, *UVW1*, u_{CSP}, and B_{CSP} bands at redshifts which will be monitored in future large surveys.

For each of the *UVM2*, *UVW1*, u_{CSP}, and B_{CSP} filters we calculated the redshifts at which there would be maximum overlap of the SED portions sampled by the rest-frame filter and an observed-frame filter. This limits our analysis to the 'best case' scenarios in which the wavelength ranges of the SEDs sampled by the rest-frame and observed-frame are most similar.

In Figure 4.11 we present cross-band K-corrections vs SN phase for the rest-frame B_{CSP} filter for the observed frame g_{CSP}, V_{CSP}, and r_{CSP} bands at redshifts of 0.14, 0.20, and 0.45, respectively. The left column of plots display the K-correction magnitudes as calculated using our bolometric SEDs. K-corrections were also calculated using the template SEDs, and are not shown. The $\Delta m_{15}(B)$ decline rates are demarked using the color scheme shown in the upper, left plot. The right column of plots display the differences in K-correction magnitudes between the calculations using our bolometric SEDs and the templates. We show that for the full range of phases that we studied, using the template SEDs introduces a systematic bias trending with $\Delta m_{15}(B)$ decline rate. We observe that the K-correction magnitudes agree for our SNe with $\Delta m_{15}(B)$ values near the mean value of 1.2, and that the magnitudes diverge as the $\Delta m_{15}(B)$ values diverge from the mean. This trend is roughly symmetric around the mean $\Delta m_{15}(B)$ value. We interpret this as an indication that subtle differences in feature strengths exist between the bolometric and template SEDs, and that these differences are coupled to the $\Delta m_{15}(B)$ decline rate. At B-band maximum light, we estimate that by neglecting the $\Delta m_{15}(B)$ factor, one introduces an error as large as ± 0.04 mag for B cross-band K-corrections calculated using the template SEDs. Within the phase ranges we studied, the largest error introduced is ± 0.08 mag.

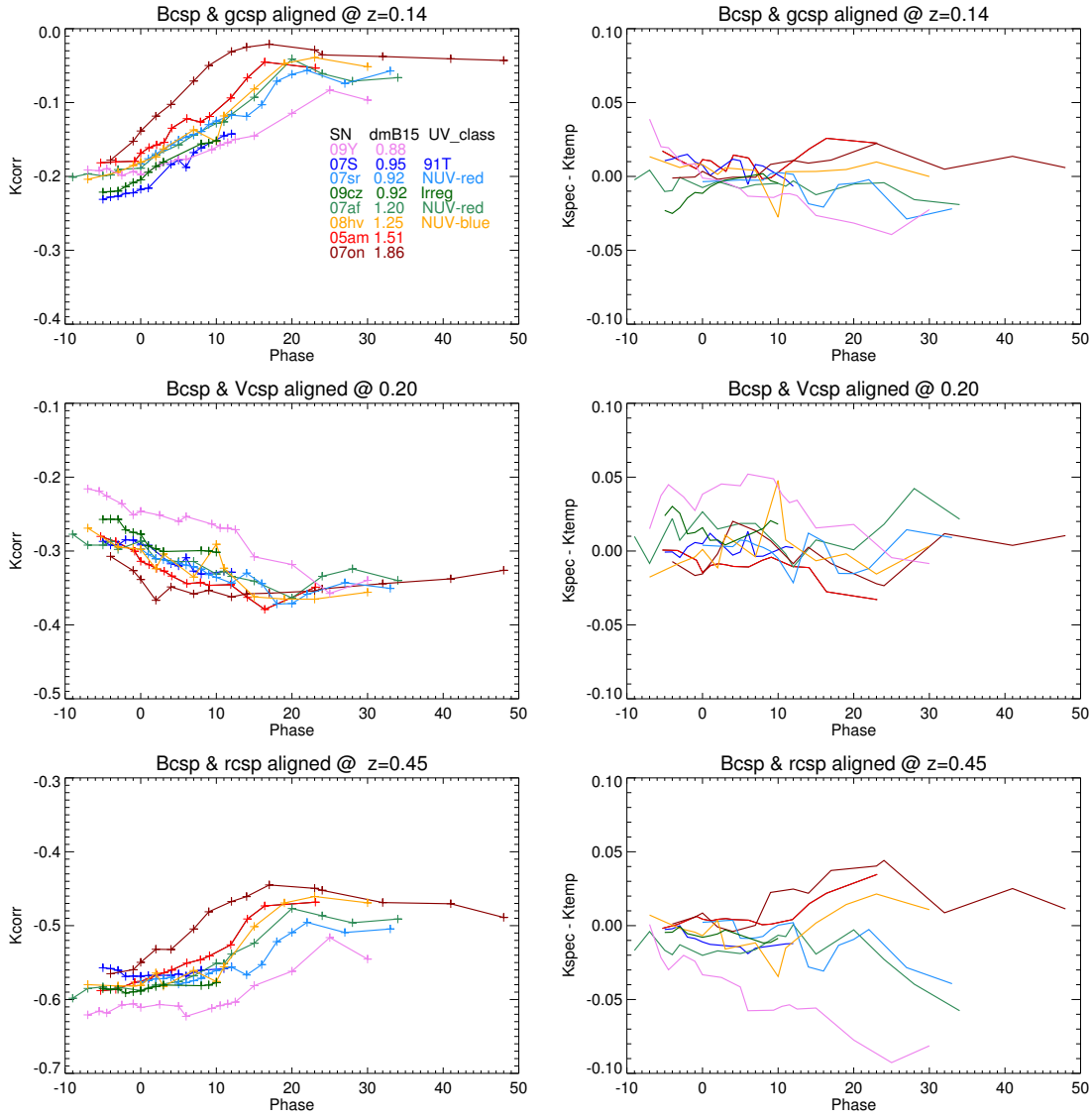

Figure 4.11: CSP B-band cross-band K-corrections vs phase.
Cross-band K-corrections for the rest-frame B_{CSP} filter and the observed-frame g_{CSP}, V_{CSP}, and r_{CSP} filters at redshifts which provide the best filter overlaps are plotted against the SNe phases relative to B-band maximum. The left column shows K-correction magnitudes calcualted using our bolometric SEDs. B-band decline rates for each SN are displayed using the color scheme outlined in the upper left panel. The right column shows the difference in K-correction values obtained when using our bolometric SEDs and template SEDs.

In Figure 4.12 we present the same B_{CSP} cross-band K-corrections as in Figure 4.11, now plotted against the SNe $(B-V)$ colors. The colors plotted are calculated from the synthetic magnitudes of the bolometric SEDs. Similar to the previous analysis, we again see that a systematic bias in the K-correction values can be traced to the $\Delta m_{15}(B)$ decline rate. Specifically, we see that the disagreement in K-correction magnitudes increase as the $\Delta m_{15}(B)$ values diverge from the mean value, and are generally smaller magnitudes at bluer colors and increase toward redder colors.

In Figures 4.13 - 4.15 we present cross-band K-corrections for the u_{CSP}, *UVW1*, and *UVM2* filters plotted against the SNe phases relative to B-band maximum. In these plots the layout and color schemes are same as the previous ones. In the u_{CSP} plots we see minimal evidence that $\Delta m_{15}(B)$ has a systematic effect on the differences in K-correction values as was found for the B_{CSP} band. For the *UVW1* and *UVM2* cases, we find no evidence for a $\Delta m_{15}(B)$ driven systematic effect. Additionally, we computed $\Delta m_{15}(UVM2)$, $\Delta m_{15}(UVW1)$, and $\Delta m_{15}(u_{CSP})$ values for each SN, and searched for trends in the K-correction residuals for each set of filters. This analysis provided no indication that the decline rates measured in each UV filter correlate with systematic SED differences.

We observe that the differences in K-correction values calculated by the bolometric and template SEDs increase from B_{CSP} to u_{CSP}, peak in the *UVW1* band, and then decrease in the *UVM2* band. At the epoch of B-band maximum light we measure the typical scatter in each band to be: $UVM2 = \pm 0.1$ mag, $UVW1 = \pm 0.2$ mag, $u_{CSP} = \pm 0.05$ mag, $B_{CSP} = \pm 0.04$ mag. The peak in the *UVW1* band coincides with the photometric observations of Brown et al. (2010) who found a greater scatter in (*UVM2* - *UVW1*) colors than the optical, and is slightly at odds with their observations of greater scattering of *UVM2* magnitudes than UVW1 magnitudes. Milne et al. (2013, 2015) later documented some order in these dispersions by noting

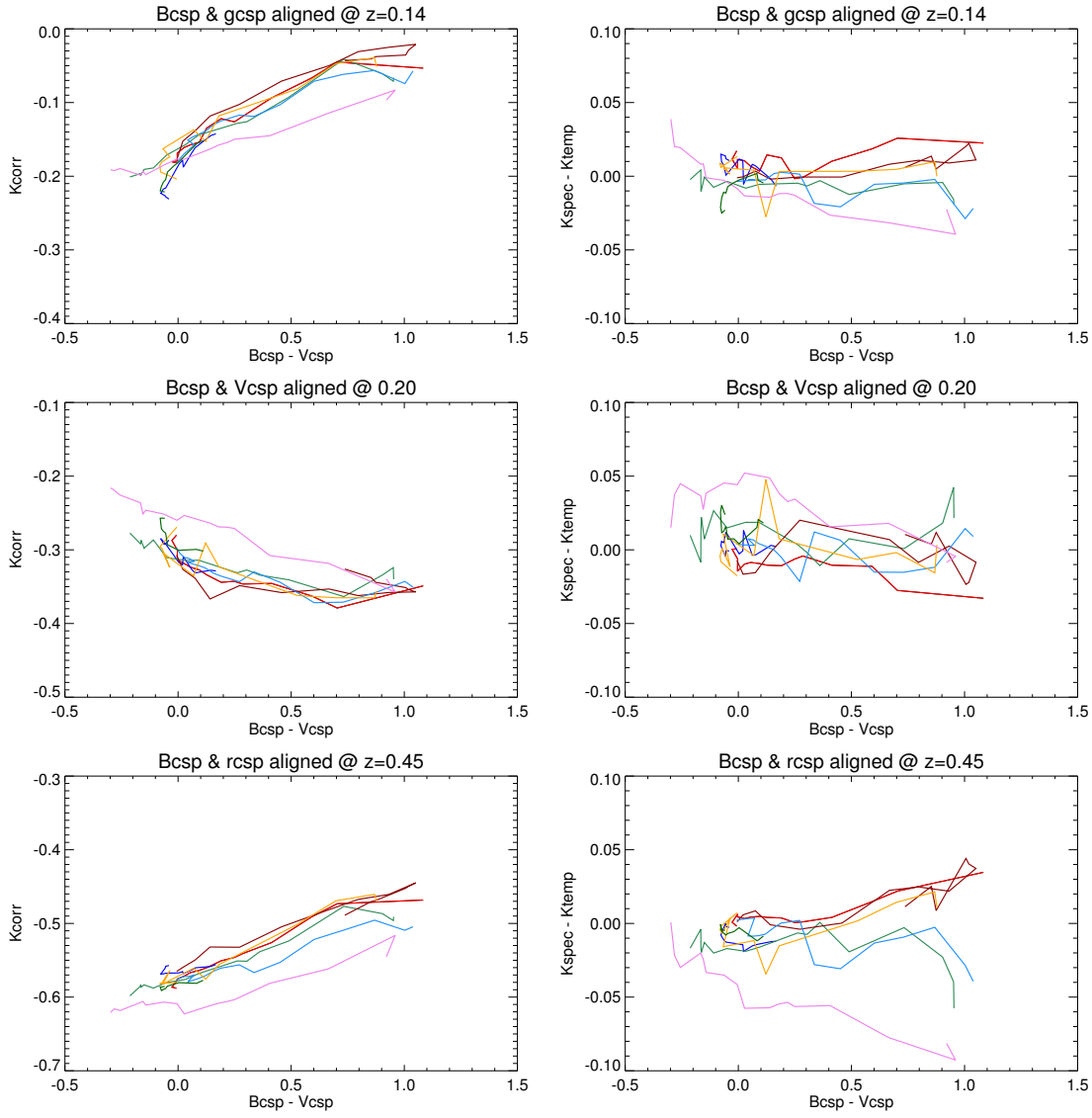

Figure 4.12: CSP B-band cross-band K-corrections vs (B-V) color. Cross-band K-corrections for the rest-frame B_{CSP} filter and the observed-frame g_{CSP}, V_{CSP}, and r_{CSP} filters at redshifts which provide the best filter overlaps are plotted against the SNe colors. The left column shows K-correction magnitudes calcualted using our bolometric SEDs. B-band decline rates for each SN are displayed using the color scheme outlined in the upper left panel. The right column shows the difference in K-correction values obtained when using our bolometric SEDs and template SEDs.

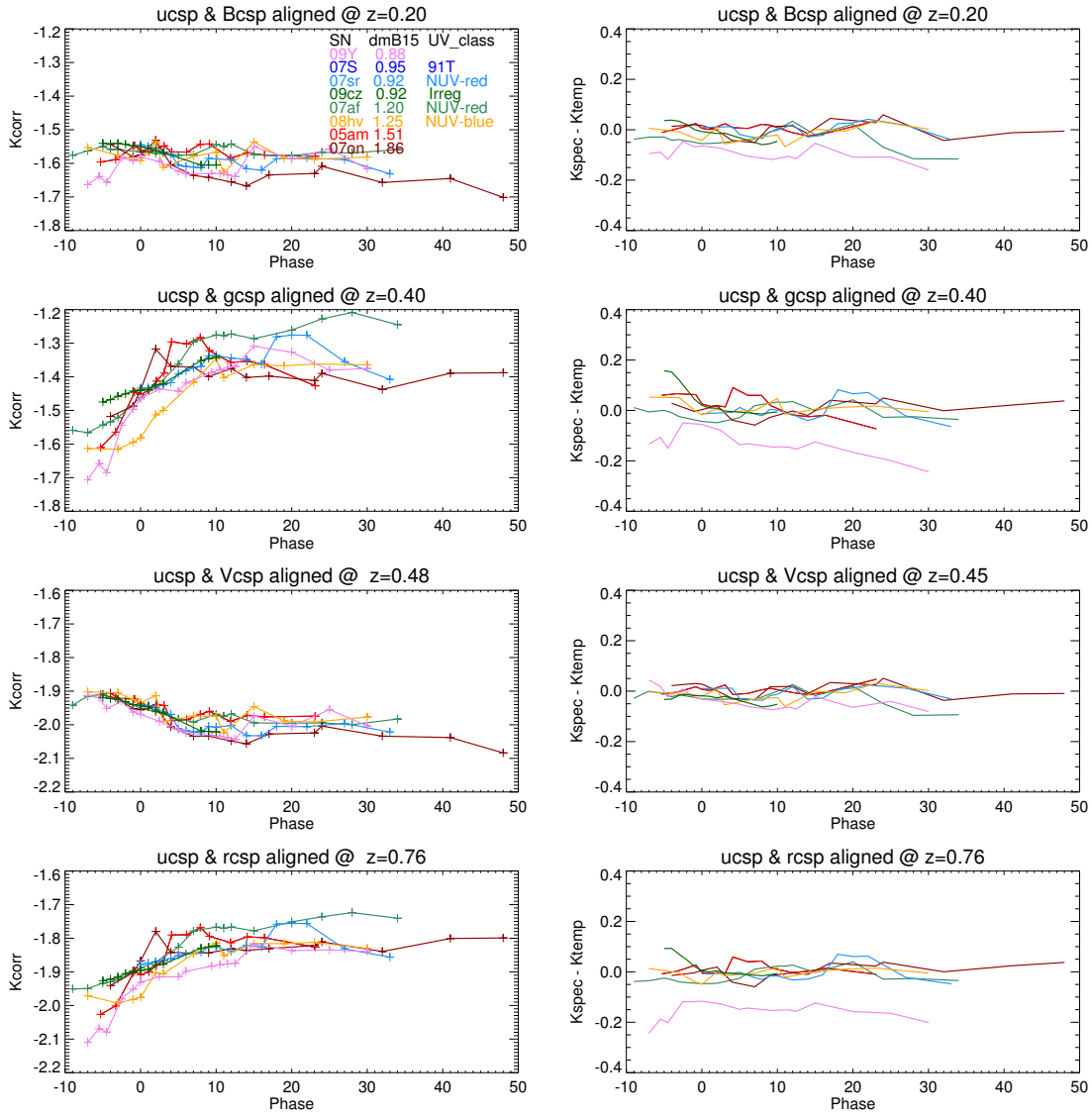

Figure 4.13: CSP u-band cross-band K-corrections vs phase.
Cross-band K-corrections for the u_{CSP} filter as functions of SN phase are shown in the left plots. The redshifts indicated were selected to provide the best overlap between the rest-frame u_{CSP} filter and the observer-frame filters. We calculated K-corrections using our bolometric SEDs and the templates of Hsiao et al. (2007); the difference between these K-corrections values as functions of SN phase are shown in the right plots.

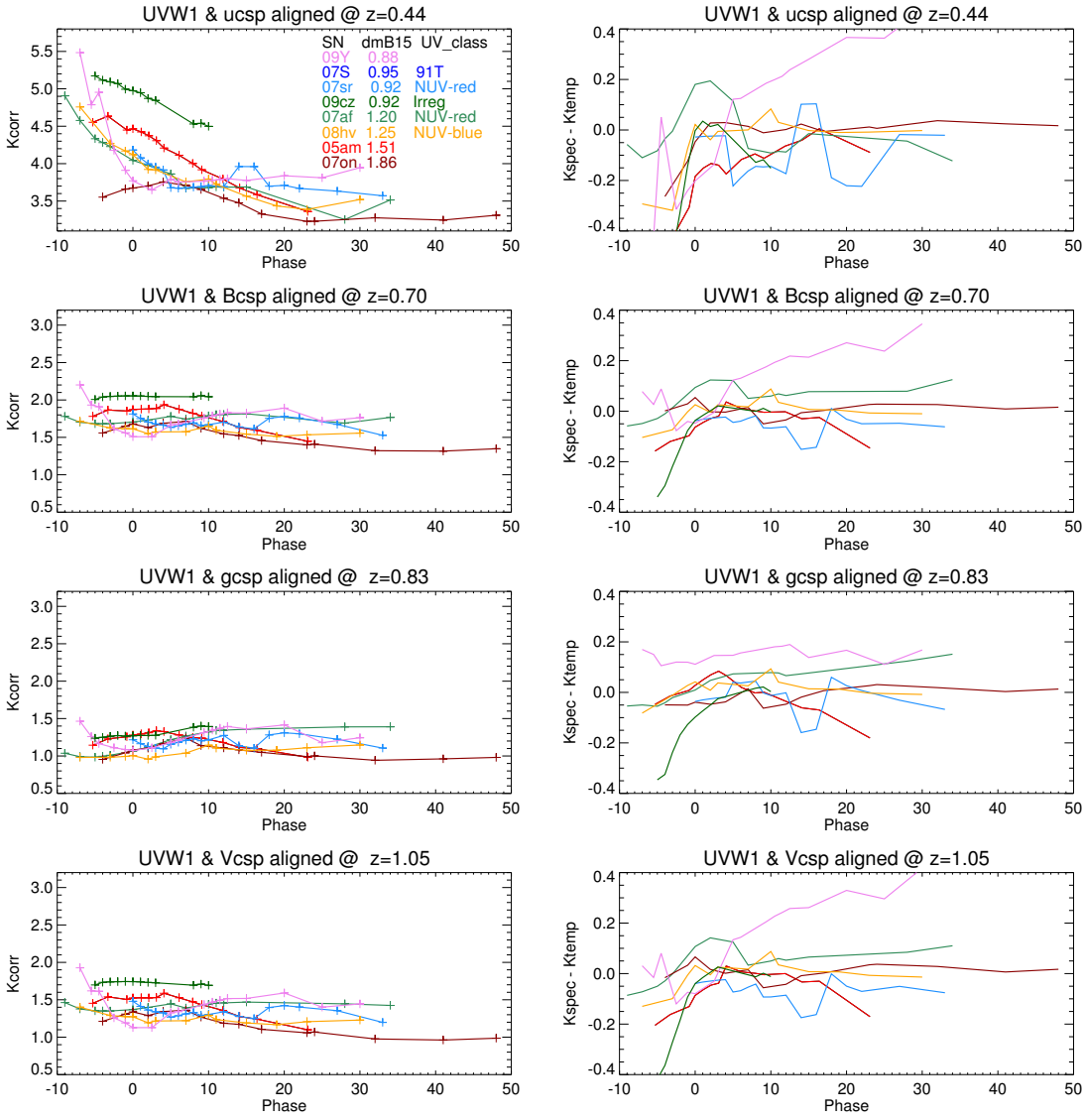

Figure 4.14: UVW1 cross-band K-corrections vs phase.
Cross-band K-corrections for the *Swift UVW1* filter as functions of SN phase are shown in the left plots. The redshifts indicated were selected to provide the best overlap between the rest-frame *UVW1* filter and the observer-frame filters. We calculated K-corrections using our bolometric SEDs and the templates of Hsiao et al. (2007); the difference between these K-corrections values as functions of SN phase are shown in the right plots.

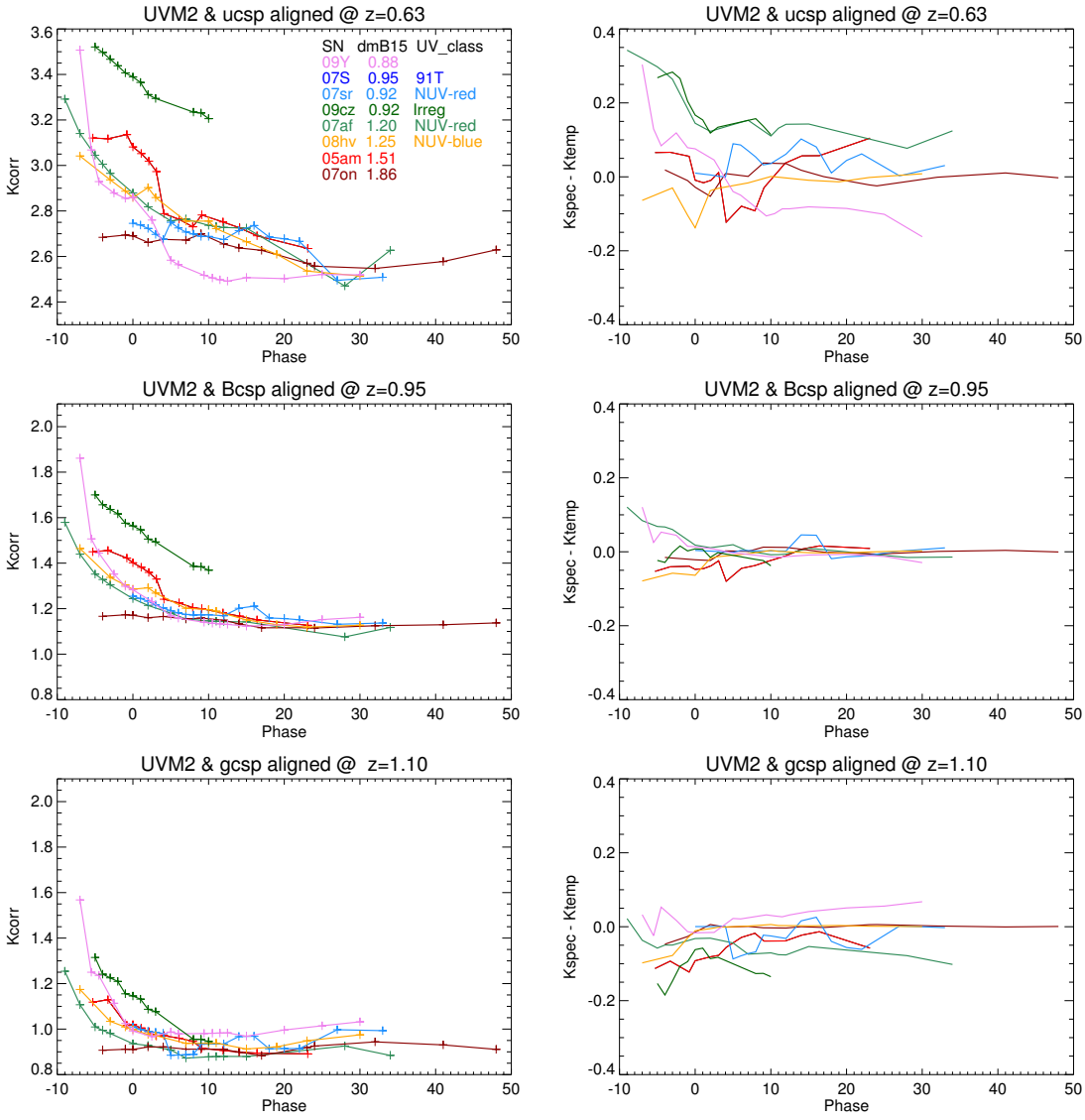

Figure 4.15: UVM2 cross-band K-corrections vs phase.
Cross-band K-corrections for the *Swift UVM2* filter as functions of SN phase are shown in the left plots. The redshifts indicated were selected to provide the best overlap between the rest-frame *UVM2* filter and the observer-frame filters. We calculated K-corrections using our bolometric SEDs and the templates of Hsiao et al. (2007); the difference between these K-corrections values as functions of SN phase are shown in the right plots.

that SNe Ia can be grouped photometrically into the categories Near-UV red (NUV red), Near-UV blue (NUV blue), Mid-UV blue (MUV blue) and irregular. Both of these observations are evidence for diverse feature structure among UV SEDs within the wavelength range $2300 - 3300$ Å. Our K-correction calculations trace the underlying spectroscopic diversity within this wavelength range, and provide an estimate of the K-correction accuracy we can expect in lieu direct spectral measurements. It is worth restating here that these calculations are done for the redshifts which provide the best overlap of rest-frame and observed-frame filters. Accordingly, one expects that non-optimal redshifts, which force the filters to sample slightly different regions of the source SED, will exacerbate differences between the resulting bolometric and template SED K-correction values.

Photometry of SNe in the rest-frame UV will be obtained in large numbers by current and future large surveys (DES, LSST, etc.) Our analysis has shown that a single set of time-evolving templates (Hsiao et al., 2007) does not capture the UV and blue-optical spectroscopic diversity of SNe Ia. Therefore, it is our recommendation that great care be taken when calculating K-corrections of these survey data. Continued analysis of the existing UV spectra sample and additional high quality spectral series observations will likely be very useful in generating a robust method of K-correcting rest-frame UV photometry in a way which accounts for time evolution as well as SED variations among SNe Ia UV subclassifications.

Reducing systematic errors in K-corrections will ultimately enable us to reduce systematic errors in the measurement of cosmological parameters. Amanullah et al. (2010) listed intrinsic color variations of SNe Ia as one of the three major sources of systematic error in the measurement of it w using SNe Ia. Our analysis has quantifed the systematic effect of SED variations on the K-corrections which are computed in making these measurements and provides a set of UV-O-IR SEDs to reduce this

effect. Additionally, as stated by Milne et al. (2013), the categorization of SNe based on NUV-optical colors lowers the scatter in $(U_{sw} - V_{sw})$ and $(UVW1 - V_{sw})$ to a level comparable to $(B - V)$. This finding gives hope that it may be possible to extend the cosmological utility of SNe Ia into the NUV. Achieving this will require knowledge of the spectroscopic differences responsible for the color differences so that K-corrections can be calculated with confidence and minimal systematic error. Our analysis, and those of Milne et al. (2013, 2015), have begun to probe the underlying spectroscopic differences and physical origins of these events. Our identification of a possible set of regular spectroscopic features responsible for the NUV dichotomy is potentially another step toward the utilization of the NUV as a cosmological tool.

4.12 Flux Ratios and Bolometric Corrections

The majority of SNe Ia observations are made within the wavelength ranges of ground-based optical filters, typically *UBVRI* or *ugriz*. This is the case due to the relative ease of obtaining data within these wavelength ranges. For these data sets with optical only observations, it is sometimes desirable to estimate UV-O-IR fluxes by calculating bolometric corrections to account for the UV and NIR fluxes which remain unmeasured. Among differing studies, bolometric corrections are calculated using differing techniques, assumptions and wavelength ranges (Stritzinger & Leibundgut, 2005; Wang et al., 2009; Taubenberger et al., 2011; Sasdelli et al., 2014; Zhang et al., 2016). This is disadvantageous because it complicates the comparison of bolometric data sets from differing sources and introduces systematic errors.

Our UV-O-IR data set is useful for expanding the utility of data sets without full UV-O-IR observations and those without UV spectral observations by enabling the calculation of bolometric corrections of SNe Ia which take into account realistic UV and NIR evolutionary trends. We present an example case in which we calculate

bolometric corrections for a data set comprised of typical ground-based *UBVRI* or *ugri* observations covering 3200 − 9000Å. In practice, we recommend that these calculations be customized to accurately reflect the wavelength coverage of a given data set. For this example, we define the UV to be the total integrated flux of an SED within the wavelength range 1600 − 3200Å, the optical within the range 3200 − 9000Å, the NIR within the range 9000 − 25000Å, and 'bolometric' within the range 1600 − 25000Å. In Figures 4.16 - 4.19 we present the relative contributions of each of these wavelength regimes to the total bolometric flux as functions of SNe phase relative to B-band maximum brightness.

In Figure 4.16 we observe the UV fraction to evolve with time from $\sim 10 \pm 5\%$ near peak brightness to $\sim 3 \pm 2\%$ at $+20$ days. We stress that the UV fraction is shown to evolve with SN phase and strongly suggest that bolometric corrections take this into account. We observe that the NUV-blue SN 2008hv (Milne et al., 2013) consistently has a greater UV fraction than all the other SNe. With the exception of SN 2008hv, we observe weak evidence of a trend in which SNe with faster B-band decline rates exhibit lower UV fractions at epochs prior to $+20$ days and then evolve to convergence around $+20$ days. We stress that classification as NUV-blue appears to not be a part of this trend. We note that at the earliest epochs for which we have data, the 1991T-like SN 2007S appears that it may not be a part of the leveling-off trend exhibited by the other SNe in the sample. This suggests a greater UV fraction earlier than -5 days as demonstrated by Smitka et al. (2015) for a 1999aa-like object.

In Figure 4.17 we observe a scatter of $\sim 5\%$ in the optical fraction near maximum light and an increase in the scatter at later epochs. We observe the peak optical fraction to correlate with B-band decline rate, where fast declining SNe peak earlier than slow declining SNe. For epochs between 15 and 25 days we observe a correlation between the B-band decline rate and the optical fraction. For the phase of $+20$ days

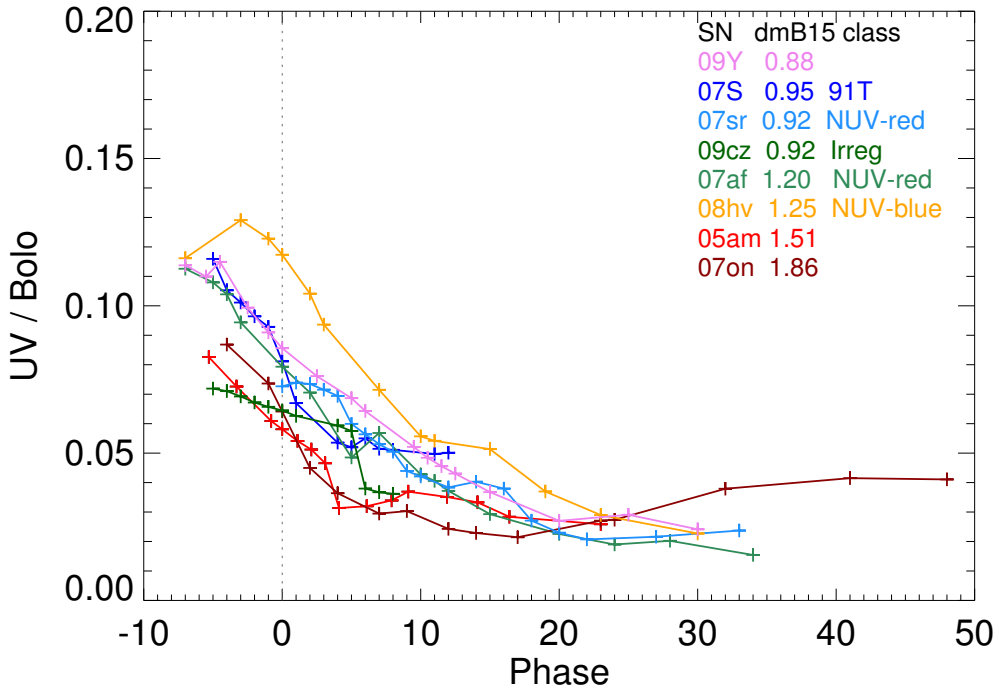

Figure 4.16: UV / bolo vs phase.
The relative contribution of the UV to the total bolometric flux as a function of SN phase relative to B-band maximum. We observe that the UV fraction evolves with time and a $\sim 5\%$ scatter in the UV fraction at epochs prior to $+20$ days. We observe that the NUV-blue SN 2008hv consistently has a greater fraction of UV flux than other SNe. We observe weak evidence that faster B-band decline rate corresponds to less UV flux at epochs prior to $+20$ days, and warn that classification as NUV-blue defies this trend.

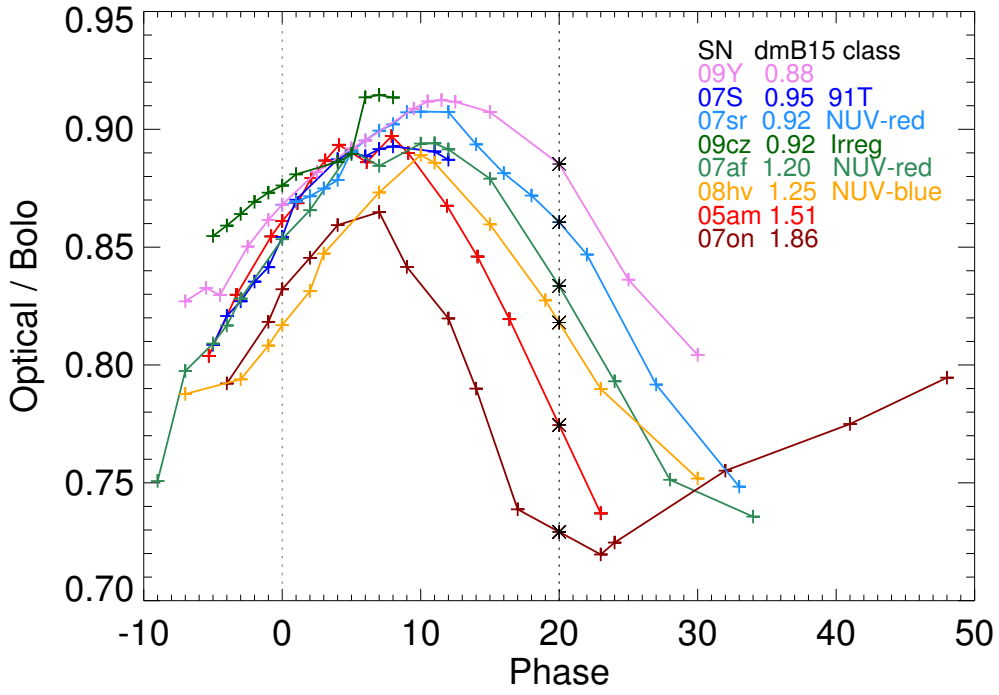

Figure 4.17: Optical / bolo vs phase.
The relative contribution of the optical to the total bolometric flux as a function of SN phase relative to B-band maximum. We observe the peak optical fraction to occur earlier for faster declining SNe Ia. Near B-band maximum light we observe the scatter in optical fraction to be $\sim 5\%$ and increase thereafter. At 20 days post-maximum we observe a relationship between B-band decline rate and optical fraction.

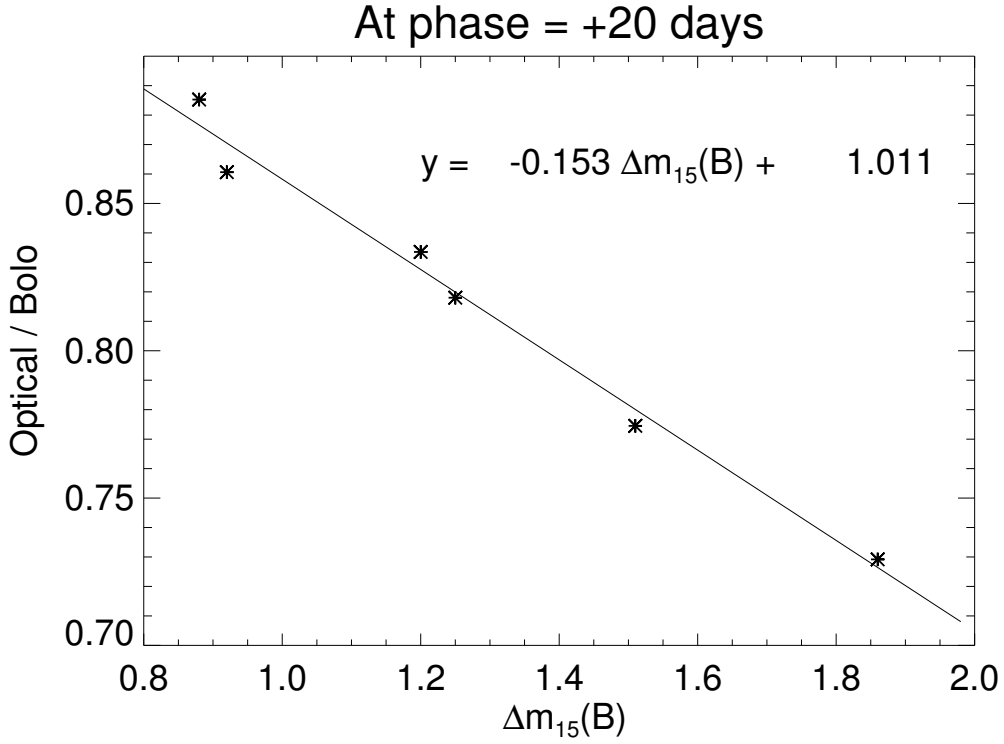

Figure 4.18: Optical / bolo vs $\Delta m_{15}(B)$ at +20 days.
The contribution of the optical to the total bolometric fluxes at a phase of +20 days plotted as a function of B-band decline rate. A linear fit to the data is shown by the straight line.

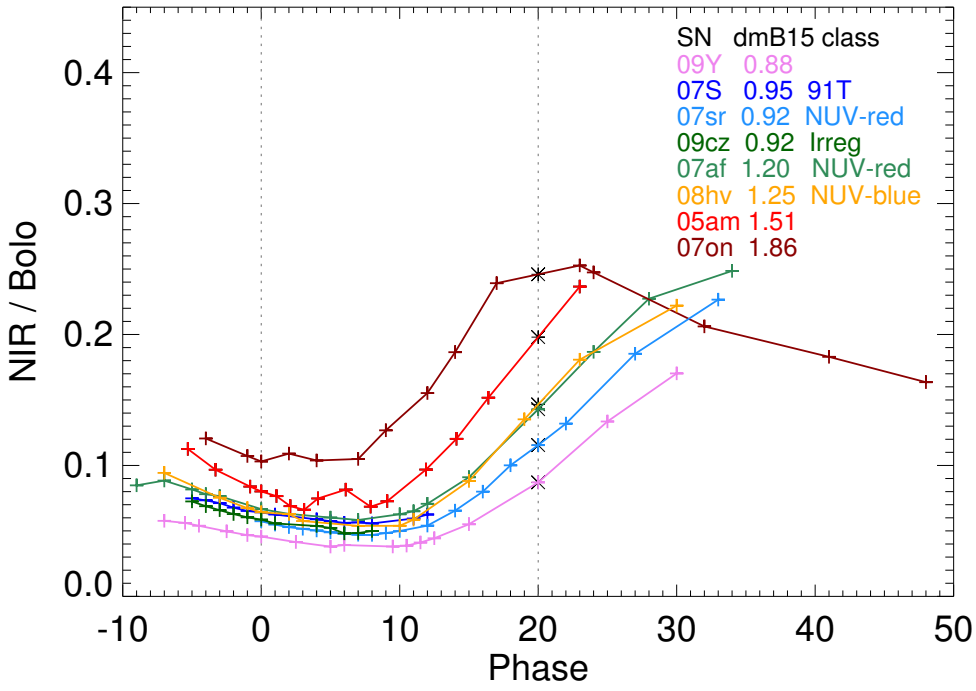

Figure 4.19: NIR / bolo vs phase.
The relative contribution of the NIR to the total bolometric flux as a function of SN phase relative to B-band maximum. At all epochs for which we have data, we observe a strong dependence of the NIR fraction on the B-band decline rate.

we interpolated the optical fraction value for each SN; Figure 4.18 plots these values against the B-band decline rate. We find a linear relationship between the optical fraction and the B-band decline rate. This observation suggests that it may be possible to accurately estimate bolometric fluxes at epochs between +15 and +25 days using only optical data.

In Figure 4.19 we present the NIR contribution to the bolometric flux for the eight SNe Ia in our sample. We observe a scatter in the NIR fraction of $\sim$ 10% near maximum brightness and an increase thereafter. We observe a strong trend in which SNe Ia B-band decline rate is proportional to the NIR proportional flux. This trend is very distinctly present between -5 and $+30$ days. Similar to the optical, for the phases of 0 and $+20$ days we interpolated the NIR fraction value for each SN; Figures 4.20 and 4.21 plot these values against the B-band decline rate.

In Figures 4.22 and 4.23 we present bolometric corrections for photometric observations made using differing combinations of filters within the *UBVRI* and *ugri* systems. The curves presented were calculated by integrating the UV-O-IR SEDs within the wavelength ranges sampled by the filters indicated in each plot. Table 4.12 gives the exact wavelength ranges within which integrations were performed.

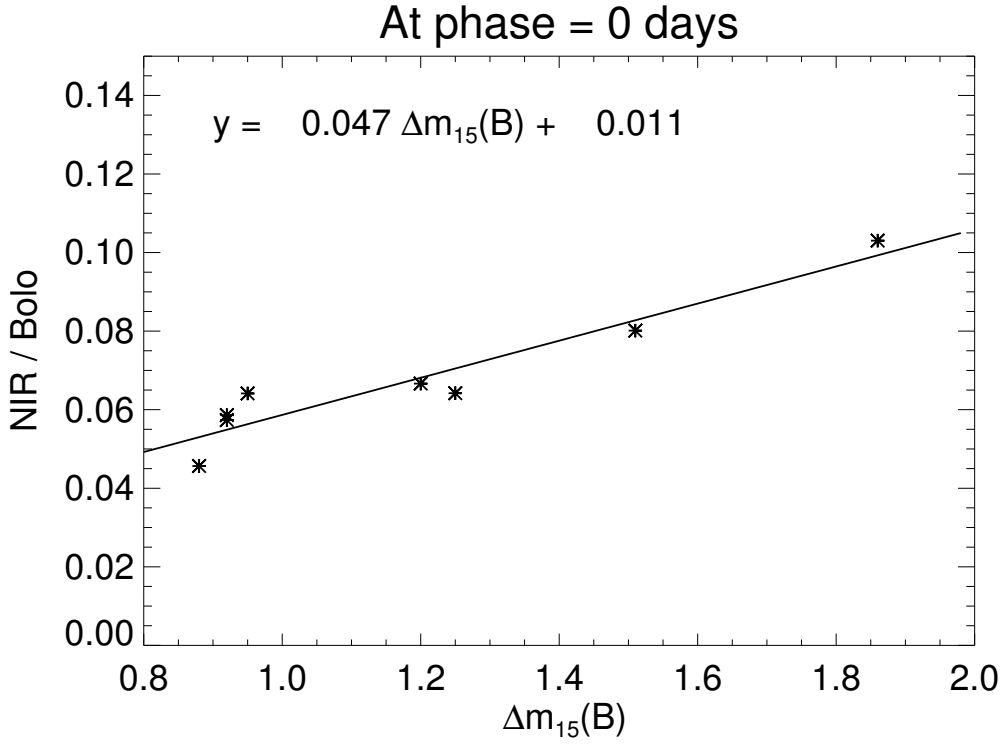

Figure 4.20: NIR / bolo vs $\Delta m_{15}(B)$ at 0 days.
The contribution of the NIR to the total bolometric fluxes at a phase of 0 days plotted as a function of B-band decline rate. A linear fit to the data is shown by the straight line.

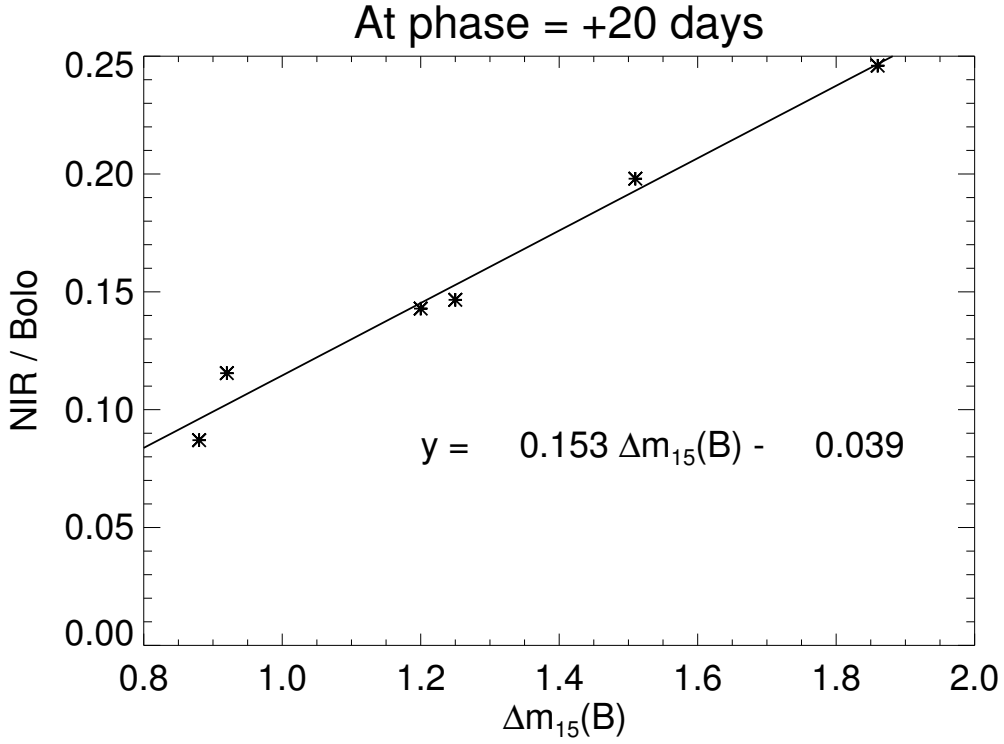

Figure 4.21: NIR / bolo vs $\Delta m_{15}(B)$ at +20 days.
The contribution of the NIR to the total bolometric fluxes at a phase of +20 days plotted as a function of B-band decline rate. A linear fit to the data is shown by the straight line.

Table 4.12: Bolometric correction wavelength ranges.
We present the wavelength ranges within which integrations were performed in the calculation of bolometric correction values.

Filters	Minimum Wavelength (Å)	Maximum Wavelength (Å)
$UBVRI$	3200	9000
$BVRI$	4000	9000
BVR	4000	7000
BV	4000	6000
V	5000	6000
$ugri$	3400	8300
ugr	3400	6800
gr	4000	6800
g	4000	5500

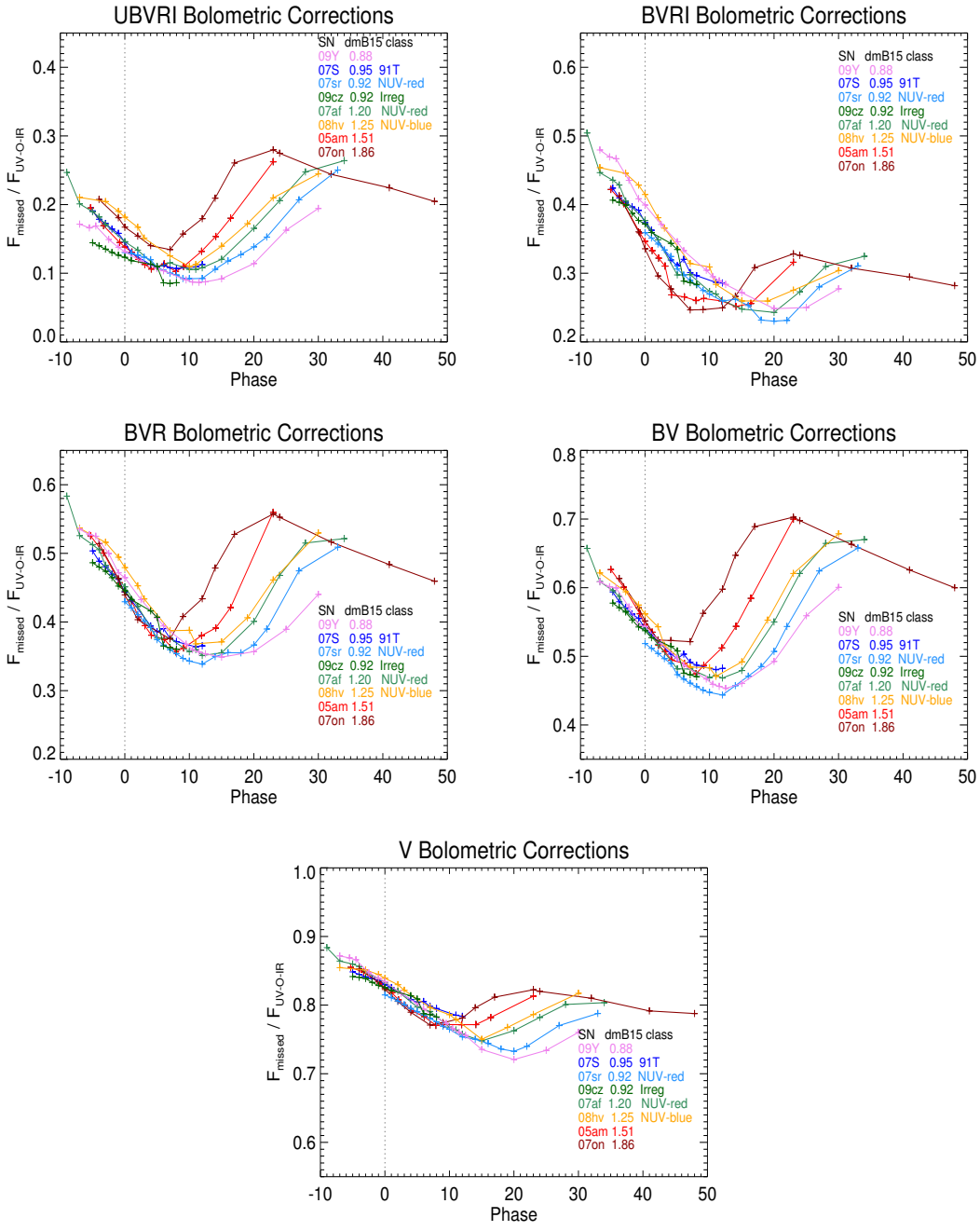

Figure 4.22: The UBVRI system bolometric corrections.
The fractional missed UV-O-IR flux for photometry measured using different combinations of the UBVRI filters as functions of SN phase.

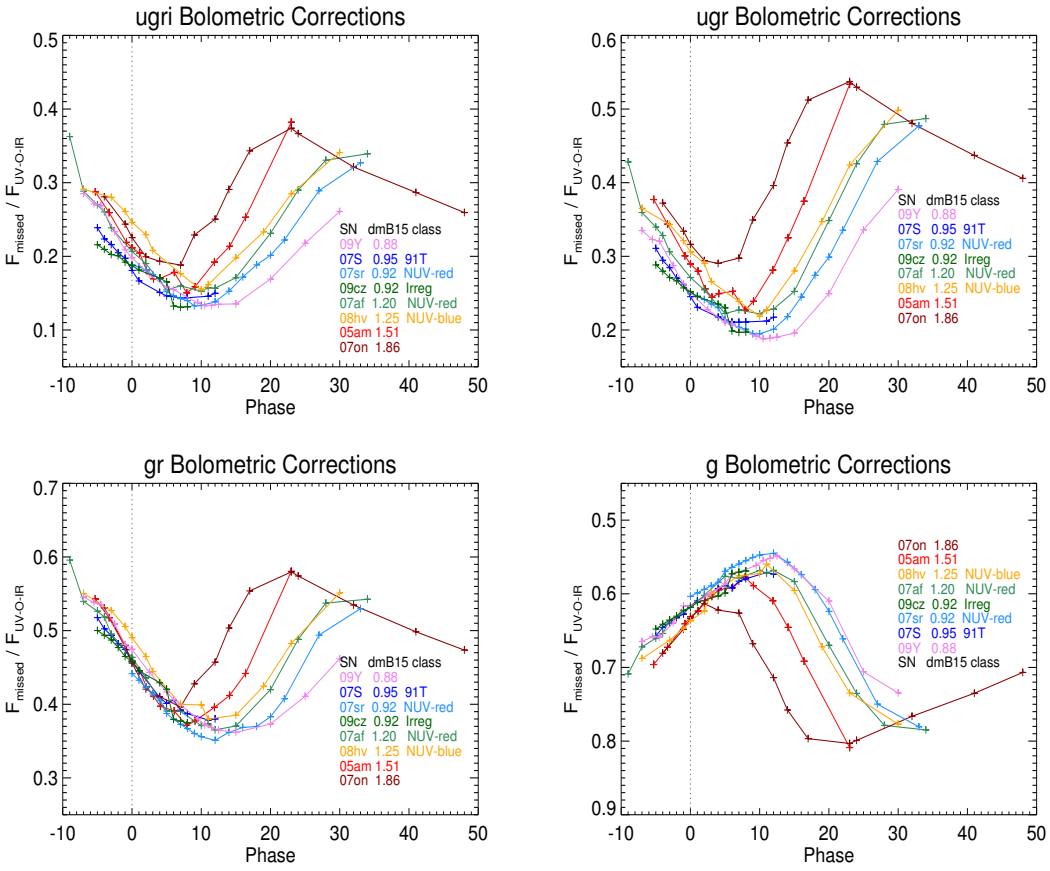

Figure 4.23: The ugri system bolometric corrections.
The fractional missed UV-O-IR flux for photometry measured using different combinations of the CSP versions of the ugri filters as functions of SN phase.

5. SUMMARY

We have presented an ultraviolet (UV) spectroscopic atlas containing 91 spectra of 22 unique Type Ia supernovae (SNe Ia). The spectra were observed using the Ultraviolet/Optical Telescope (UVOT) onboard the *Swift* space telescope. We presented a new technique of decontaminating UVOT grism spectra, which we applied to 40 of the spectra in our sample. We presented the first UV spectroscopic series of a peculiar 1999aa-like SN Ia, iPTF14bdn, and compared to normal SNe in our sample. We found this SN to have very blue UV colors at early times caused by a bright feature between $2800 - 3200$Å. We attributed this to a lower UV opacity caused by higher temperatures above the SN photosphere, likely due to a greater quantity of ^{56}Ni in this region. We also identified the spectroscopic feature differences between $2700 - 3300$Å responsible for the near-UV (NUV) photometric diversity. Comparison of these features to model data suggested that NUV-bluer SNe result from lower metal abundances in the outer ejecta layers.

We combined our UV spectral atlas with UV, optical and NIR photometry, and spectra to generate a UV-O-IR spectral series atlas for 8 SNe Ia near peak brightness. The UV-O-IR SEDs represent time evolution within -10 to $+30$ days of peak brightness, decline rates between $0.9 < \Delta m_{15}(B) < 1.8$, and UV subclassification (when known). Using these data, we calculated integrated bolometric luminosities and synthesized ^{56}Ni masses. We demonstrated that our UV-O-IR SEDs provide an improved method of calculating K-corrections for B-band optical photometry, and presented an analysis of SNe Ia UV K-corrections. We presented a method of calculating bolometric corrections which take the SNe decline rates into account for SNe near peak brightness.

REFERENCES

Adelman-McCarthy, J. K., Agüeros, M. A., Allam, S. S., et al. 2007, ApJS, 172, 634

Amanullah, R., Lidman, C., Rubin, D., et al. 2010, ApJ, 716, 712

Arnett, W. D. 1982, ApJ, 253, 785

Arnett, W. D., Branch, D., & Wheeler, J. C. 1985, Nature, 314, 337

Arp, H. 1961, ApJ, 133, 869

Ashall, C., Mazzali, P., Bersier, D., et al. 2014, MNRAS, 445, 4427

Bayless, A. J., Pritchard, T. A., Roming, P. W. A., et al. 2013, ApJL, 764, L13

Bernstein, J. P., Kessler, R., Kuhlmann, S., et al. 2012, ApJ, 753, 152

Bessell, M. S. 1990, Publications of the Astronomical Society of the Pacific, 102, 1181

Bevington, P., & Robinson, D. 2003, Data reduction and error analysis for the physical sciences, McGraw-Hill Higher Education (McGraw-Hill)

Blondin, S., Matheson, T., Kirshner, R. P., et al. 2012, AJ, 143, 126

Bohlin, R. C., & Gilliland, R. L. 2004a, AJ, 128, 3053

—. 2004b, AJ, 127, 3508

Bostroem, K. A., & Proffitt, C. 2011, STIS Data Handbook v. 6.0 (Space Telescope Institute)

Branch, D., Baron, E., Thomas, R. C., et al. 2004, PASP, 116, 903

Breeveld, A. A., Landsman, W., Holland, S. T., et al. 2011, in American Institute of Physics Conference Series, Vol. 1358, American Institute of Physics Conference Series, ed. J. E. McEnery, J. L. Racusin, & N. Gehrels, 373–376

Brown, P. J. 2014, ApJL, 796, L18

Brown, P. J., Breeveld, A. A., Holland, S., Kuin, P., & Pritchard, T. 2014a, Ap&SS,

354, 89

Brown, P. J., Dawson, K. S., Harris, D. W., et al. 2012a, ApJ, 749, 18

Brown, P. J., Roming, P. W. A., Milne, P., et al. 2010, ApJ, 721, 1608

Brown, P. J., Dawson, K. S., de Pasquale, M., et al. 2012b, ApJ, 753, 22

Brown, P. J., Smitka, M. T., Wang, L., et al. 2014b, ArXiv e-prints, arXiv:1408.2381

Brown, P. J., Kuin, P., Scalzo, R., et al. 2014c, ApJ, 787, 29

Brown, P. J., Smitka, M. T., Wang, L., et al. 2015a, ApJ, 805, 74

—. 2015b, ApJ, 805, 74

Bufano, F., Immler, S., Turatto, M., et al. 2009, ApJ, 700, 1456

Burns, C. R., Stritzinger, M., Phillips, M. M., et al. 2011, AJ, 141, 19

—. 2014, ApJ, 789, 32

Cao, Y., Perley, D., Kasliwal, M., et al. 2014, The Astronomer's Telegram, 6175, 1

Cao, Y., Kulkarni, S. R., Howell, D. A., et al. 2015, Nature, 521, 328

Childress, M. J., Filippenko, A. V., Ganeshalingam, M., & Schmidt, B. P. 2014, MNRAS, 437, 338

Childress, M. J., Scalzo, R. A., Sim, S. A., et al. 2013, ApJ, 770, 29

Cohen, M., Walker, R. G., Carter, B., et al. 1999, AJ, 117, 1864

Colina, L., & Bohlin, R. C. 1994, AJ, 108, 1931

Contreras, C., Hamuy, M., Phillips, M. M., et al. 2010, AJ, 139, 519

Filippenko, A. V., Richmond, M. W., Matheson, T., et al. 1992a, ApJL, 384, L15

Filippenko, A. V., Richmond, M. W., Branch, D., et al. 1992b, AJ, 104, 1543

Fisher, A., Branch, D., Nugent, P., & Baron, E. 1997, ApJL, 481, L89

Fitzpatrick, E. L. 1999, PASP, 111, 63

Folatelli, G., Morrell, N., Phillips, M. M., et al. 2013, ApJ, 773, 53

Foley, R. J., Filippenko, A. V., & Jha, S. W. 2008, ApJ, 686, 117

Foley, R. J., & Kirshner, R. P. 2013, ApJL, 769, L1

Foley, R. J., Matheson, T., Blondin, S., et al. 2009, AJ, 137, 3731

Foley, R. J., Challis, P. J., Filippenko, A. V., et al. 2012a, ApJ, 744, 38

Foley, R. J., Kromer, M., Howie Marion, G., et al. 2012b, ApJL, 753, L5

Foley, R. J., Filippenko, A. V., Kessler, R., et al. 2012c, The Astronomical Journal, 143, 113

Foley, R. J., Fox, O. D., McCully, C., et al. 2014, MNRAS, 443, 2887

Freedman, W. L., Madore, B. F., Gibson, B. K., et al. 2001, ApJ, 553, 47

Fukugita, M., Ichikawa, T., Gunn, J. E., et al. 1996, AJ, 111, 1748

Garavini, G., Folatelli, G., Goobar, A., et al. 2004, AJ, 128, 387

Gehrels, N., Chincarini, G., Giommi, P., et al. 2004, ApJ, 611, 1005

Gutiérrez, C. P., González-Gaitán, S., Folatelli, G., et al. 2016, A&A, 590, A5

Hamuy, M., Phillips, M. M., Suntzeff, N. B., et al. 1996, AJ, 112, 2398

Hamuy, M., Folatelli, G., Morrell, N. I., et al. 2006, PASP, 118, 2

Hicken, M., Wood-Vasey, W. M., Blondin, S., et al. 2009, ApJ, 700, 1097

Hoeflich, P., Khokhlov, A. M., & Wheeler, J. C. 1995, ApJ, 444, 831

Hoeflich, P., Mueller, E., & Khokhlov, A. 1993, A&A, 268, 570

Höflich, P., Wheeler, J. C., & Thielemann, F. K. 1998, ApJ, 495, 617

Hogg, D. W., Baldry, I. K., Blanton, M. R., & Eisenstein, D. J. 2002, ArXiv Astrophysics e-prints, astro-ph/0210394

Howell, D. A., Sullivan, M., Nugent, P. E., et al. 2006, Nature, 443, 308

Hsiao, E. Y., Conley, A., Howell, D. A., et al. 2007, ApJ, 663, 1187

Hubble, E., & Humason, M. L. 1931, Contributions from the Mount Wilson Observatory / Carnegie Institution of Washington, 427, 1

Humason, M. L., Mayall, N. U., & Sandage, A. R. 1956, AJ, 61, 97

Jack, D., Baron, E., & Hauschildt, P. H. 2015, ArXiv e-prints, arXiv:1503.03088

Jeffery, D. J. 1989, ApJS, 71, 951

Jeffery, D. J., Leibundgut, B., Kirshner, R. P., et al. 1992, ApJ, 397, 304

Jensen, J. B., Blakeslee, J. P., Gibson, Z., et al. 2015, ApJ, 808, 91

Jha, S. 2002, PhD thesis, Harvard University

Jha, S., Branch, D., Chornock, R., et al. 2006a, AJ, 132, 189

Jha, S., Kirshner, R. P., Challis, P., et al. 2006b, AJ, 131, 527

Kasen, D. 2006, ApJ, 649, 939

—. 2010, ApJ, 708, 1025

Kim, A., Goobar, A., & Perlmutter, S. 1996, PASP, 108, 190

Kirshner, R. P., Jeffery, D. J., Leibundgut, B., et al. 1993, ApJ, 415, 589

Kowalski, M., Rubin, D., Aldering, G., et al. 2008, ApJ, 686, 749

Kuin, N. P. M., & Rosen, S. R. 2008, MNRAS, 383, 383

Kuin, N. P. M., Landsman, W., Page, M. J., et al. 2009, MNRAS, 395, L21

Kuin, N. P. M., Landsman, W., Breeveld, A. A., et al. 2015, MNRAS, 449, 2514

Kuin, P. 2014, UVOTPY: Swift UVOT grism data reduction, Astrophysics Source Code Library, ascl:1410.004

Landolt, A. U. 1992, AJ, 104, 340

Larsen, S. S., Walsh, J., & Kummel, M. 2006, Wavelength and Flux Calibration of the ACS/HRC PR200L Prism, Tech. rep.

Law, N. M., Kulkarni, S. R., Dekany, R. G., et al. 2009, PASP, 121, 1395

Lentz, E. J., Baron, E., Branch, D., & Hauschildt, P. H. 2001, ApJ, 557, 266

Li, W., Filippenko, A. V., Chornock, R., et al. 2003, PASP, 115, 453

Lira, P., Suntzeff, N. B., Phillips, M. M., et al. 1998, AJ, 115, 234

LSST Science Collaboration, Abell, P. A., Allison, J., et al. 2009, ArXiv e-prints, arXiv:0912.0201

Maguire, K., Sullivan, M., Pan, Y.-C., et al. 2014, MNRAS, 444, 3258

Margutti, R., Milisavljevic, D., Soderberg, A. M., et al. 2014, ApJ, 780, 21

Marion, G. H., Sand, D. J., Hsiao, E. Y., et al. 2015, ApJ, 798, 39

Mazzali, P. A. 2000, A&A, 363, 705

Mazzali, P. A., Danziger, I. J., & Turatto, M. 1995, A&A, 297, 509

Mazzali, P. A., Sullivan, M., Hachinger, S., et al. 2014, MNRAS, 439, 1959

Miknaitis, G., Pignata, G., Rest, A., et al. 2007, ApJ, 666, 674

Milne, P. A., Brown, P. J., Roming, P. W. A., Bufano, F., & Gehrels, N. 2013, ApJ, 779, 23

Milne, P. A., Foley, R. J., Brown, P. J., & Narayan, G. 2015, ApJ, 803, 20

Milne, P. A., Brown, P. J., Roming, P. W. A., et al. 2010, ApJ, 721, 1627

Mould, J. R., Huchra, J. P., Freedman, W. L., et al. 2000, ApJ, 529, 786

Munari, U., Henden, A., Belligoli, R., et al. 2013, NewA, 20, 30

Nugent, P., Kim, A., & Perlmutter, S. 2002, PASP, 114, 803

Nugent, P. E., Sullivan, M., Cenko, S. B., et al. 2011, Nature, 480, 344

Oke, J. B., & Sandage, A. 1968, ApJ, 154, 21

Pereira, R., Thomas, R. C., Aldering, G., et al. 2013, A&A, 554, A27

Perlmutter, S., Gabi, S., Goldhaber, G., et al. 1997, ApJ, 483, 565

Perlmutter, S., Aldering, G., Goldhaber, G., et al. 1999, ApJ, 517, 565

Phillips, M. M. 1993, ApJL, 413, L105

Phillips, M. M., Wells, L. A., Suntzeff, N. B., et al. 1992, AJ, 103, 1632

Pickles, A. J. 1998, PASP, 110, 863

Poole, T. S., Breeveld, A. A., Page, M. J., et al. 2008, MNRAS, 383, 627

Pskovskii, I. P. 1977, Soviet Ast., 21, 675

Pskovskii, Y. P. 1984, Soviet Ast., 28, 658

Rheault, J.-P., DePoy, D. L., Behm, T. W., et al. 2010, in Proc. SPIE, Vol. 7735, Ground-based and Airborne Instrumentation for Astronomy III, 773564

Rheault, J.-P., Mondrik, N. P., DePoy, D. L., Marshall, J. L., & Suntzeff, N. B.

2014, in Proc. SPIE, Vol. 9147, Ground-based and Airborne Instrumentation for Astronomy V, 91475L

Riess, A. G., Filippenko, A. V., Challis, P., et al. 1998, AJ, 116, 1009

Riess, A. G., Macri, L., Casertano, S., et al. 2011, ApJ, 730, 119

Riess, A. G., Macri, L. M., Hoffmann, S. L., et al. 2016, ArXiv e-prints, arXiv:1604.01424

Roming, P. W. A., Kennedy, T. E., Mason, K. O., et al. 2005, Space Science Reviews, 120, 95

Sahu, D. K., & Arora, S. 2011, Central Bureau Electronic Telegrams, 2669, 2

Sandage, A. 1956, The Red-shift (Freeman)

Sasdelli, M., Mazzali, P. A., Pian, E., et al. 2014, MNRAS, 445, 711

Schlafly, E. F., & Finkbeiner, D. P. 2011, ApJ, 737, 103

Schlegel, D. J., Finkbeiner, D. P., & Davis, M. 1998, ApJ, 500, 525

Schmidt, B. P., Suntzeff, N. B., Phillips, M. M., et al. 1998, ApJ, 507, 46

Silverman, J. M., Ganeshalingam, M., Li, W., et al. 2011, Monthly Notices of the Royal Astronomical Society, 410, 585

Silverman, J. M., Foley, R. J., Filippenko, A. V., et al. 2012a, MNRAS, 425, 1789

Silverman, J. M., Ganeshalingam, M., Cenko, S. B., et al. 2012b, ApJL, 756, L7

Smith, J. A., Tucker, D. L., Kent, S., et al. 2002, AJ, 123, 2121

Smitka, M. T., Brown, P. J., Kuin, P., & Suntzeff, N. B. 2016, Publications of the Astronomical Society of the Pacific, 128, 034501

Smitka, M. T., Brown, P. J., Suntzeff, N. B., et al. 2015, ApJ, 813, 30

Sobolev, V. V. 1960, Moving envelopes of stars (Cambridge: Harvard University Press)

Straizys, V. 1996, Baltic Astronomy, 5, 459

Stritzinger, M., & Leibundgut, B. 2005, A&A, 431, 423

Stritzinger, M., Hamuy, M., Suntzeff, N. B., et al. 2002, AJ, 124, 2100

Stritzinger, M. D., Phillips, M. M., Boldt, L. N., et al. 2011, AJ, 142, 156

Strömgren, B. 1937, ApJ, 86, 1

Suntzeff, N. B. 2000, in American Institute of Physics Conference Series, Vol. 522, American Institute of Physics Conference Series, ed. S. S. Holt & W. W. Zhang, 65–74

Suntzeff, N. B., Phillips, M. M., Covarrubias, R., et al. 1999, AJ, 117, 1175

Suzuki, N., Rubin, D., Lidman, C., et al. 2012, ApJ, 746, 85

Taubenberger, S., Benetti, S., Childress, M., et al. 2011, MNRAS, 412, 2735

Thomas, R. C., Nugent, P. E., & Meza, J. C. 2011, PASP, 123, 237

Walker, E. S., Hachinger, S., Mazzali, P. A., et al. 2012, MNRAS, 427, 103

Wang, X., Li, W., Filippenko, A. V., et al. 2008, ApJ, 675, 626

Wang, X., Li, W., Filippenko, A. V., et al. 2009, The Astrophysical Journal, 697, 380

Wang, X., Wang, L., Filippenko, A. V., et al. 2012, The Astrophysical Journal, 749, 126

Woosley, S. E., & Kasen, D. 2011, ApJ, 734, 38

Yamanaka, M., Maeda, K., Kawabata, M., et al. 2014, ApJL, 782, L35

Yaron, O., & Gal-Yam, A. 2012, PASP, 124, 668

Zhang, J.-J., Wang, X.-F., Bai, J.-M., et al. 2014, AJ, 148, 1

Zhang, J.-J., Wang, X.-F., Sasdelli, M., et al. 2016, ApJ, 817, 114

APPENDIX A

DECONTAMINATED UVOT SPECTRAL ATLAS

Spectra of SNe Ia processed using our decomtamination method (Section 2.2.2.1) and templates observed as part of our *Swift* Guest Investigator project are presented here. Details of the spectral observations and reductions can be found in Table A.1.

A.1 SN 2005df

Four spectra of SN 2005df extracted using our empirical decontamination technique are presented in Figure A.1. An earlier reduction of these observations were presented by Bufano et al. (2009). We were unable to remove the severe contamination from a saturated zeroth order field source below 2500 Å and obtained no usable spectra below this limit. The spectra of Bufano et al. (2009) predate the UVOTPY software, and so the spectra presented here are favorable because they have been reduced using the most recent calibrations and updated software. We calculated phases relative to B-band maximum light using the peak value of Milne et al. (2010) occurring at $JD = 2453598.825$.

A.2 SN 2009dc

A UVOT spectrum of SN 2009dc was presented in Brown et al. (2014c). We re-extracted this spectrum using our empirical decontamination technique and present it in Figure A.2. The spectral features blueward of 2700 Å are still present following decontamination. The phase of this observation was calculated using the UVOT photometry B-band time of maximum light of $JD = 2454947.3$ (Brown et al., 2014c).

Table A.1: Observation details for SNe Ia utilizing emperical decontamination.

Ellipsis symbols (. . .) denote spectra for which we did not apply the empirical decontamination technique in the extraction process. These spectra did not show any signs of contamination and are included for completeness. ⋆ Relative to B-band maximum light. † This epoch's observations were comprised of three roll angles, additional template obsids are 00092172006 and 00092172008.

SN	Obsid	Template Obsid	Date	JD (2450000+)	Phase⋆ (days)	Exposure Time (s)
2005df	00030252004	00092169002	2005 Aug 11	3599.2	-5.2	1640
2005df	00030252010	00092169002	2005 Aug 14	3596.6	-2.2	986
2005df	00030252014	00092169002	2005 Aug 17	3600.4	1.6	2018
2005df	00030252019	. . .	2005 Aug 21	3604.1	5.2	422
2009dc	00031405005	00092171002	2009 May 01	4952.6	5.2	7682
2009ig	00031473007	00092172004†	2009 Aug 25	5069.1	-11.2	4548
2009ig	00031473010	00092172014	2009 Aug 27	5071.1	-9.3	14019
2009ig	00031473014	00092172014	2009 Sep 01	5076.1	-4.2	5853
2009ig	00031473017	00092172014	2009 Sep 03	5078.2	-2.2	13524
2009ig	00031473021	00092172014	2009 Sep 07	5082.0	1.6	17337
2009ig	00031473026	00092172012	2009 Sep 14	5089.0	8.6	18010
2010ev	00031751001	00092173002	2010 Jul 05	5383.3	-2.2	17670
2011by	00031977006	00092177002	2011 May 01	5683.1	-7.9	9451
2011by	00031977014	00092177002	2011 May 05	5686.0	-3.9	7780
2011by	00031977019	00092177002	2011 May 07	5686.8	-2.2	9238
2011by	00031977024	. . .	2011 May 10	5689.0	1.1	9553
2011fe	00032094001	00032094018	2011 Sep 07	5811.7	-3.2	3525
2011fe	00032094004	00032094018	2011 Sep 10	5815.0	0.1	4165
2011fe	00032094010	00032094018	2011 Sep 13	5818.0	3.0	3019
2011fe	00032094012	00032094018	2011 Sep 16	5820.6	5.7	3071
2011fe	00032101004	00032101012	2011 Sep 29	5833.8	18.7	2540
2011fe	00032101006	00032101012	2011 Oct 02	5837.4	22.3	4141
2011fe	00032101009	00032101012	2011 Oct 08	5842.9	27.8	3729
2012cg	00032464002	00092179004	2012 May 23	6070.7	-11.4	8875
2012cg	00032464002	00092179004	2012 May 23	6071.1	-10.9	8801
2012cg	00032464008	00092179004	2012 May 26	6074.0	-8.1	8231
2012cg	00032464008	00092179004	2012 May 27	6074.9	-7.2	7346
2012dn	00032516006	00092180002	2012 Jul 22	6131.5	-2.2	3574
2007sr	00031073001	. . .	2007 Dec 20	4455.2	6.4	1780
2007sr	00031073016	00092165002	2007 Dec 25	4459.6	10.8	3730
2007sr	00031073019	00092165002	2007 Dec 26	4460.6	11.8	3392
2007sr	00031073023	. . .	2007 Dec 28	4463.2	14.4	5990
2007sr	00031073026	. . .	2008 Jan 02	4468.0	19.2	5060
2011iv	00031008013	00092178002	2011 Dec 05	5900.7	-5.2	8137
2011iv	00031008016	00092178004	2011 Dec 06	5902.3	-3.7	2902
2011iv	00031008018	00092178004	2011 Dec 07	5902.8	-3.0	5713
2011iv	00031008022	00092178004	2011 Dec 09	5905.3	-0.7	632
2011iv	00031008026	00092178006	2011 Dec 11	5907.0	1.0	12108
2013aa	00032724004	00092181002	2013 Feb 19	6343.2	-0.6	5624
2013aa	00032724009	00092181002	2013 Feb 26	6350.2	6.3	6020

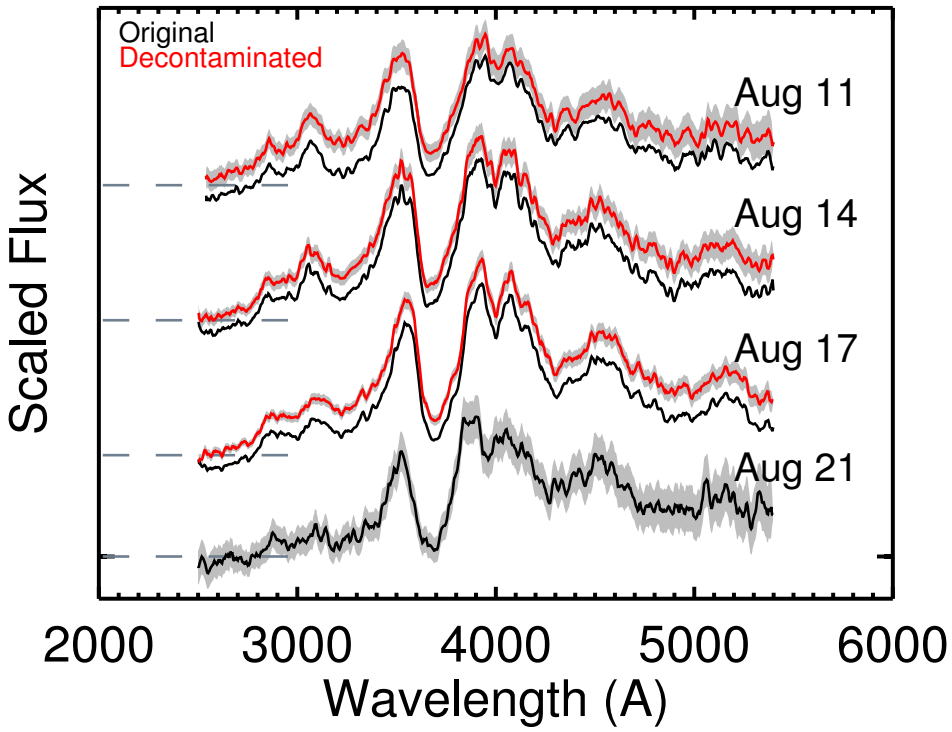

Figure A.1: Spectra of SN 2005df.
Extracted using the regular UVOTPY extraction and our empirical decontamination technique. The offset between the spectra is due to the first order dispersed host galaxy light appearing in the background estimation region of the regular extraction and not appearing within the dispersed SN light measurement region.

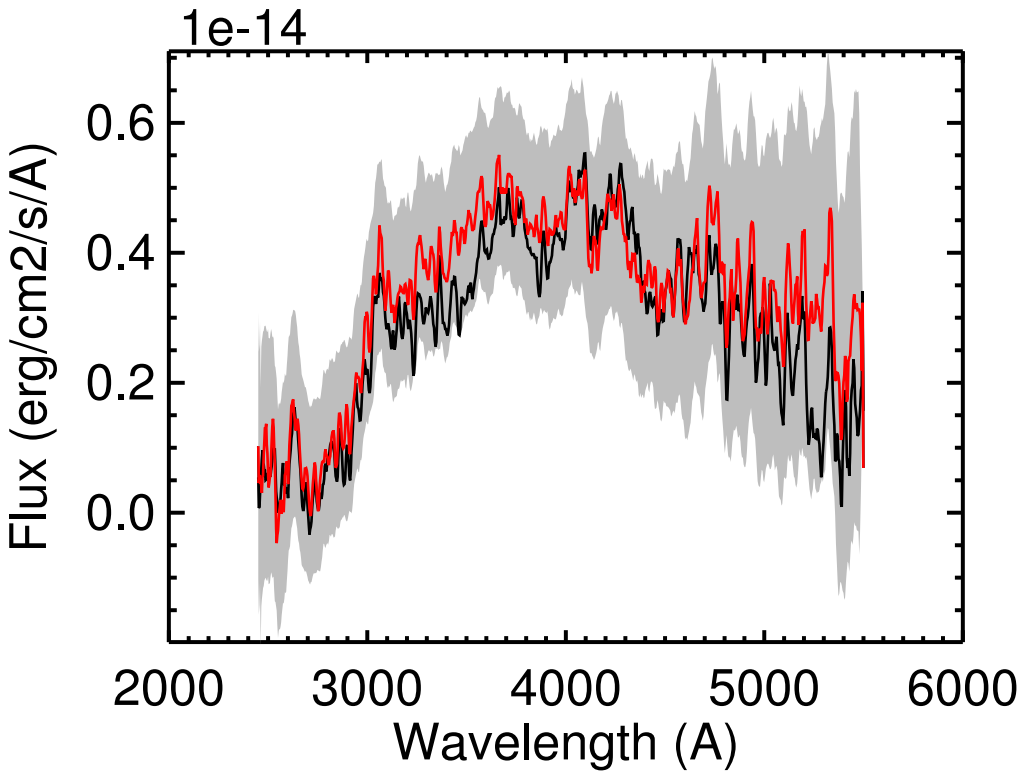

Figure A.2: A spectrum of SN 2009dc.
Observed on 2009 May 01 and extracted using the regular UVOTPY extraction and our empirical decontamination technique. This spectrum was originally presented by Brown et al. (2014c).

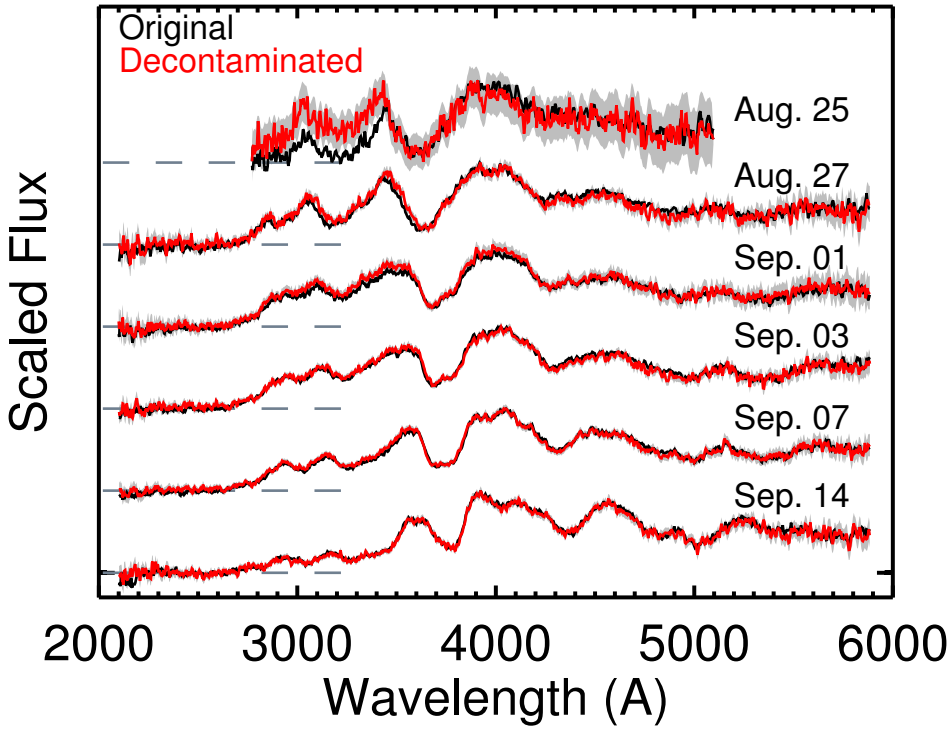

Figure A.3: Spectra of SN 2009ig.
Extracted using the regular UVOTPY extraction and our empirical decontamination technique.

A.3 SN 2009ig

Six spectra of SN 2009ig extracted using our empirical decontamination technique are presented in Figure A.3. We calculated phases relative to B-band maximum light using the peak time of Foley et al. (2012a) occurring at $JD = 2455080.5$.

A.4 SN 2010ev

A spectrum of SN 2010ev extracted using our empirical decontamination technique are presented in Figure A.4. We attempted to decontaminate an additional observation from 2010 July 12 but were unable to extract a viable spectrum due to contamination from an extremely bright nearby bright zeroth order source for which a reliable coincidence loss could not be calculated. The phase of this observation was calculated using the UVOT photometry B-band time of maximum light of $JD = 2455385.4$ from the Swift Optical/Ultraviolet Supernova Archive (SOUSA) (Brown et al., 2014a).

A.5 SN 2011by

Four spectra of SN 2011by extracted using our empirical decontamination technique are presented in Figure A.5. The phases of these observations were calculated using the UVOT photometry B-band time of maximum light of $JD = 2455690.9$ from SOUSA (Brown et al., 2014a).

A.6 SN 2011fe

We extracted seven spectra of SN 2011fe using our empirical decontamination technique. These are presented in Figure A.6. The spectrum from 2011 September 10 is the same as in Section 2.2.2.2. We calculated phases relative to B-band maximum light using the peak value of Pereira et al. (2013) occurring at $JD = 2455815.0$.

A.7 SN 2012cg

Four spectra of SN 2012cg extracted using our empirical decontamination technique are presented in Figure A.7. Both obsids contained many exposures, so we broke each into two groups for analysis to give better time resolution. The phases of these observations were calculated using the UVOT photometry B-band time of

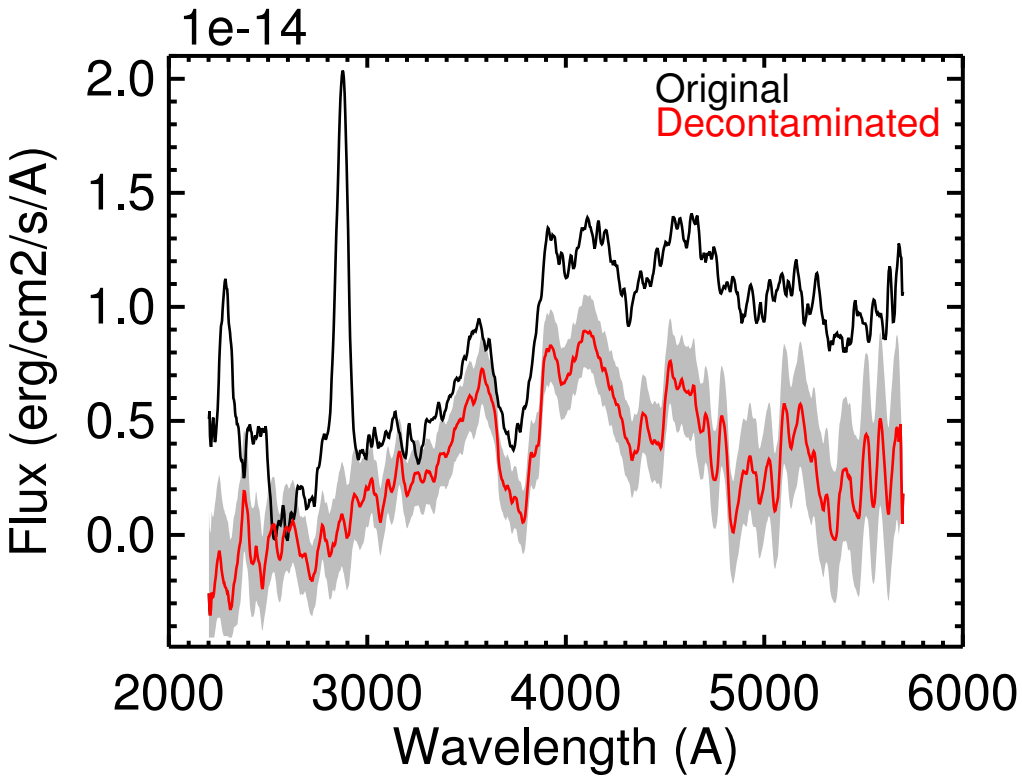

Figure A.4: Spectra of SN 2010ev.
Observed on 2010 July 05 and extracted using the regular UVOTPY extraction and our empirical decontamination technique. The offset between the spectra is due to the first order dispersed host galaxy light being superimposed on the dispersed SN spectrum and not appearing within the background estimation region.

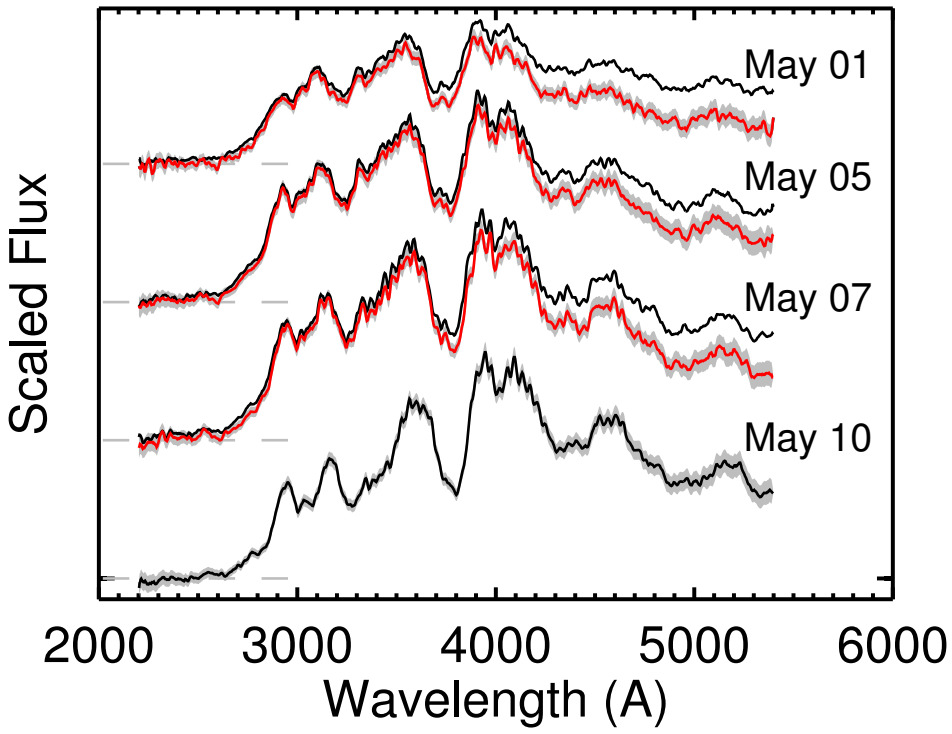

Figure A.5: Spectra of SN 2011by.
Extracted using the regular UVOTPY extraction and our empirical decontamination technique.

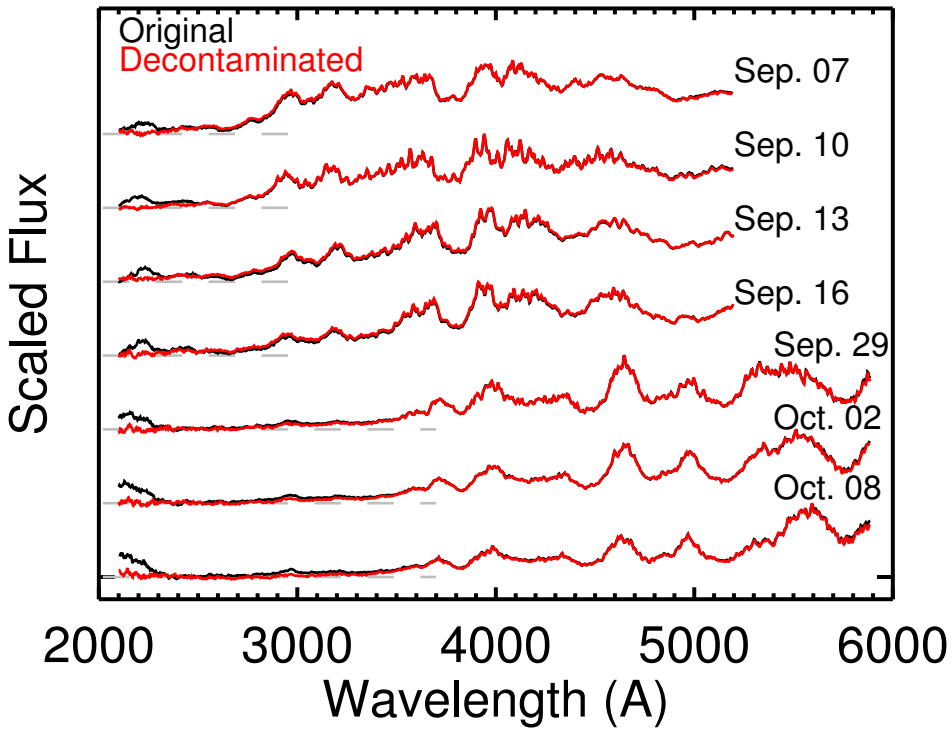

Figure A.6: Spectra of SN 2011fe.
Extracted using the regular UVOTPY extraction and our empirical decontamination technique. Error contours are smaller than the thickness of the plotting lines.

maximum light of $JD = 2456082.1$ from SOUSA (Brown et al., 2014a).

A.8 SN 2012dn

A UVOT spectrum of SN 2012dn was presented in Brown et al. (2014c). We re-extracted this spectrum using our empirical decontamination technique and present it in Figure A.8. The spectral features blueward of 2700 Å documented by Brown et al. (2014c) are still present following decontamination. The phase of this observation was calculated using the UVOT photometry B-band time of maximum light of $JD = 2456133.3$ (Brown et al., 2014c).

A.9 SN 2007sr

Five spectra of SN 2007sr are presented in Figure A.9.

A.10 SN 2011iv

Five spectra of SN 2011iv are presented in Figure A.10

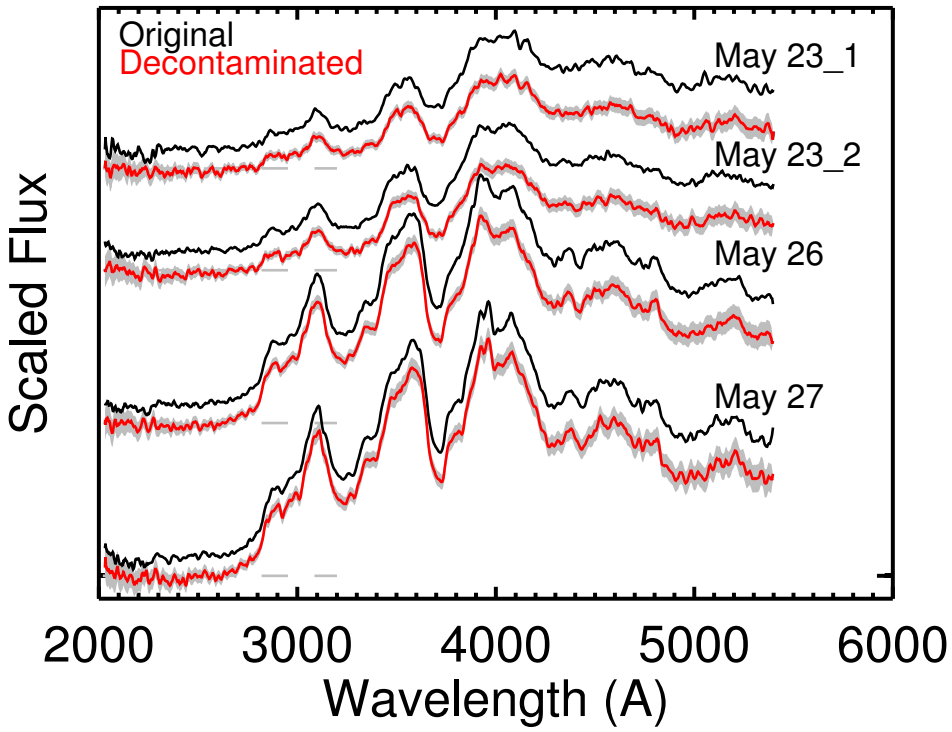

Figure A.7: Spectra of SN 2012cg.
Extracted using the regular UVOTPY extraction and our empirical decontamination technique. The offset between the spectra is due to the first order dispersed host galaxy light being superimposed on the dispersed SN spectrum and not appearing within the background estimation region.

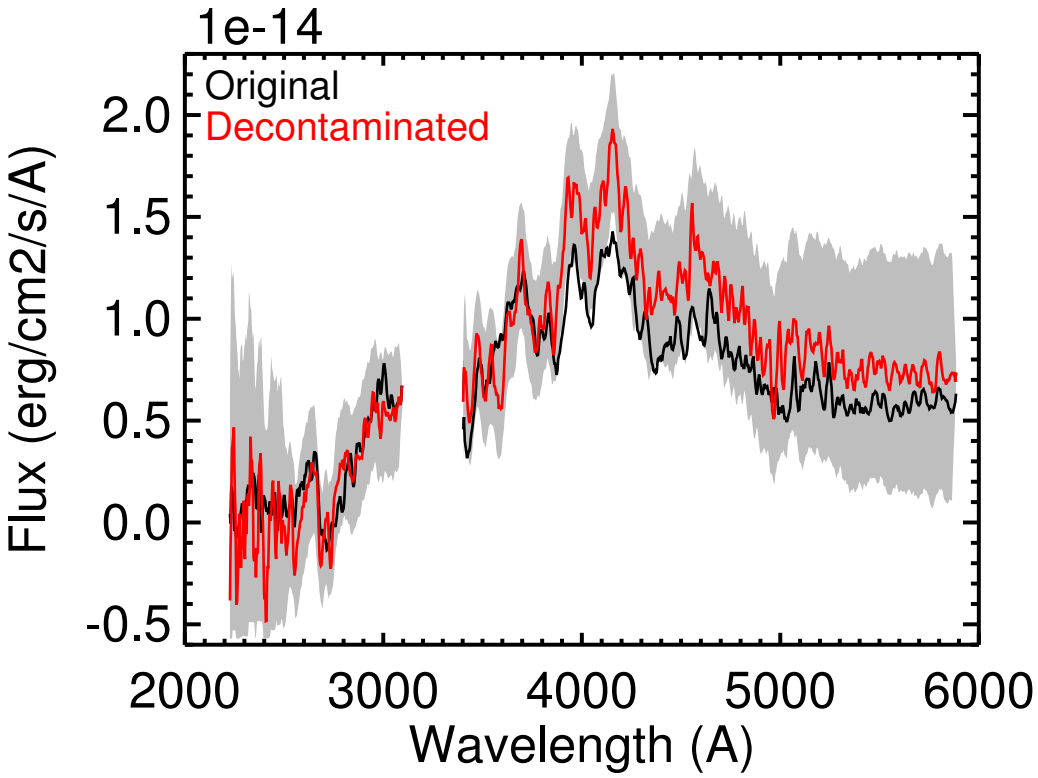

Figure A.8: A spectrum of SN 2012dn.
Observed on 2012 July 22 and extracted using the regular UVOTPY extraction and our empirical decontamination technique. This spectrum was originally presented by Brown et al. (2014c). A portion of the spectrum was trimmed due to severe contamination from a very bright field source.

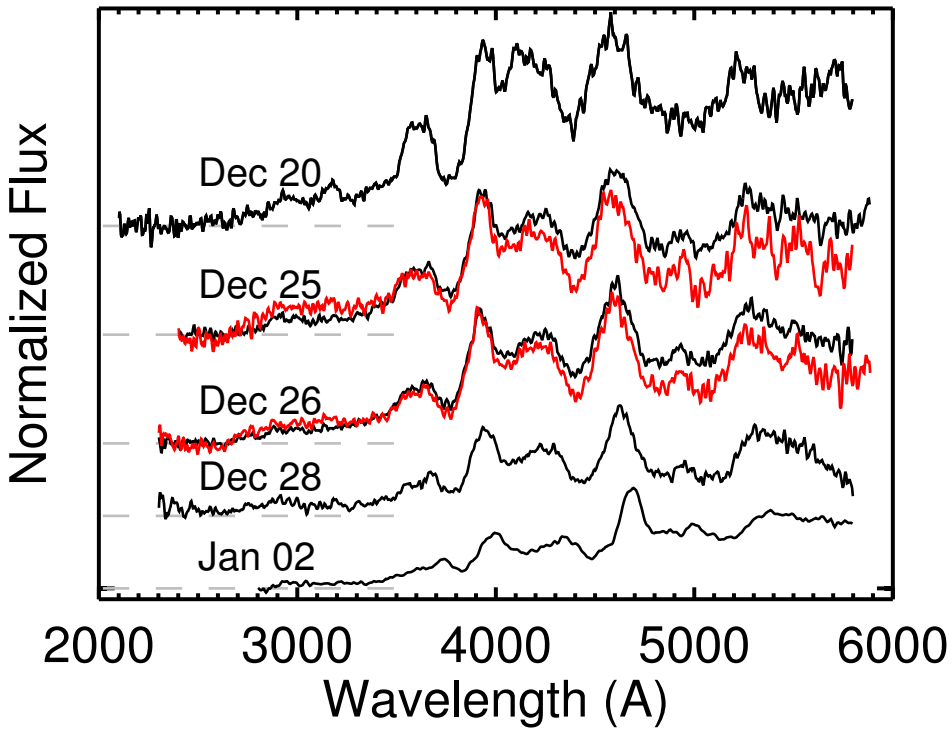

Figure A.9: Spectra of 2007sr.
Extracted using the regular UVOTPY extraction method and and our empirical decontamination technique.

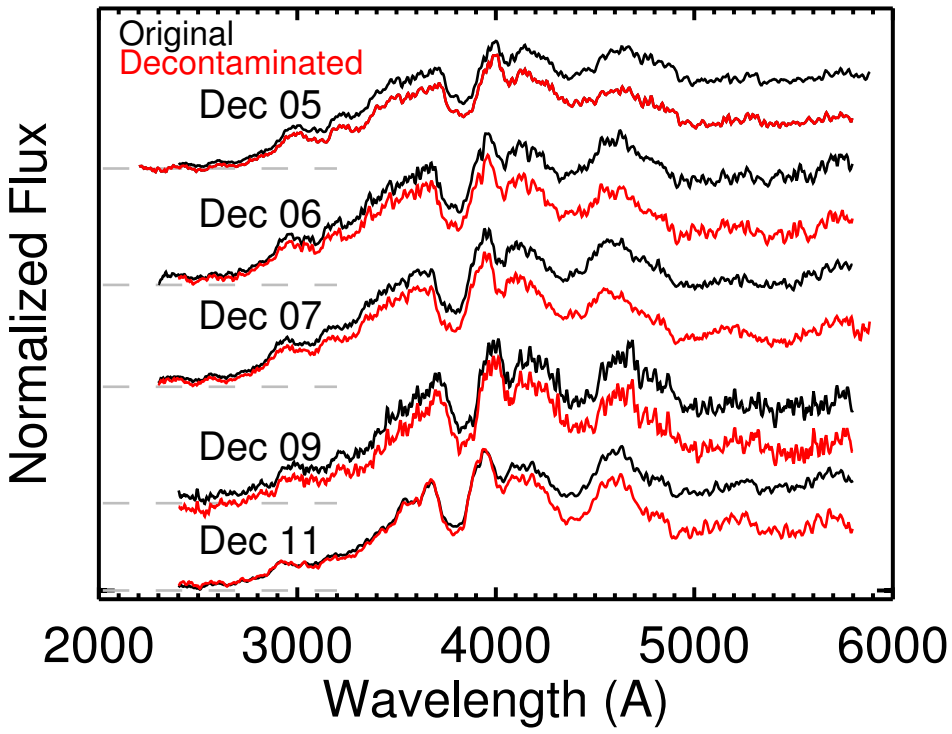

Figure A.10: Spectra of 2011iv.
Extracted using the regular UVOTPY extraction method and and our empirical decontamination technique.

APPENDIX B

NORMAL UVOTPY UVOT SPECTRAL ATLAS

Swift UVOT spectra of SNe observations extracted using the normal UVOTPY extraction are presented here. Details of the observations can be found in Table B.1.

B.1 SN 2005am

The spectra of SN 2005am are presented in Figure B.1.

B.2 SN 2005cf

The spectra of SN 2005cf are presented in Figure B.2.

B.3 SN 2005ke

Two spectra of SN 2005ke are presented in Figure B.3. This SN is of the 1991bg-like subclassification. These are the only published spectra of this subclass of SN Ia. Phases are calculated relative to B-band maximum light using the peak value of Contreras et al. (2010).

B.4 SN 2006ej

The spectra of SN 2006ej are presented in Figure B.4.

B.5 SN 2008Q

The spectra of SN 2008Q are presented in Figure B.5.

B.6 SN 2009Y

The spectra of SN 2009Y are presented in Figure B.6.

B.7 SN 2009an

The spectra of SN 2009an are presented in Figure B.7.

Table B.1: Observation details for SNe Ia utilizing normal extraction.

SN	Obsid	Date	JD (2450000+)	Phase (days)	Exposure Time (s)
2005am	00030010007	2005 Mar 09	3439.1	1.1	2370
2005am	00030010054	2005 Mar 23	3452.6	14.6	1840
2005cf	00030028008	2005 Jun 04	3526.2	-8.6	1604
2005cf	00030028011	2005 Jun 05	3527.2	-7.6	1653
2005cf	00030028014	2005 Jun 06	3538.2	-6.6	1409
2005cf	00030028020	2005 Jun 08	3530.3	-4.6	1462
2005cf	00030028023	2005 Jun 09	3531.0	-3.8	540
2005cf	00030028026	2005 Jun 10	3532.2	-2.6	600
2005cf	00030028029	2005 Jun 11	3533.1	-1.7	1707
2005cf	00030028044	2005 Jun 16	3537.9	3.0	1532
2005cf	00030028047	2005 Jun 17	3538.8	3.9	1697
2005cf	00030028050	2005 Jun 20	3542.3	7.4	1690
2005cf	00030028057	2005 Jun 26	3547.8	13.0	1692
2005cf	00030028059	2005 Jun 29	3550.6	15.8	1864
2005ke	00030342003	2005 Nov 20	3694.9	-4.2	1633
2005ke	00030342007	2005 Nov 22	3696.9	-2.3	3070
2006ej	00030801004	2006 Aug 27	3974.8	-2.4	2150
2008Q	00031103007	2008 Feb 09	4505.7	-0.8	7000
2008Q	00031103010	2008 Feb 13	4510.2	3.7	4987
2009Y	00037276005	2009 Feb 07	4870.2	-5.5	5710
2009Y	00031343002	2009 Feb 08	4870.9	-4.7	8251
2009Y	00031343004	2009 Feb 10	4873.2	-2.4	12418
2009Y	00031343006	2009 Feb 11	4874.4	-1.3	6269
2009Y	00031343009	2009 Feb 13	4875.6	0.0	15102
2009Y	00037276007	2009 Feb 18	4881.0	5.4	8788
2009Y	00037276009	2009 Feb 19	4881.6	6.0	2748
2009an	00031363002	2009 Mar 03	4894.2	-5.3	18746
2009an	00031363008	2009 Mar 10	4901.1	1.5	8425
2009an	00031363010	2009 Mar 12	4902.8	3.2	10280
2011ao	00031935002	2011 Mar 08	5629.2	-11.0	10652
2011ao	00031935004	2011 Mar 09	5630.0	-10.2	6635
2011ao	00031935006	2011 Mar 15	5636.2	-4.0	7872
2012fr	00032614004	2012 Nov 03	6234.9	-8.6	5927
2012fr	00032614006	2012 Nov 04	6236.2	-7.5	11279
2012fr	00032614010	2012 Nov 07	6239.2	-4.4	12645
2012fr	00032614014	2012 Nov 08	6239.6	-4.0	3510
2012fr	00032614019	2012 Nov 10	6242.0	-1.6	9845
2012fr	00032614021	2012 Nov 11	6243.1	-0.5	4546
2012fr	00032614025	2012 Nov 13	6245.0	1.3	16423
2012ht	00032662004	2012 Dec 26	6287.8	-8.3	13492
2012ht	00032662007	2012 Dec 28	6289.9	-6.2	6856
2012ht	00032662010	2012 Dec 31	5293.2	-2.8	5587
2013aa	00032724004	2013 Feb 19	6343.2	-0.6	5624
2013aa	00032724009	2013 Feb 26	6350.2	6.3	6020
2014J	00033123006	2014 Jan 25	6683.0	-7.2	11239
2014J	00033123025	2014 Feb 01	6689.5	-0.8	7518
2014J	00033123032	2014 Feb 03	6692.0	1.8	8030
2014J	00033123036	2014 Feb 04	6693.4	3.2	4330
2014J	00033123040	2014 Feb 05	6694.4	4.2	4730
2014J	00033123045	2014 Feb 07	6696.1	5.9	4172
2014J	00033123049	2014 Feb 08	6697.2	7.0	4097

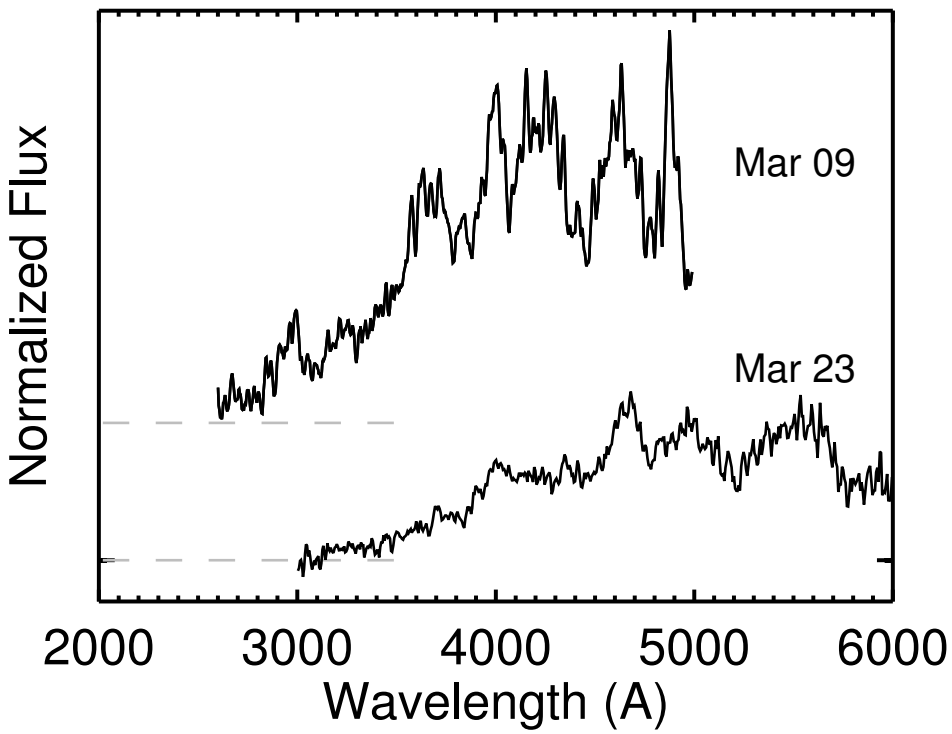

Figure B.1: Spectra of SN 2005am.
Extracted using the regular UVOTPY extraction.

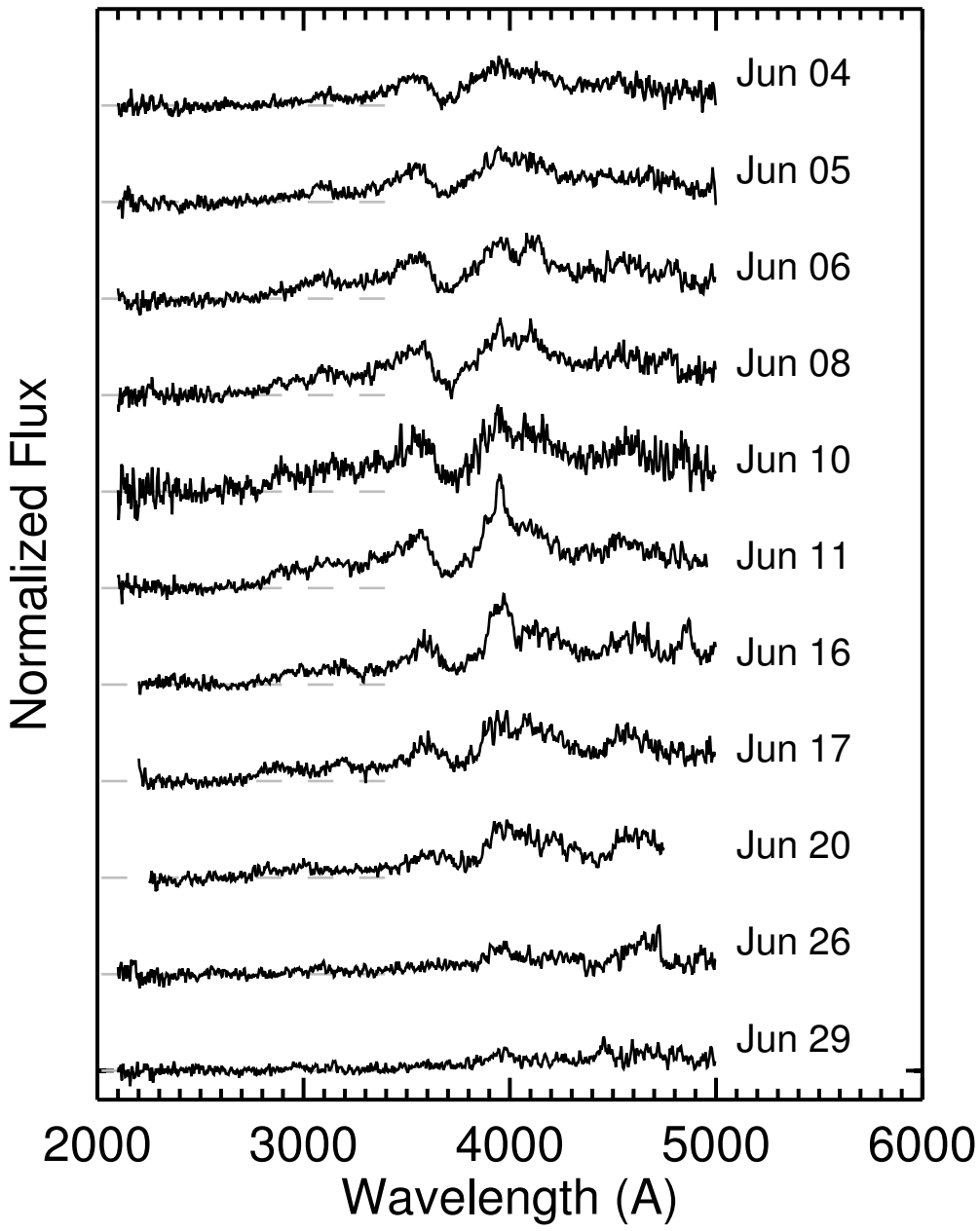

Figure B.2: Spectra of SN 2005cf.
Extracted using the regular UVOTPY extraction.

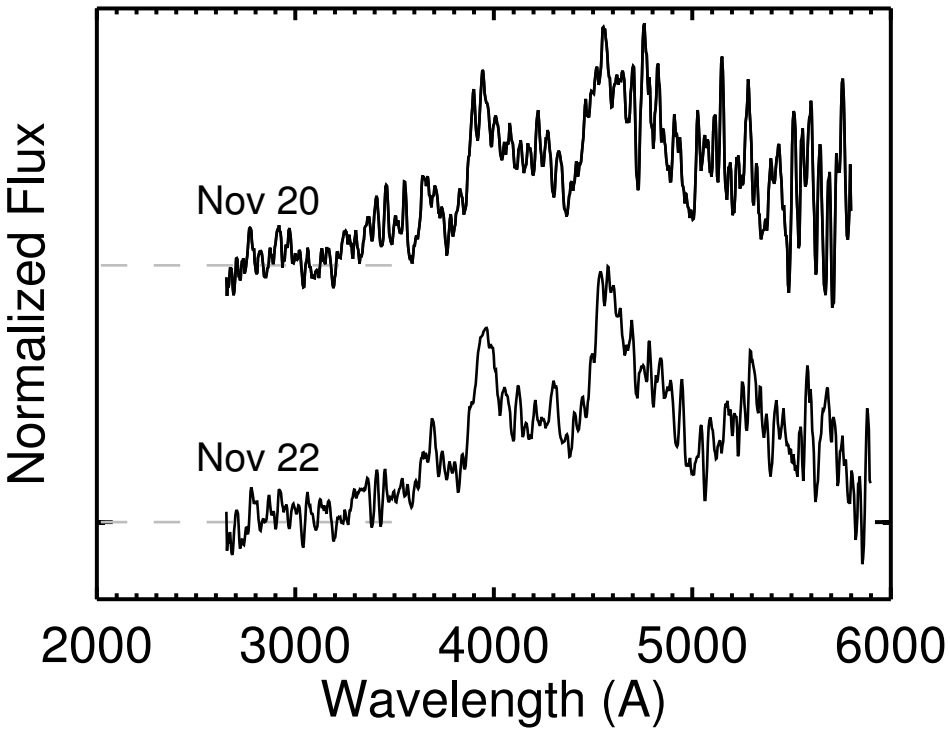

Figure B.3: Spectra of SN 2005ke.
Extracted using the regular UVOTPY extraction. This SN is classified as 1991bg-like in the optical.

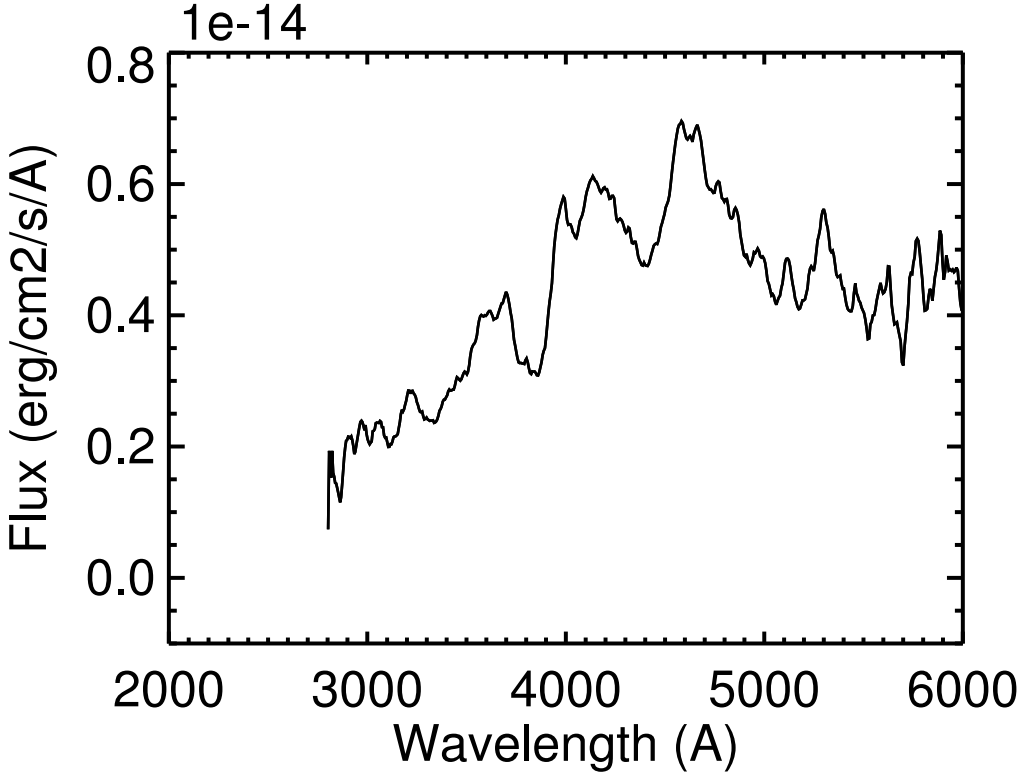

Figure B.4: Spectra of SN 2006ej.
Extracted using the regular UVOTPY extraction.

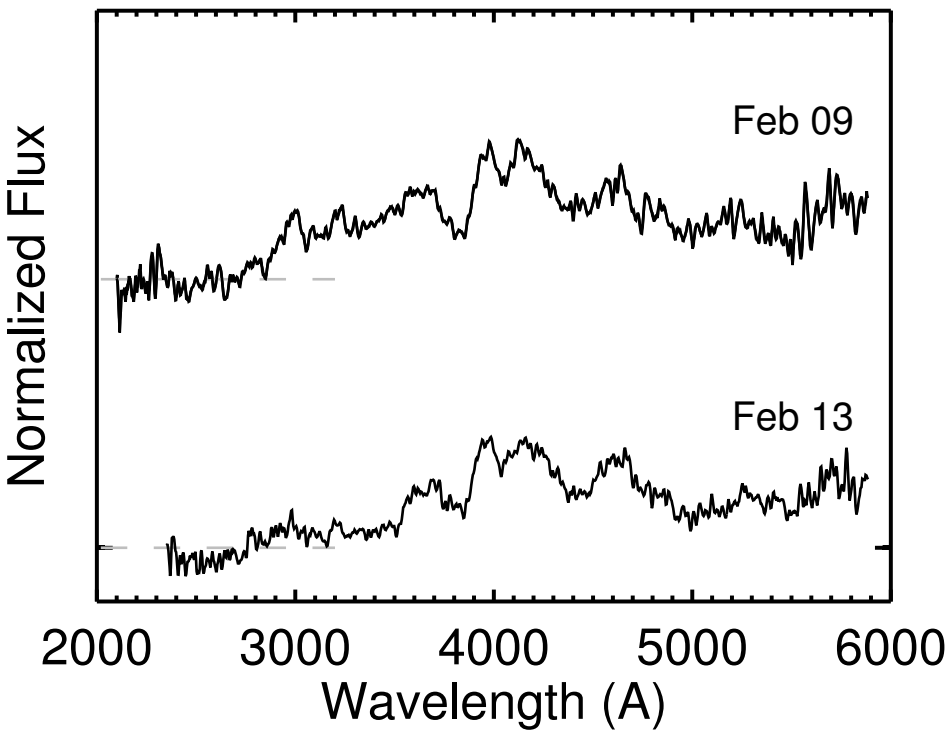

Figure B.5: Spectra of SN 2008Q.
Extracted using the regular UVOTPY extraction.

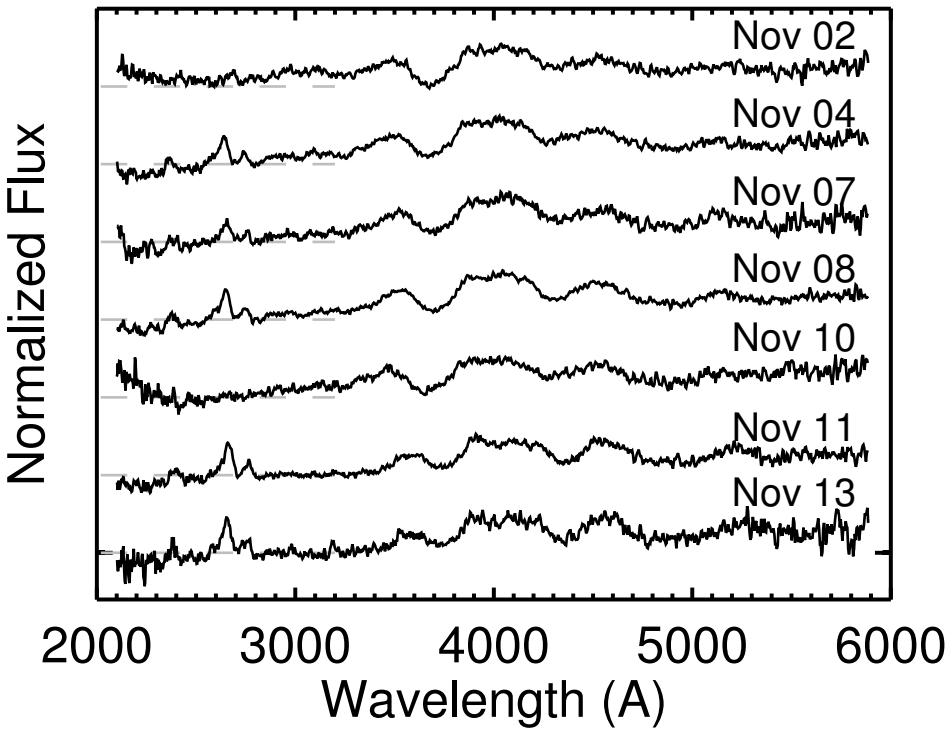

Figure B.6: Spectra of SN 2009Y.
Extracted using the regular UVOTPY extraction.

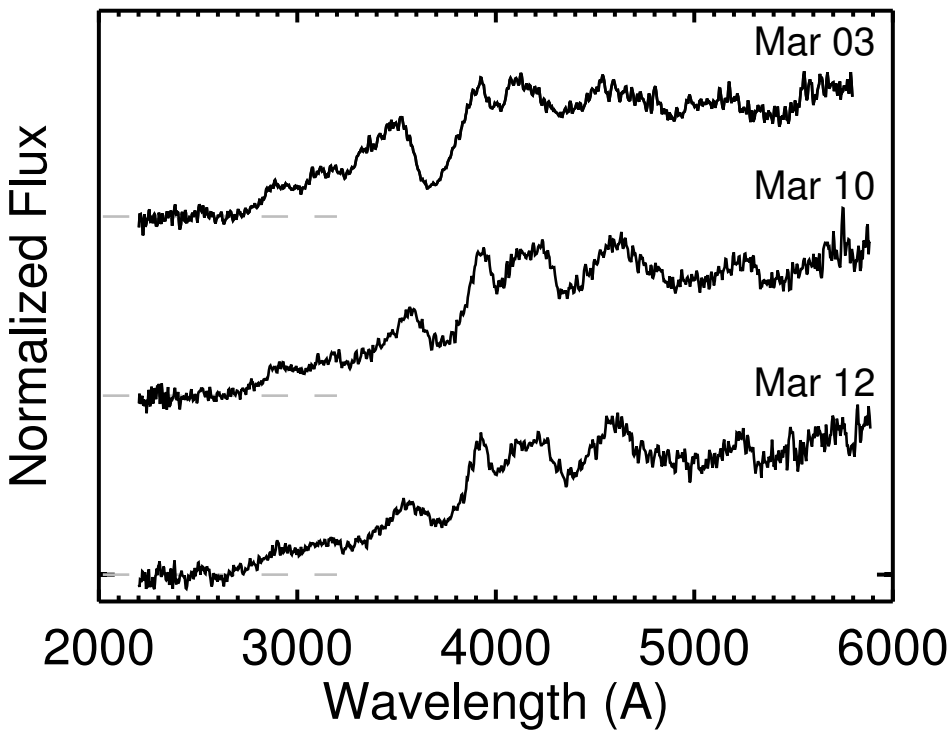

Figure B.7: Spectra of SN 2009an.
Extracted using the regular UVOTPY extraction.

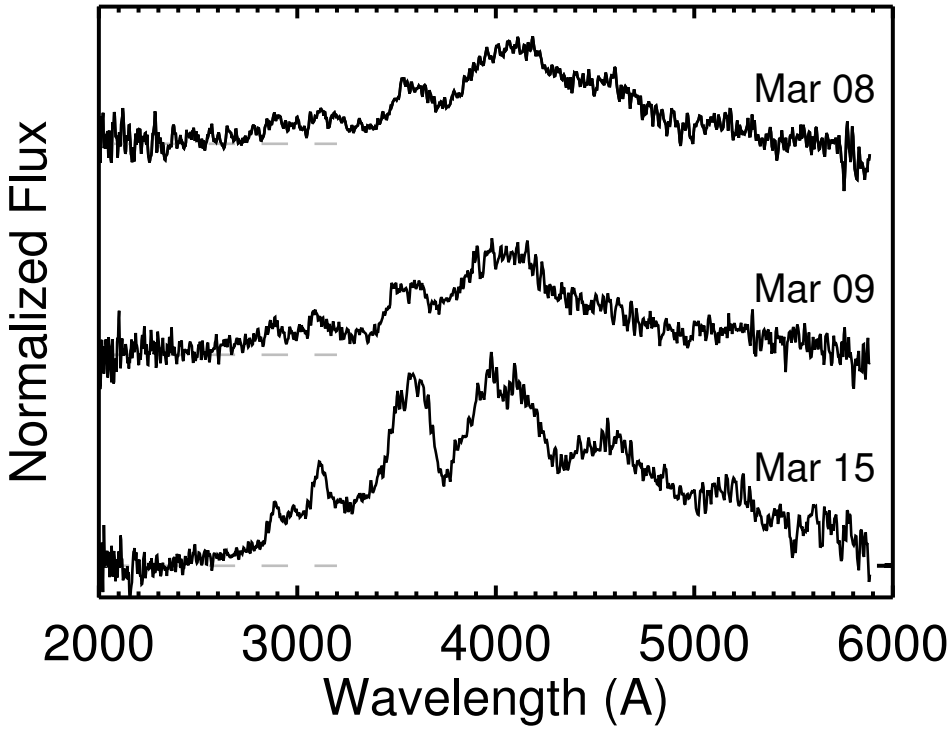

Figure B.8: Spectra of SN 2011ao.
Extracted using the regular UVOTPY extraction.

B.8 SN 2011ao

The spectra of SN 2011ao are presented in Figure B.8.

B.9 SN 2012fr

The spectra of SN 2012fr are presented in Figure B.9.

B.10 SN 2012ht

Two spectra of SN 2012ht are presented in Figure B.10.

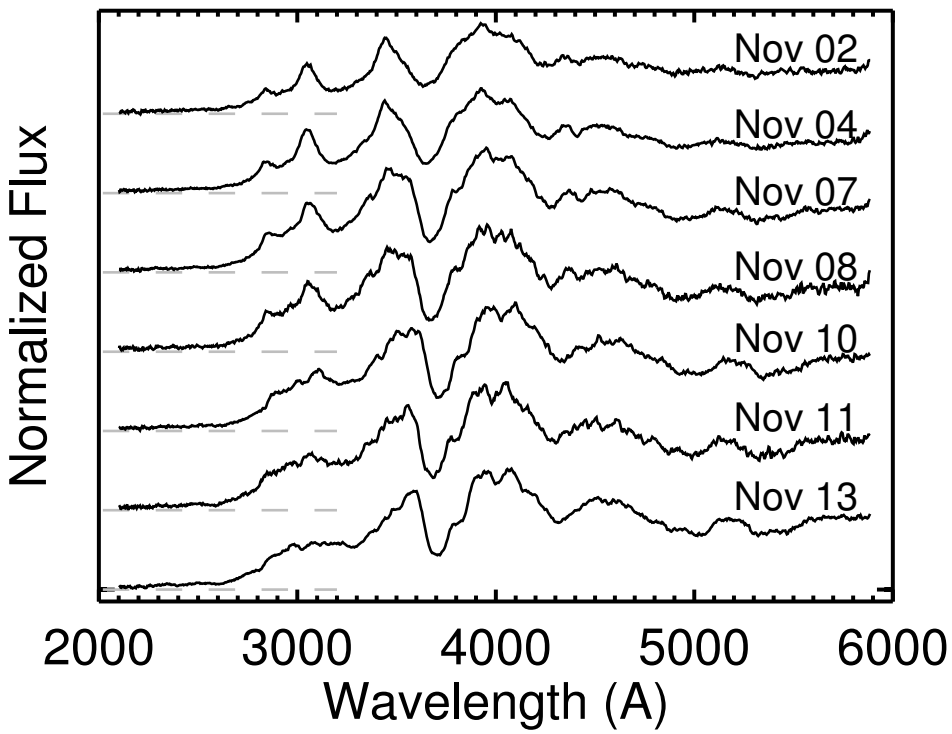

Figure B.9: Spectra of SN 2012fr.
Extracted using the regular UVOTPY extraction.

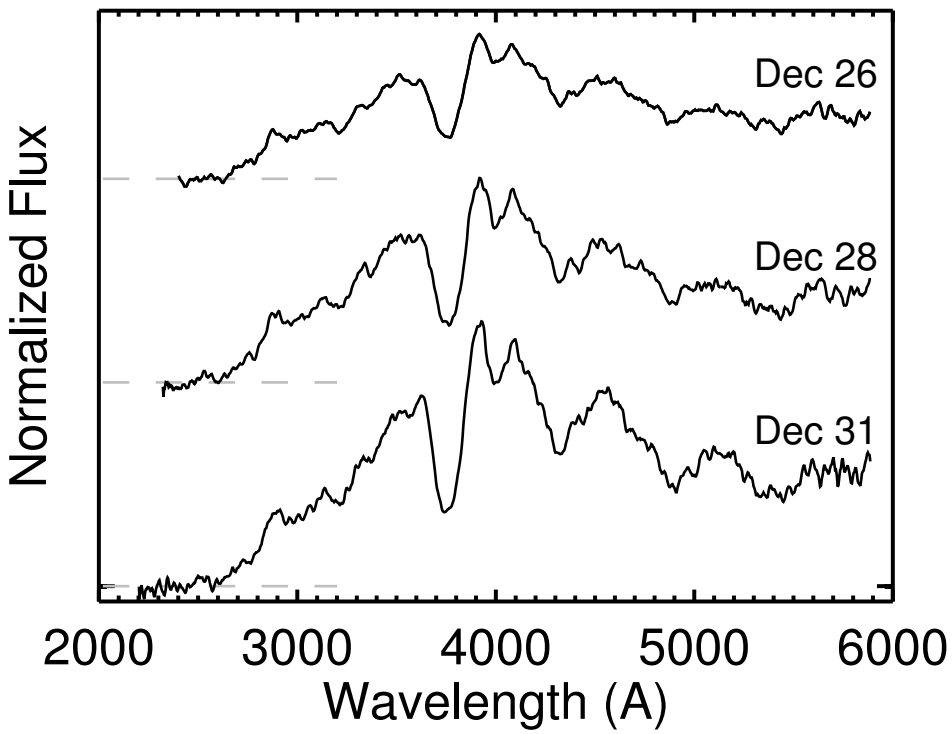

Figure B.10: Spectra of SN 2012ht.
Extracted using the regular UVOTPY extraction.

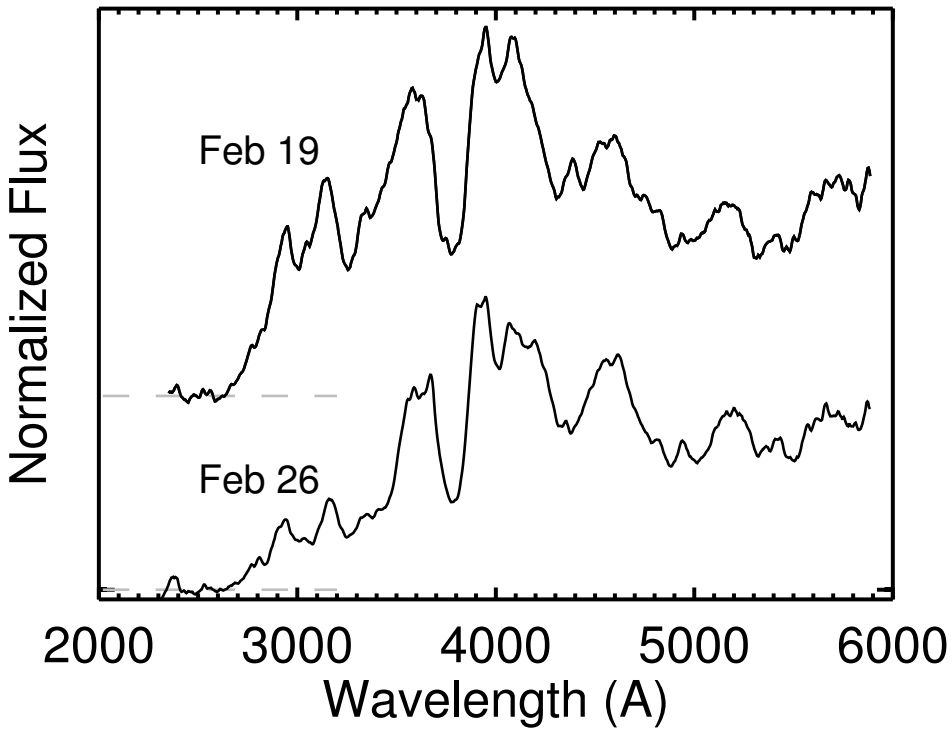

Figure B.11: Spectra of SN 2013aa.
Extracted using the regular UVOTPY extraction.

B.11 SN 2013aa

Two spectra of SN 2013aa are presented in Figure B.11.

B.12 SN 2014J

The spectra of SN 2014J are presented in Figure B.12. This SN is known to exhibit extreme extinction (Brown et al., 2015b). Phases are calculated relative to B-band maximum light using the peak value of Marion et al. (2015).

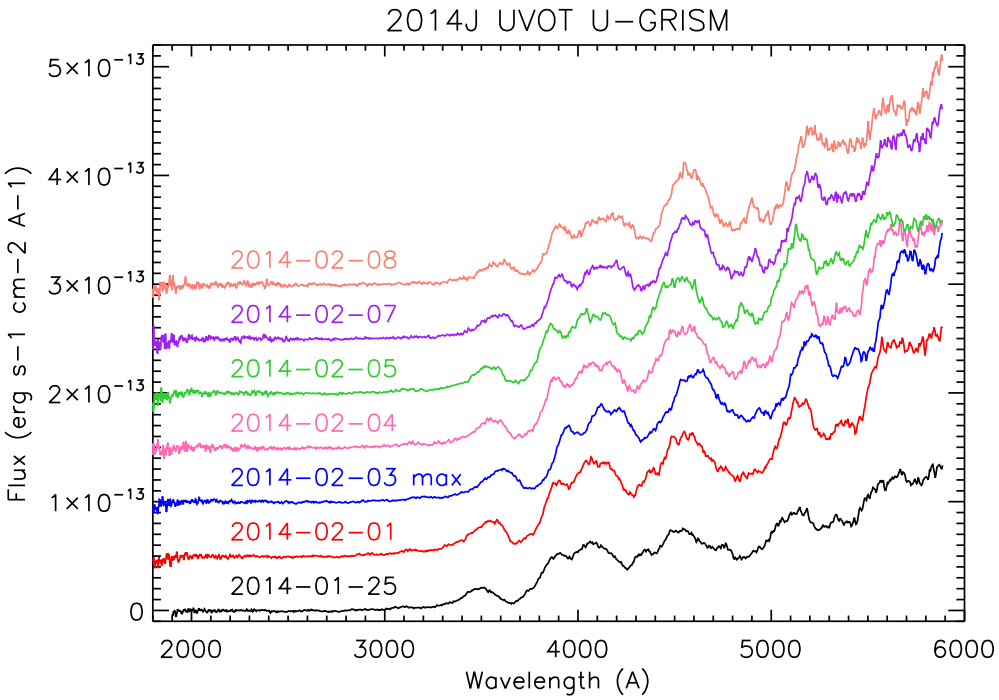

Figure B.12: Spectra of SN 2014J.
Extracted using the regular UVOTPY extraction.